MODELLING THE MOVEMENT OF MARINE PARTICLES IN DISCRETE TIME AND SPACE WITH APPLICATION TO SCOTIAN SHELF CONNECTIVITY

by

Erica C. Rogers

Submitted in partial fulfillment of the requirements
for the degree of Master of Science

at

Dalhousie University
Halifax, Nova Scotia
August 2015

For my parents, who always told me I could.

And for my children: I know you can.

TABLE OF CONTENTS

LIST OF TABLES

LIST OF FIGURES

ABSTRACT

The complexity of ocean circulation makes it difficult to predict both the origin and destination of objects transported by ocean currents. Many practical applications (e.g., planning marine search and rescue operations, predicting the year class success of important fisheries, and responding to threats posed by oil spills and mines) require a Lagrangian approach to the modelling of fluid movement. Similarly, many scientific applications (e.g., understanding the connections between the spawning and nursery areas of marine organisms, estimating the residence time of deep ocean basins and the exchange between them) are sometimes tackled more effectively using a Lagrangian approach. One way of estimating where objects come from, and where they go, is based on integrating a stochastic differential equation for particle position. In this thesis, the effectiveness of two such methods are explored: one based on discretization in time (the conventional approach) and another based on discretization in space. The ability of the methods to deal with both Lagrangian chaos (evident in time varying flows without diffusion) and spatial gradients in diffusivity (leading to false aggregation of particles), is discussed using simple, idealized examples. The discrete-space method is then applied and evaluated for the Scotian Shelf-Gulf of Maine system using flow fields predicted by an ocean circulation model with a horizontal grid spacing of about 2 km. Positively and neutrally buoyant particles are tracked in both two and three dimensions. Connectivity between deep basins, and the shelf break, is quantified for the study area and the ability of the discrete space tracking scheme to predict the observed movement of near surface drifters is assessed.

LIST OF ABBREVIATIONS AND SYMBOLS USED

Abbreviation	Description
ADCP	Acoustic Doppler Current Profiler
DS	Discrete Space
DT	Discrete Time
pdf	Probability Distribution Function
HYCOM	HYbrid Coordinate Ocean Model
JRCC	Joint Rescue Coordination Centre
NCODA	Navy Coupled Ocean Data Assimilation
NEMO	Nucleus for European Modelling of the Ocean
NSC	Nova Scotia Current
ODE45	Ordinary Differential Equation 45
SAR	Search and Rescue
SDE	Stochastic Differential Equation
TA	Target Area

Symbol	Description	Units*
x	vector; particle position; Cartesian system with scalar (x,y,z)	
t	time	s
u	advective component of particle movement	m s^{-1}
ϵ	stochastic (diffusive) component of particle movement	m s^{-1}
g	"personality" component of particle movement	
W_t	Wiener process	
D	Diffusion	m^2 s^{-1}
p	probability distribution	
z	complex vector; center of Aref's blinking vortex	m
b	real coordinates of the center of Aref's vortex	m
a	Aref's vortex radius	m
Γ	strength of Aref's vortex	m s^{-1}
ζ	vector; Aref's particle position	m
$\dot{\zeta}$	Aref's particle motion	m s^{-1}
λ	constant; determining the size of particle trajectory (Aref)	
ρ	radius of arc of particle trajectory (Aref)	
ζ_c	vector; center of the arc of particle trajectory (Aref)	m
T	time; one cycle of the Aref system	s
σ	standard deviation	
N, n	normal distribution; or integer	
a_d, b_d	linear regression coefficients	m s^{-1}
W_{10}	windspeed at 10 m above sea level	m s^{-1}
r	radius of uncertainty in position	m
L	length of the side of a grid box	m
ε	random displacement amount	m
I	identity matrix	

Symbol	Description	Units*
ψ	stream function	$m^2\ s^{-1}$
α	integer; scale factor	
τ	e-folding time	days

*Note that for the theoretical examples described in this work, the units of the following symbols have been generalized as [length] or [time]. However, for simplicity, they have been listed in this table as [meters] and [seconds].

ACKNOWLEDGEMENTS

I would like to thank my co-supervisors, Dr. Keith Thompson and Dr. Haibo Niu for their support and guidance. Their expertise, patience and persistence kept me on track and helped me learn so much more than is reflected in this document. You brought me a long way: from being afraid of Matlab to a somewhat competent programmer; a feat which was far from easy. I would also like to thank Dr. Thompson for putting up with all my colourful rainbow plots with his patient repetition of "but where's the math Erica?"

I greatly appreciate the comments and suggestions from my external, Dr. Brad deYoung and sincerely thank him for agreeing to be my external on short notice. I am truly grateful that you made the time for me despite your busy schedule.

I would also like to thank my remaining committee members: Dr. Harold Ritchie and Dr. Youyu Lu not only for their suggestions throughout my research and the thesis writing process, but also for teaching the OCEA 5220 course: Numerical Modelling of Atmospheres and Oceans. This course was instrumental to my success.

My sincere gratitude goes to my academic sister, Anna Katavouta for generously allowing me to use the results of her Regional Model. As well, thank you to Tsubasa Kodaira, Zhongjie He for the data they provided.

A special thank you to Mathieu Dever for keeping me laughing (and laughing and laughing). Jenna Hare: you are a Latex whiz and an excellent hugger. Thank you for being my academic buddy stand-in. Anne Lombardi and Anne McKee, your home-baked goods are worthy of many prizes and I would love to be the judge of a bake off at any time.

I would be remiss if I didn't acknowledge the Canadian Navy for sponsoring me. In particular, without the forward-thinking, persistence and support from Major Norm Scantland, I would not have been granted permission to be here. Sir, I cannot express how grateful I am.

I honestly can not count the number of times Justine McMillan helped me. You never failed to take time out from your own busy workload to talk me off the ledge and invariably solved any problem I had, from simple coding errors in Matlab or Latex, to oceanographic concepts. You have been the best officemate a girl could ask for and you know a big piece of the puzzle is yours.

Perhaps most importantly, I would like to thank my family (who had to put up with me during the times that Justine wasn't available to talk me off my ledge). To my husband, Lee, thank you for never hesitating to rearrange your own busy schedule when I needed to work late (usually on extremely short notice). Your love and support are my touchstone and I would be lost without you. To my parents - you always told me I could do anything I put my mind to. Thank you for your unwavering belief in me. I hope to pass the self-confidence you instilled in me to my kids. Finally, to my rambunctious, curious, beautiful children who told me that being a "Master Scientist" was really cool: you can do anything you put your mind to. I love you to the moon and back (yes Owen, a million, million, kagillion times); and no Kate, I love *you* more.

CHAPTER 1

INTRODUCTION

1.1 Background

In fluid mechanics, there are two frames of reference for describing the movement of a fluid: Eulerian and Lagrangian (*Kundu and Cohen*, 2008). The Eulerian frame describes the time-varying field at a given grid location such as a moored current meter would report (*Gill*, 1982). The Lagrangian frame describes the fluid flow from a drifting object or fluid parcels' point of view (*Lumley*, 1969). While the Eulerian method is mathematically simpler, many practical applications, such as planning marine search and rescue operations and responding to threats posed by oil spills and mines, require the Lagrangian approach (*Batchelor*, 1967). Similarly, many theoretical applications such as understanding the connections between the spawning and nursery areas of marine organisms, estimating the residence time of deep ocean basins and the exchange between them, are sometimes tackled more effectively using the Lagrangian approach.

Accurate predictions of the movement of objects and fluid parcels depend on two major contributors to fluid motion: advection and diffusion (*Lynch et al.*, 2015). Advective flow fields that are time independent result in trajectories that are straightforward to calculate; flow patterns that are time dependent can rapidly become more complicated and possibly lead to chaotic advection (*Aref*, 1983). Aref demonstrates this fact through his famous

example of a blinking vortex in which a particle's trajectory is mapped in a flow field where the origin of a vortex is periodically shifted (*Aref*, 1983). The second component that must be accurately described to obtain realistic predictions is diffusion. The concept of Fickian diffusion can be used to address issues related to environmental dispersion (*Fisher et al.*, 1979). However, difficulties can arise when trying to achieve realistic predictions when diffusivity is spatially non-uniform. This has been clearly demonstrated to result in the false aggregation of particles in regions of low diffusivity when simple numerical schemes are used (*Visser*, 1997).

Two main classes of methods are used to model the uncertainty in particle position (*Lynch et al.*, 2015). The first solves a Fokker-Planck equation for the evolution of the probability distribution function of particle position (*Gardiner*, 2009). The second involves integration of a stochastic differential equation (SDE) for the velocity of a single particle (*Gardiner*, 2009). Two types of particle tracking methods already exist. The most common method is based on discretization in time and involves calculating the distance a particle will travel under the influence of a flow field over a given time interval (*Lynch et al.*, 2015). A less common method is based on discretization in space and involves the calculation of an analytic expression for the trajectory within a given grid box (*Blanke and Raynaud*, 1997). The simplest analytic expression assumes the velocity varies linearly across each grid box. Recent examples of the discrete time (DT) and discrete space (DS) methods will be explored in this thesis. The DT example is the Norwegian Search and Rescue model LEEWAY. The DS example is Ariane, a software package developed by Blanke and Raynaud (1997).

While both Ariane and LEEWAY predict where objects will go in the ocean, they can also be used to answer questions about where particles come from. The "forward" method is particularly useful for quantifying regional connectivity, i.e., the probability that a particle will end up in a given area after a specified period of time (*Lynch et al.*, 2015). The

backward method provides estimates of the source region of a particle. (It is interesting to note that the Fokker-Planck equation has a "backward" version which covers this scenario (*Gardiner*, 2009).) The backward tracking method is not straightforward to implement unless the flow field is non-divergent and diffusion is constant (*Gillespie*, 1996). Ariane makes these assumptions. By way of contrast, *Breivik et al.* (2012) used successive forward iterations of LEEWAY to narrow down probable areas of origin. This method is discussed further in Chapter 3. Table 1.1 summarizes the capabilities and differences of both methods.

	Ariane	LEEWAY
Discrete Time		✓
Discrete Space	✓	
Backwards Integration	✓	✓
Random Component	$*$	✓

Table 1.1: Comparison of particle tracking methods. ✓indicates the model has the listed capability; $*$ indicates the capability is absent from the present form of the model. An important difference is that Ariane does not allow for a random component of the flow. The addition of this capability is discussed in Chapter 3.

1.2 Objectives and Structure of the Thesis

The objectives of the research were as follows:

- Evaluate and compare DT and DS particle tracking methods using idealized examples.
- Combine the strengths of both methods, by extending the DS method, Ariane, to include a random component.
- Use Ariane to quantify retention within the deep basins of the Scotian Shelf, and the connectivity between them.

- Assess Ariane's ability to predict the observed movement of near surface drifters in the Scotian Shelf and Gulf of Maine region with focus on search and rescue applications.

The general theory of modelling uncertainty in particle position is discussed in Chapter 2 including: methods based on the Fokker-Planck equation and methods based on stochastic differential equations. This chapter will also address the complexity of predicting flows using two highly idealized examples. The first is designed to illustrate Lagrangian chaos (evident in some time varying flows without diffusion) and the second demonstrates the effect of spatial gradients in diffusivity (leading to false aggregation of particles).

The methods used by DT particle tracker "LEEWAY " and DS particle tracker,"Ariane" are covered in Chapter 3. Also included in this chapter is a method of adding dispersion to Ariane. This was completed in an attempt to combine the strengths from the DS and DT approaches.

An evaluation and comparison of the efficiency and effectiveness of DT and DS methods are discussed in Chapter 4, using idealized examples including (i) a simple vortex, (ii) Aref's blinking vortex, and (iii) Visser's spatially varying diffusivity.

The Scotian Shelf and Gulf of Maine's regional oceanography as well as a description of the flow fields kindly provided by Anna Katavouta (PhD student at Dalhousie University) will be included in Chapter 5.

Deep basin retention is quantified in Chapter 6. In addition, the connectivity between deep basins is explored using DS tracker, "Ariane."

Ariane's ability to predict the observed movement of near surface drifters is addressed in Chapter 7.

The final chapter is a summary and discussion.

CHAPTER 2

OVERVIEW OF MODELLING UNCERTAINTY OF PARTICLE POSITION

As noted in the Introduction, there are two main classes of methods for predicting where objects come from, and go to. According to *Lynch et al.* (2015), the first of these two methods, particle simulation, was "among the earliest uses of the modern computer". The contemporary version is based on the integration of a Langevin equation of the form

$$\frac{dx}{dt} + g(x) = u(x,t) + \epsilon \tag{2.1}$$

where x denotes (vector) position of the particle, g is the particle's "personality" attributes, u is the prescribed environmental condition and ϵ is the stochastic forcing (*Lynch et al.*, 2015). The simplest example of particle tracking involves describing the path of a physically passive, biochemically inert particle through the output of an ocean model (*Lynch et al.*, 2015). The term "personality" refers to any characteristic a particle might have that would cause it to deviate from this simplistic definition, e.g., swimming or buoyancy. The path can be described through integration of the following SDE:

$$\frac{dx}{dt} = u(x,t) + \epsilon(x,t) \tag{2.2}$$

where u is the local fluid velocity (*Lynch et al.*, 2015). The second component, ϵ, describes the stochastic movement that leads to diffusion. An alternate form of this equation involves the integration of the Ito stochastic differential equation:

$$dx = u(x,t)dt + \sqrt{2D(x,t)}dW_t \tag{2.3}$$

where W_t is the Wiener process or Brownian motion often simulated using a random walk (*Jordan et al.*, 1998). Note *Gardiner* (2009) states that integration of (2.3) is "mathematically and technically the most satisfactory, but not always the most natural choice physically." *Gardiner* (2009) goes on to state that an alternative equation, the Stratonovich SDE, is the "natural choice." In this case it is given by

$$dx = u(x,t)\ dt - \frac{1}{2}\frac{\partial}{\partial x}D(x,t)\ dt + \sqrt{2D(x,t)}dW_t \tag{2.4}$$

The key difference in the derivation of these two equations is (2.3) assumes the random component is white noise (statistically uncorrelated) while (2.4) assumes more realistic noise with finite correlation time (*Gardiner*, 2009). The main difference in equation (2.4) compared to (2.3) is the inclusion of the spatial gradient of diffusivity term. This term is intimately related to the false aggregation of particles discussed in Section 2.2.

The second class of methods involves solving an evolving probability distribution function (pdf). Einstein first derived his version of the pdf, later called the Fokker-Planck equation, to describe Brownian motion (*Lemons and Gythiel*, 1997). Interestingly, Langevin first derived his version of (2.1) in response to Einstein's pdf. The one dimensional version of the Fokker-Planck corresponding to the Ito SDE can be written:

$$\frac{\partial p}{\partial t} + \frac{\partial}{\partial x}(up) = \frac{\partial^2}{\partial x^2}(Dp) \tag{2.5}$$

where $p = p(x,t)$ is the probability density of finding the particle at position x at time t, $u(x,t)$ is the fluid velocity and $D = D(x,t)$ is the diffusion coefficient (*Jordan et al.*, 1998). This is similar to an advection-diffusion model of the evolution of concentration of a fluid property based on the concept of Fickian diffusion (*Fisher et al.*, 1979). Two different situations will be explored in this Chapter. The first considers only advective motion in which case the shape of the pdf does not change in time, but rather moves along a trajectory as if it were a particle. The second considers only the diffusive component and therefore describes the time evolution of the shape of the pdf.

While (2.2) and (2.5) seem different, the solution to a given Fokker-Planck equation represents the probability density for the position of a particle whose motion is described by a corresponding stochastic differential equation (*Jordan et al.*, 1998). In other words, the Fokker-Planck effectively describes the solution to N SDEs as $N \to \infty$.

The integration of (2.2) or (2.5) is not as straightforward as might seem. To illustrate, the following two sections describe two different, highly idealized examples. The first shows the complexity that can arise using only the advective component and the second shows the difficulties that can arise when incorporating spatially variable diffusion.

2.1 Lagrangian Chaos: Aref's Blinking Vortex

Trajectories within a steady, time independent flow field are more predictable than those within time varying fields. Time dependence complicates trajectory prediction immensely even in the absence of a diffusive component. Considering only the advective component, (2.2) can be written:

$$\frac{dx}{dt} = u(x,t) \tag{2.6}$$

Consider the flow pattern described by *Aref* (1983) in which two vortices "blink" on and off. If T is the total duration of 1 full cycle (both vortices completing a full blink) then

vortex 1 blinks off at $T/2$ increments (*Aref*, 1983). Figure 2.1 shows the set up, where the location of the centers of the active vortices, $z(t)$, are shown as crosses and are defined by:

$$z(t) = \begin{cases} +b & nT \leqslant t < (n+\frac{1}{2})T \\ -b & (n+\frac{1}{2})T \leqslant t < (n+1)T \end{cases} \tag{2.7}$$

Note that z is complex $(x+iy)$, b is the real coordinates of the center of the vortices, and $n = (0, \pm 1, \pm 2, ...)$ is the number of blinks. The flow field is bounded to a circular disk by including an image vortex at $a^2/\overline{z}(t)$ where the overbar indicates the complex conjugate and a is the radius of the bounding edge. The strength of the agitating vortex is given byΓ while the image has a strength of $-\Gamma$. Following *Aref* (1983), a particles' motion, $\dot{\overline{\zeta}}$ is given by:

$$\dot{\overline{\zeta}} = \frac{\Gamma}{2\pi i}\left[(\zeta - z)^{-1} - (\zeta - \frac{a^2}{\overline{z}})^{-1}\right] \tag{2.8}$$

Substituting the location of the first stirrer, $+b$, (2.8) becomes

$$\dot{\overline{\zeta}} = \frac{\Gamma}{2\pi i}\frac{b^2 - a^2}{(\zeta - b)(\zeta b - a^2)} \tag{2.9}$$

The particle trajectory follows the arc of a circle with known radius:

$$\rho = \frac{\lambda}{1-\lambda^2}\left(\frac{a^2}{b} - b\right) \tag{2.10}$$

centered at

$$\zeta_c = \frac{b - \lambda^2 a^2/b}{1-\lambda^2} \tag{2.11}$$

where λ is a constant $(0 \ < \lambda \leqslant b/a)$ related to the initial position, ζ_0. Given that ζ_0 is known, the angle through which the particle is rotated around the vortex is all that is required to find the final location at time $T/2$. This requires the solution of the implicit

equation:

$$\zeta = \zeta_c + \rho e^{i\phi} \tag{2.12}$$

due to the presence of the image vortex which causes particles to rotate in circles around a point that is not at the center of the blinking vortex.

A similar derivation is required for the period when $t \geq T/2$. Alternatively, *Aref* (1983) observes that the particle position in this second time period can be found using only the first stirrer located at $z = +b$. This is accomplished by inverting the particle's position at $t = T/2$ and then evolving the particle through $T/2 \leq t < T$ as though the stirrer was still at the original position. Finally, $\zeta(T)$ can be determined by then inverting the final position. This is shown in panel (a) of Figure 2.1.

The resulting trajectories of particles within Aref's time varying, highly analytical flow fields look relatively uncomplicated. Figure 2.1 illustrates typical trajectories calculated using the above equations. However, if multiple particles are released in this field, and their positions are only shown at time intervals separated by T, the solutions can become much more complicated as shown in Figure 2.2. Recall that this in case there is no diffusive component, and yet after a relatively short period, particle positions are reminiscent of those resulting from diffusion. Aref termed this effect "Lagrangian Chaos".

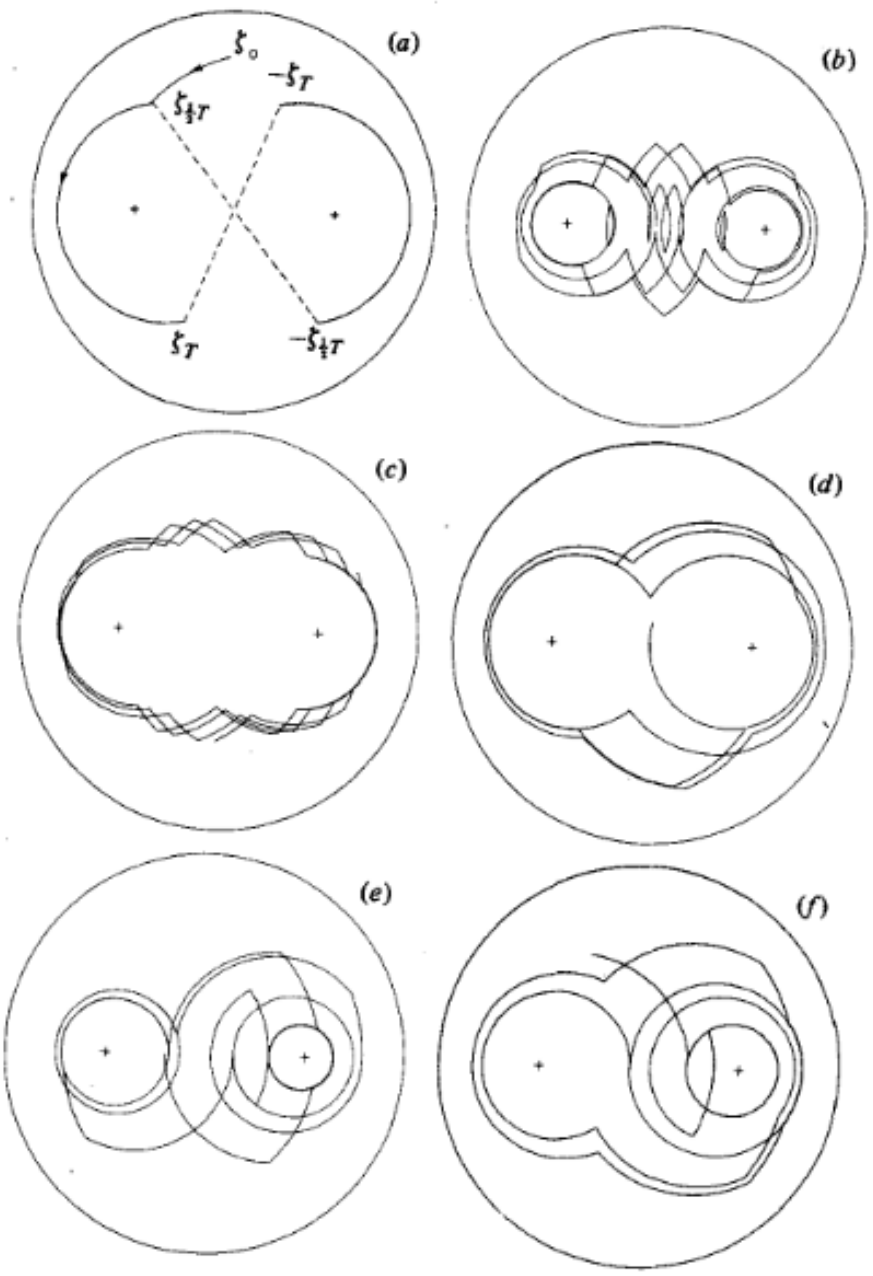

Figure 2.1: Particle trajectories according to Aref's blinking vortex. Panel (a) shows a method of trajectory calculation in which only the first stirrer (at $z = +b$) is used, and particle locations are inverted to find actual positions. Panels (b through f) show examples of particle trajectories for different starting locations. Crosses indicate the centers of the vortices and rotation is always in the counterclockwise direction. From *Aref* (1983).

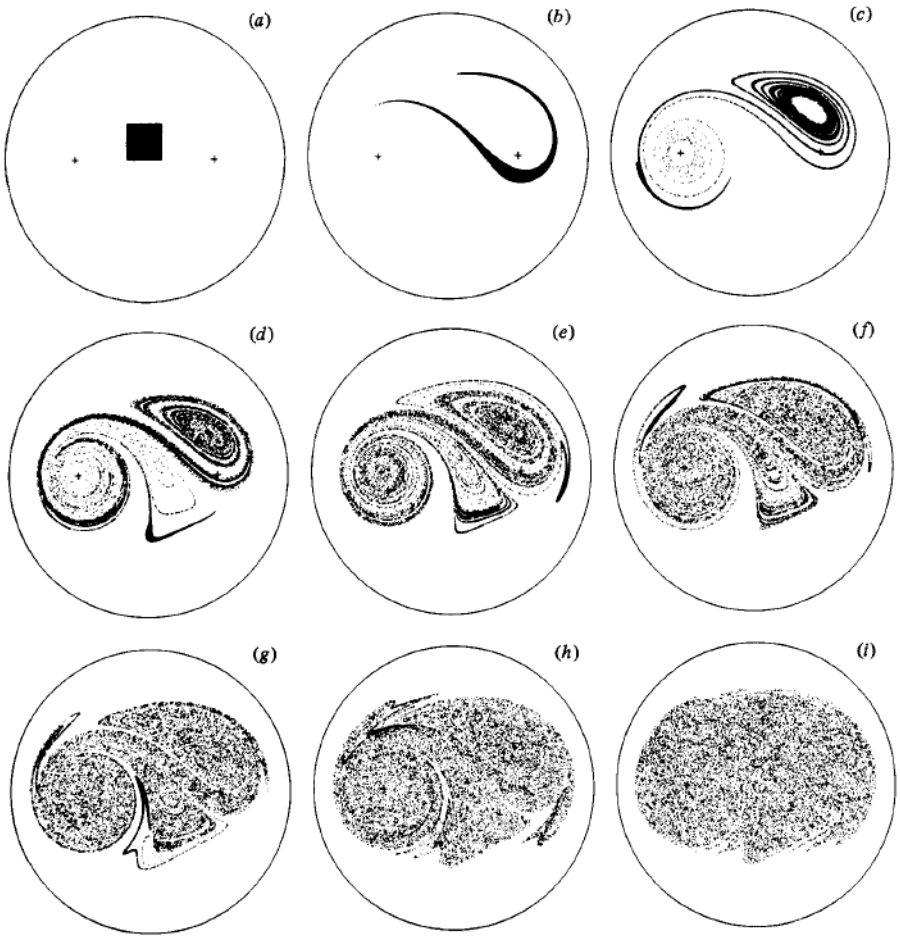

Figure 2.2: Lagrangian Chaos: Locations of particles initiated at t_0 in a square, at various stages during the stirring process. T is one; panels shown are a t times (a) t = 0; (b) 1; (c) 2; (d) 3; (e) 4; (f) 5; (g) 6; (h) 9; (i) 12. From *Aref* (1983).

2.2 Surprising Consequences of Spatial Variations in Diffusivity

The second example illustrates the difficulty of modelling trajectories when only the diffusive component is considered. In this case (2.2) becomes:

$$\frac{dx}{dt} = \epsilon(x,t) \tag{2.13}$$

There are many different approximation schemes to solve (2.2). Approximations can be either explicit or implicit. Explicit means the advective component is approximated using only the current state of the flow fields while implicit uses future states as well (*Haidvogel and Beckmann*, 1999). There are many examples of approximation schemes including Forward and Backward Euler, Trapezoidal, Leapfrog, Adams-Bashforth, and Runge-Kutta (*Haidvogel and Beckmann*, 1999; *Press et al.*, 1999). This is by no means an exhaustive list. Each of these methods can be combined and/or applied to approximate advective forces through space and/or time. In the simplest of these examples, the Forward Euler method, particle position is given by:

$$x_{n+1} = x_n + \Delta t F_n$$

where F_n corresponds to the right hand side of (2.2).

Note that the use of the most simple approximation scheme, the Forward-Euler ("naive" random walk method) can falsely aggregate particles in areas of low diffusivity. This method describes the change in position from x_n to x_{n+1}:

$$x_{n+1} = x_n + \epsilon\sqrt{2D(x_n)\sigma_\epsilon \Delta t} \tag{2.14}$$

over the finite timestep, Δt and where ϵ is some normal random process with mean 0 and standard deviation, 1 (*Visser*, 1997). To avoid false aggregation (2.14) must be corrected using a D' term which relates to the spatial gradient of the diffusivity (*Visser*, 1997). The corrected random walk model is described by *Visser* (1997) as:

$$x_{n+1} = x_n + D'(x_n)\Delta t + \epsilon\sqrt{2D(\overline{x}_n)\Delta t} \tag{2.15}$$

where D' represents $\partial D/\partial x$, the gradient of diffusivity and $\overline{x}_n$ is given by $x_n + \frac{1}{2}\frac{\partial D}{\partial x}|_{x=x_n}\Delta t$. In this case, D' becomes a non-random, pseudo-velocity term which counteracts false aggregation in areas of low diffusivity.

The diffusivity profile is shown in Figure 2.3 with a subsurface minimum of diffusivity (*Visser*, 1997). The results of the naive model, shown in Figure 2.4, demonstrate how particles eventually aggregate at depths between 10 and 20 m, corresponding to the low diffusivity zone. The second panel of Figure 2.4 demonstrates how the addition of the pseudo-velocity term, D', eliminates this false aggregation.

These results have been corroborated by *North et al.* (2006) and *Hunter et al.* (1992). The latter found that this false aggregation could also be corrected by remapping the spatial coordinate to create a transport equation with constant diffusivity. However, this technique is not covered in more detail in this thesis.

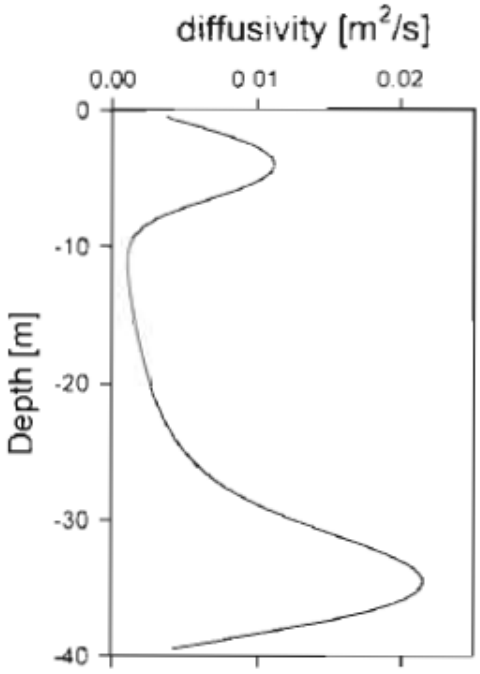

Figure 2.3: Diffusivity profile defined by *Visser* (1997). The water column depth is 40 m. This profile is simulating a "surface wind stress corresponding to a wind speed of about 9 m s^{-1}, a tidal current of amplitude 0.5 m s^{-1}, moderate stratification: a vertical difference of 0.15 kg m^{-3} over a 15 m pycnocline separating vertically well-mixed surface and bottom layers" (*Visser*, 1997).

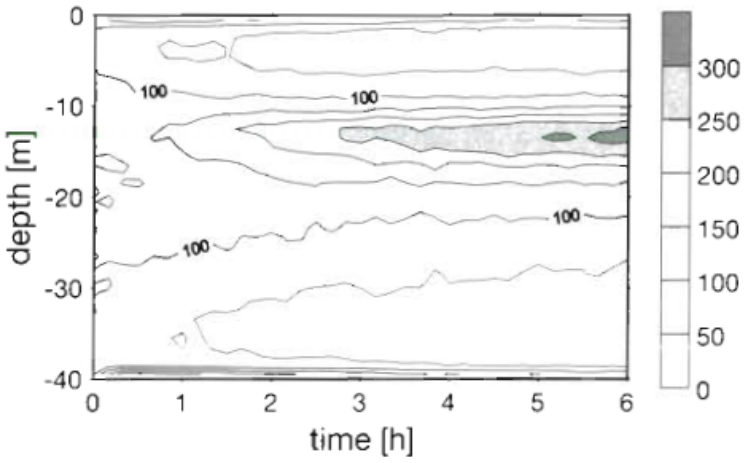

(a) Naive Random Walk

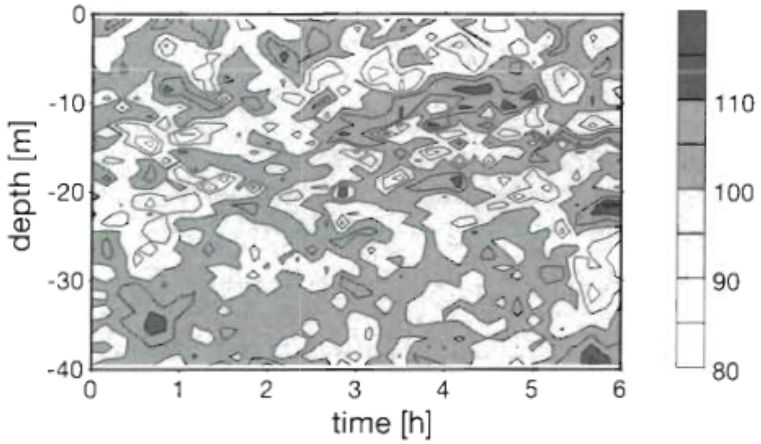

(b) With advective (D') term added

Figure 2.4: Examples of the false aggregation of particles in a zone of low diffusivity when particle locations are calculated using a naive Euler method and the results when a false advection term added. Colorbar to the right indicates numbers of particles. A perfectly uniform distribution would show 100 particles m^{-1}. From *Visser* (1997).

2.3 Practical Considerations

AVAILABILITY OF TRACKING SOFTWARE: As discussed above, particle tracking uses the output from ocean circulation models to predict the movement of particles from a Lagrangian perspective. While pdf's are very useful, they are not covered in any more detail in this thesis. Particle tracking methodology can be divided into two types of methods: those that track in discrete time and those that track in discrete space. A comprehensive list of contemporary particle trackers can be found at http://www.nefsc.noaa.gov/drifter/particles.html (*Lynch et al.*, 2015). Regardless of the particle tracking method, the general process involves three key components. The direction and magnitude of the advective element must be approximated at a particular location and time, x_n within a given grid. A stochastic component must be added, and the distance travelled by a particle must be calculated. The combination of these three components results in the final location, x_{n+1} (*Lynch et al.*, 2015).

CHOICE OF TIME STEP: For DT methods, the frequency of approximations is dictated by the timestep, Δt. Path calculations are only made at the given Δt and location is determined at each subsequent Δt. It is important that an appropriate Δt is selected such that, in the gridded situation, particle paths are not skipping over several grid boxes in one iteration (*Lynch et al.*, 2015). Other schemes, such as Runge-Kutta, can actively determine an appropriate Δt without specification by the modeller.

CHOICE OF GRID: DS methods use grid spacing to determine the frequency of approximation. This allows analytic specification of the trajectory of a particle within a grid box given specified boundary flows. This is a great simplification to the DT method. Both of these methods will be covered in detail in Chapter 3 through the detailed breakdown of existing particle tracking models corresponding to each type. Note that the grid definition will modify the discretization of flow fields. Specifically, discrete difference grids (grid

boxes are quadrilateral), can be handled differently than discrete element grids (grid boxes are triangular) *Lynch et al.* (2015). In the case of discrete difference grids, velocities are approximated in different locations along the edges or centers of the boxes. *Arakawa and Lamb* (1977) list the different types for discrete difference grids, however, this thesis focuses on the Arakawa C grid.

ADDING A RANDOM COMPONENT: There are different methods for adding the stochastic component. Among others, there are four different "random walks", depending on levels of autocorrelation, that can be used (*Lynch et al.*, 2015). The simplest version is memoryless; stochastic additions are not correlated with previous ones. A random component is added to particle position directly, and chosen from a distribution which can be described by:

$$\epsilon \sim \sqrt{2D\Delta t}N(0,1) \tag{2.16}$$

where N is a normal distribution (*Lynch et al.*, 2015). More advanced versions allow for correlation between the current and previous random component addition through the addition of the random component to the advective component directly.

PARTICLE PERSONALITY: The simplification of a massless, chemically and biologically inert particle is sufficient for particle tracking in highly idealized scenarios. However, for practical purposes further criteria and modelling constraints must be specified. For example, modelling an oil spill requires a variation of (2.2) that is different from one used to determine residence times in deep basins. Boundary effects (should particles stick or reflect?) must also be considered.

FORWARD OR BACKWARD TRACKING: As discussed in the Introduction, particle position can be calculated using a combination of predetermined advective fields with stochastic non-reversible diffusive components (*Isobe et al.*, 2009). The reverse, finding

out where things come from (sources), is even more complicated due in part to the non-reversible nature of the stochastic component. Additionally, finding source regions can not simply be reduced to reversing the advective components due to the existence of converging flow fields in the reverse time field (*Isobe et al.*, 2009). However, it is possible to find sources using forward running models. These methods are usually iterative and can require a lot of time to run.

CHAPTER 3

PARTICLE TRACKING IN DISCRETE TIME AND SPACE

Discrete time (DT) tracking methods calculate the distance a particle will travel under the influence of a flow field over a specified time interval (*Lynch et al.*, 2015). In general, a decrease in the time interval will lead to more accurate predictions. Discrete space (DS) trackers use analytic expressions for a trajectory within a given grid box that is part of a larger-scale spatial discretization. As expected, a decrease in grid box size increases the accuracy of prediction. This chapter provides a description of two existing models as examples of the two methods.

3.1 Description of Particle Tracking in Discrete Time

The LEEWAY model is used by the Norwegian Joint Rescue Coordination Centre (JRCC) to generate search and rescue (SAR) target areas using the DT method. The challenge in any search and rescue operation is to reduce the number of unknowns so that the generated SAR zone has a high probability of containing the SAR target, but that is not so large as to overtax the SAR resources. LEEWAY utilizes a Runge-Kutta time scheme to track a Monte Carlo based stochastic ensemble of trajectories to approximate a search area (*Breivik and Allen*, 2008). To generate a realistic search area, relevant variables (e.g., wind, surface currents and the characteristics of the object of the search) must be accurately quantified.

An ensemble of numerical integrations are performed where the various parameters are perturbed in a stochastic fashion thereby generating a cloud of candidate positions for the drifting object.

The motion of an object drifting on a body of water results from the external forces acting on the object and factors affecting the center of mass (*Hackett et al.*, 2006). Forces acting externally on the object include water currents, surface winds, wave motion and wave induced currents. Factors effecting the center of mass include gravity and buoyancy. The position of a floating object can be computed by integrating the total drift velocity, u_{drift}, of an object given by

$$u_{drift} = u_{curr} + u_L \tag{3.1}$$

where u_{curr} is the ocean current velocity relative to the Earth and u_L is the object's drift velocity relative to the ambient water. The current velocity, u_{curr}, has two main components: Stokes drift associated with the surface gravity waves and surface current (*Hackett et al.*, 2006). The Stokes drift term is the net drift of a fluid parcel or free floating object in the direction of surface gravity wave propagation (*Stokes*, 1880). The second component, the surface current, includes four main components: Ekman drift, mean barotropic/baroclinic motion, tidal and inertial currents (*Hackett et al.*, 2006). Ekman drift is a current induced by the balance of the wind generated shear and the Coriolis force (*Ekman*, 1905). This force balance results in a surface current induced at an angle to the prevailing wind direction. Baroclinic motion is the portion of the surface current that results from horizontal inhomogeneities in the stratification of the ocean (*Gill*, 1982). The final two types of surface currents are those induced mainly by tidal forces and the wind; both are influenced strongly by the rotation of the Earth (*Gill*, 1982).

The second component of the total drift velocity, u_L is the drift resulting from the wind and wave forces acting directly on the object. It is strongly dependent on the characteristics

of the object including its shape. The change in position of an object within this frame is then given by

$$\frac{dx}{dt} = \int_0^t \left[u_L(t) + u_{curr}(x,t)\right] dt \tag{3.2}$$

(*Breivik and Allen*, 2008). As noted earlier, the integration of this equation is not trivial as u depends on x.

For the purposes of this model, the word leeway, distinct from the model name, LEEWAY, is defined as: "the drift associated with the wind force on the overwater structure of the object as measured relative to the 10 minute averaged wind measured at 10 m height." (*Breivik and Allen*, 2008). This drift occurs at an angle to the prevailing wind and can be decomposed into a downwind and crosswind component. *Breivik and Allen* (2008) demonstrate that there is an almost linear relationship between the 10 m wind speed and the two separate components of the leeway. Therefore, results of a linear regression are used to calculate each component based on the 10 m wind speed. For example, the downwind leeway velocity is statistically modelled by

$$u_L^d = a_d W_{10} + b_d \tag{3.3}$$

where a_d and b_d are regression coefficients determined from experimental data for varying classes of objects (*Breivik and Allen*, 2008). Leeway coefficients are adjusted by adding a perturbation, ϵ_n, drawn from a normal distribution. This perturbation is included as higher wind speeds result in higher variance in the regression line. The downwind leeway component for the nth ensemble member is then expressed as

$$u_{Ln}^d = \left(a_d + \frac{\epsilon_n^{(1)}}{20}\right) W_{10} + \left(b_d + \frac{\epsilon_n^{(2)}}{2}\right) \tag{3.4}$$

Leeway coefficients a_d and b_d, for many different classes of objects, are provided in Allen and Plourde's 1999 report. The offset, b_d, is zero in all cases which, in the absence of wind, allows the object to move with the local surface current, u_{curr}, only. It is included to allow the addition of ϵ_n, because a SAR object is likely to drift faster or slower than a test object (*Allen and Plourde*, 1999). The above equation is tailored for the specific case of a drifting life raft. The relative weighting of ϵ_n depends on the category of drifting object and must be altered to fit the linear regression provided. *Breivik and Allen* (2008) also conclude that the dispersion caused by error variance of the leeway properties is two orders of magnitude larger than the dispersion caused by the wind and current perturbations. Therefore they argue that a simple stochastic model, such as the random-walk, is sufficient to account for these variances.

The final variable key to the success of a SAR operation is the last known position of the object in question. LEEWAY uses eight parameters to account for unknowns in this position. Here the subscript "0" denotes the earliest possible time of the accident and "1" denotes the latest possible time. The eight factors are then the two possible times, t_0 and t_1, most likely positions, $[x(t_0),\ y(t_0)]$ and $[x(t_1),\ y(t_1)]$ (in latitude and longitude), and the radii of uncertainty of position, $r(t_0)$ and $r(t_1)$ (*Breivik and Allen*, 2008). The model then deploys ensemble members with starting positions drawn from a normal distribution with a standard deviation of $r/2$ where r varies linearly from r_0 to r_1. The result is a cone shaped initial distribution of release positions scaled to the extremes in time and space of the accident time frame as shown in Figure 3.1. As uncertainty in the last known position grows, so does the cone of possible initial release points. An example of the type of output generated by LEEWAY is shown in Figure 3.2.

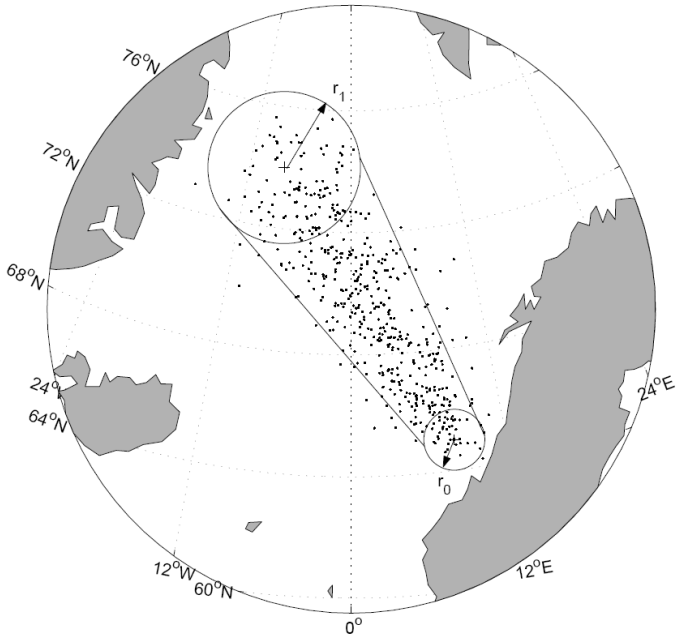

Figure 3.1: Cone of initial distribution of release positions from t_0 to t_1. These times coincide with r_0, the radius of uncertainty of the earliest possible time of accident and r_1, the radius of uncertainty of the last possible time of the accident which are centered at $[x(t_0),\ y(t_0)]$ and $[x(t_1),\ y(t_1)]$ respectively. The distance between r_0 and r_1 corresponds to the potential distance traveled between t_0 and t_1. Taken from (*Breivik and Allen*, 2008).

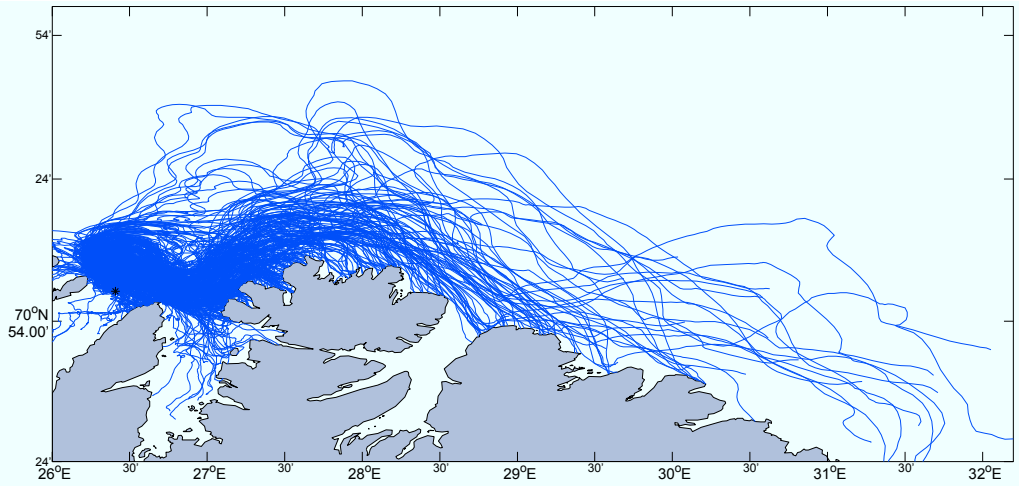

Figure 3.2: Typical trajectory output from the DT particle tracker Leeway off the coast of Norway. 500 particles were released instantaneously in a 1 km radius centered on the black x and allowed to drift for 8 days. The SAR region generated would encompass all of the end points of all of the generated trajectories.

The LEEWAY code has been used for backtracking drifting objects using an iterative algorithm based on the forward trajectory model (*Breivik et al.*, 2012). This method, called "BAKTRAK" is used to determine most probable origin of an object determined by a known final position. Specifically, the LEEWAY trajectory model is initialized and run in the forward direction. An initial seeding of "parent particles" is released in a two dimensional circular normal distribution based on a first guess radius. Time of release is also varied, based on a uniform distribution, resulting in a range of initial start positions and start times. Particles are seeded starting from the earliest start time and continue to be seeded in successively smaller radii around the target. Particles that are released closer to the final position, called the Target Area (TA), are more likely to be successful at reaching the TA. Therefore, particles are selected to become a "parent seeder" for successive runs based on a relative distance to the TA. In the event that at the end of the first iteration too few particles have reached the TA, the nearest particles (based on relative distance) are used. Once successful "parent particles" have been selected, "children" particles are seeded according to a radial Gaussian distribution about their respective parent particle initial position. The iteration stops when 100 particles have come within a determined time/space radius of the TA. Breivik et al. report this typically occurred within 5-8 successive BAKTRAK runs (*Breivik et al.*, 2012).

LEEWAY uses a Runge-Kutta integration scheme. In this study two Matlab based schemes are used: one based on Runge-Kutta and a simpler (Forward Euler) scheme that is used to highlight some of the problems that can arise with the use of "naive" integration schemes. The Forward Euler is explicit in time and space and therefore only relies on the current state of the velocity fields *Haidvogel and Beckmann* (1999). Under this scheme, (2.2) becomes

$$\Delta x = u(x_n, t_n)\Delta t + \epsilon(x_n, t_n) \tag{3.5}$$

This interpolation scheme was used in the Matlab DT method that will be used to compare the performance of DS and DT methods in Section 3.2.

3.2 Description of Particle Tracking in Discrete Space

Another method of particle tracking involves the analytical specification of trajectories or streamlines across a fixed velocity grid. One example of this DS type of particle tracking is *Blanke and Raynaud* (1997)'s program, "Ariane". The Ariane program is extremely fast and efficient as it relies on exact, three-dimensional streamlines within each box of a three-dimensional grid. To illustrate, consider a two-dimensional, single box within a larger 2D grid in a steady, unchanging velocity field. Velocity is defined in the center of each side of the box as in an Arakawa C grid, and is assumed to vary linearly from one face of the box to the opposite face (*Arakawa and Lamb*, 1977). At any point within that box, velocity can be expressed as a proportion of the change in velocity between the two faces. In 1D, a particle will either accelerate or decelerate directly across the box as dictated by the flow fields. According to this approximation, at any point within the grid box, the velocity in the x direction is given by

$$u(x) = u_0 + \frac{u_1 - u_0}{L}(x - x_0) \tag{3.6}$$

where x_0 is the left boundary of the cell, u_0 is the velocity at the left boundary, u_1 is the velocity at the right boundary, and L is the length of the side of the box. A similar equation is derived for the y-direction velocity components. A particle initiated at any starting position within a given grid box will follow a predetermined streamline as illustrated in Figure 3.3 below. These streamlines determine the exact exit location of a particle. Each grid box can be imagined to contain an infinite number of predetermined streamlines depending only on the flow fields defined at the edges and the starting position.

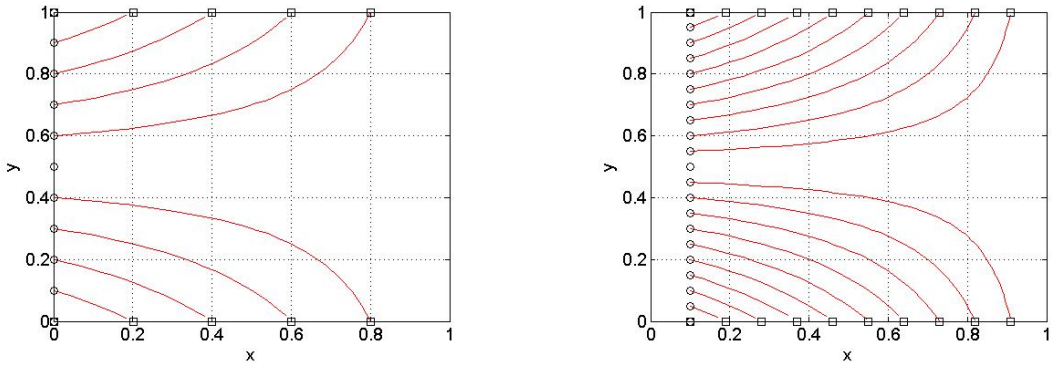

(a) Streamlines of 11 particles initiated at $x = 0$ (b) Streamlines of 21 particles initiated at x=0.1

Figure 3.3: Trajectories inside a single box with a steady flow field calculated using the DS method. Note inside the box the flow field is defined as: $2 \leqslant u \leqslant 0$, and $-1 \leqslant v \leqslant 1$. Particle initiation point is indicated by the open circles and exit locations by open squares.

The Ariane methodology initially determines the time required to transit the box by combining only the advective portion of (2.2):

$$\frac{dx}{dt} = u(x_n) \tag{3.7}$$

with (3.6) and rearranging and integrating. *Blanke and Raynaud* (1997) define the crossing time as the time required for a particle to move directly across one given cell in any direction, from any starting position within the cell, to the "exiting" grid box edge. The crossing time is given by

$$t_c = \frac{1}{\Delta u} \log \left(\frac{u_1}{u_0} \right) \tag{3.8}$$

where Δu is the difference in velocity in the x-direction ($u_0 - u_1$). A similar expression can be found in the y direction and this allows the shortest crossing time to be calculated. The smallest number defines the time a particle will actually spend within the box as well as the face the particle will exit. For example, assuming a particle crosses in the y-direction more quickly, then time to exit in the y-direction becomes t_c and therefore the exit face will be on the north or south side of the cell. Knowing the exit face, and again manipulating (3.6) and (3.7), *Blanke and Raynaud* (1997) find the final location of the particle in the

other direction, x_f, can be calculated by substituting the shortest crossing time into

$$x_f = \frac{u_0}{\Delta u} \left[\exp(\Delta u \; t_c - 1)\right] \tag{3.9}$$

This exit location from one grid box becomes the initial position for the next grid box and the process repeats. In a time varying flow field, there are two possibilities for particles within a grid box. The first is the particle crosses the grid box within the duration of a flow field and continues through to the next. The second, the particle does not exit the box before the expiration of the current flow field and an interim location within the grid box is stored. The flow fields then switch and the particle continues its path either crossing the box or remaining inside.

Blanke and Raynaud's particle tracking program, Ariane, was recreated using Matlab for the purposes of fully understanding their method. Through this reproduction it became apparent that, along with reduction of computational requirements, trajectory consistency is also a strength of the Ariane algorithm. As an extension of Ariane, the option of adding dispersion in the Matlab version of Ariane is explained in the next section.

3.2.1 Adding Dispersion to Ariane

Ariane is an excellent tool for long time scale integrations, however, it does not include a way of accounting for grid-scale turbulence, or small scale variations that are not accounted for in the flow fields, as in the LEEWAY model. *Fisher et al.* (1979) describe how the concept of Fickian diffusion can be used to simulate environmental dispersion. To see how this applies to a very simple situation, assume small scale dispersion is added to a flow field by adding a random velocity component that displaces a particle by a random amount denoted by ε. If the particle is initially released at x_0 and subsequently experiences n random steps then the particle will have a final random location given by $x_n = \varepsilon_1 + \varepsilon_2 + ... + \varepsilon_n$. This readily generalizes to two dimensions if we treat the particle's position and random

displacement as column vectors, e.g.,

$$\varepsilon_n \equiv \left[\begin{array}{c} \varepsilon_i \\ \\ \varepsilon_j \end{array} \right]_n \tag{3.10}$$

In general the expected value of the particle's displacement at time n is assumed to be zero and its covariance is

$$cov(\epsilon_i, \epsilon_j) = \begin{cases} 0 & \text{if } i \neq j; \\ \sigma^2 & \text{if } i = j. \end{cases} \tag{3.11}$$

It is straightforward to show that the expected value of the particle's position at the nth time step is zero and the variance of the position is

$$\mathrm{var}(x_n) = n\sigma^2 \mathrm{I} \tag{3.12}$$

where I is the 2×2 identity matrix. In one dimension, the expected value of the x position at the nth time step is zero and the variance is simply

$$\mathrm{var}(x_n) = n\sigma^2 \tag{3.13}$$

This implies that the standard deviation in particle position is $\sqrt{n}$.

The first step in adding dispersion to the Ariane was to generate a flow field of random velocities that generated a non divergent flow. This was achieved by first creating a gridded field of random stream function values (henceforth denoted by ψ). The ψ values are defined at the corners of the grid boxes and were scaled using a factor of σ_ψ:

$$\sigma_\psi = \alpha^2 \frac{L^2}{\Delta t} \tag{3.14}$$

where α is a scale factor, L is the size of the (square) grid box and Δt is the time step controlling when the random flow field changes. From this set of ψ values, the velocity fields across the side of each box are created using

$$u_0 = \frac{\psi_3 - \psi_1}{L} \tag{3.15}$$

and similarly for the y-direction.

The standard deviation of particle position can now be calculated using the standard deviation of the velocity:

$$\sigma = \sigma_u \Delta t \tag{3.16}$$

The velocity in the middle of each grid cell, considering only the x-direction for simplicity, can be approximated by

$$u_m = \left[\frac{\psi_4 - \psi_2 + \psi_3 - \psi_1}{2L} \right] \tag{3.17}$$

and thus the standard deviation of the velocity in the center of the cell is

$$\sigma_u = \frac{\sigma_\psi}{L} \tag{3.18}$$

The variance in particle position in one dimension due to the psi values then becomes

$$\mathrm{var}(x_n) = n(\sigma_u \Delta t)^2 = n(\alpha L)^2 \tag{3.19}$$

This the variance in position grows linearly with time $n\Delta t$ with a scale factor D:

$$var(x_{in}) = D\ t \tag{3.20}$$

where

$$D = \alpha^2 \frac{L^2}{\Delta t} \tag{3.21}$$

can be interpreted as a diffusion coefficient.

The above concepts are illustrated in Figure 3.4 which shows the dispersal of an ensemble of particles from their release point in the absence of any background velocity field. The variance of particle position in each dimension is very close to what is predicted by (3.21). The effect of using an inappropriately scaled values of D is illustrated in Appendix A.

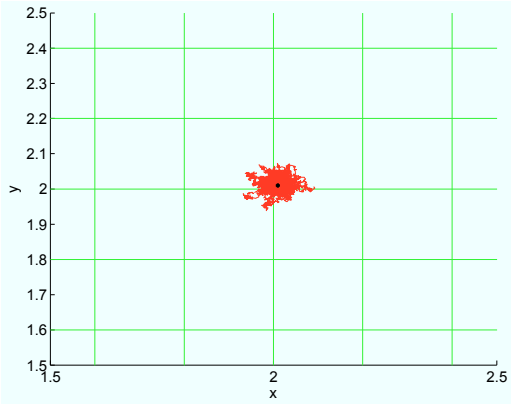

(a) $D = 6.25x10^{-7}$; $t = 100$ hours

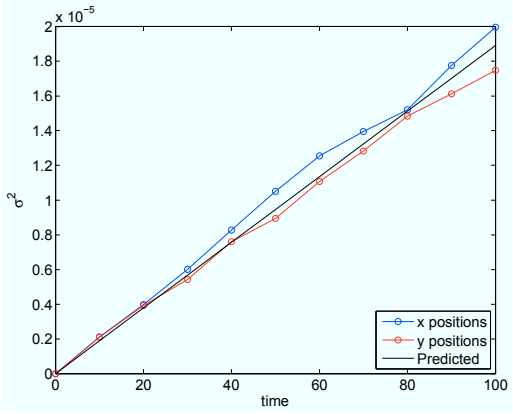

(b) σ^2 vs time; $D = 6.25x10^{-7}$; $t = 100$ hours

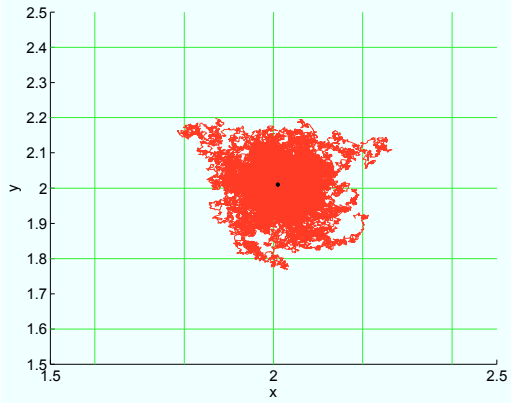

(c) $D = 6.25x10^{-7}$; $t = 10,000$ hours

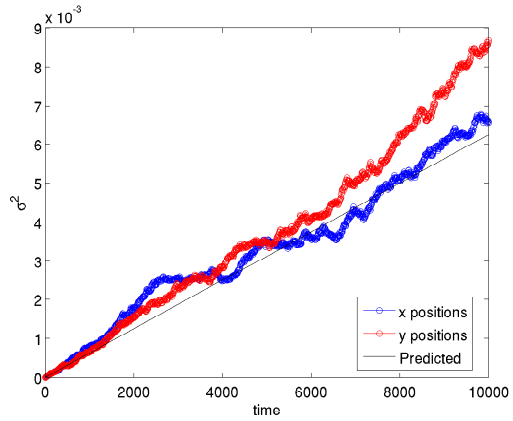

(d) σ^2 vs time; $D = 6.25x10^{-7}$; $t = 10,000$ hours

Figure 3.4: Adding dispersion to Ariane. 500 particles were released at point (2,2) indicated by the black cross. The left panels show particle trajectories calculated using the DS method in a purely dispersive flow at time (a) $t = 100$ and (b) $t = 10,000$. The right panels show the variance of the ensemble of particle positions as a function of time assuming constant D. The blue(red) line shows the variance of $x(y)$ position at time (c) $t = 100$ and (d) $t = 10,000$. The theoretical predictions by (3.20) are shown by the black line. α is 1.

CHAPTER 4

EVALUATING DT AND DS TRACKING USING IDEALIZED EXAMPLES

The efficiency of particle tracking using discrete time and discrete space methods is now compared and contrasted using the two idealized examples discussed in Chapter 2 as well as a simple, single vortex. The trajectory around such a vortex is straightforward to calculate, both numerically and analytically. Aref's blinking vortex, or a purely dispersive flow given a spatially varying diffusivity, lead to more complicated results (e.g., Lagrangian chaos and false aggregation of particles) but they can still be readily calculated and compared against analytical expectations (*Aref*, 1983; *Visser*, 1997). The performance of a method within these idealized examples indicates how reliable its results might be in more complicated settings, e.g., with realistic coastlines and bathymetry.

The remainder of this chapter will feature results generated using the Matlab codes created to mimic Ariane and LEEWAY. It is important to note, as discussed in Chapter 3, LEEWAY has significant randomness added to both wind and velocity fields which makes it an effective search and rescue tool. However, the intent in this Chapter is to evaluate the effectiveness of the DT model against idealized examples. Therefore, the random variables and the leeway coefficients, $a_{c,d}$ and $b_{c,d}$, have been set to zero.

4.1 Circular Vortex

Consider a simple, steady vortex defined on a regular square grid. The true trajectory is circular and is centered on the vortex's center; (50, 50) in this example. The trajectory will repeat circular orbits indefinitely. When using numerical tracking schemes, the accumulation of computational errors typically results in the degradation of the circular trajectory.

The trajectory calculated using the DT particle tracking model is shown in Figure 4.1. In this example, one particle was initiated at (25, 55) as indicated by the black circle. Plotting the x and y position for different times (right hand panels) is an effective way of showing that the particle has made repeated rotations about the origin and demonstrates the slight degradation of the trajectory on each revolution. The particle's trajectory was calculated for 5000 time units with a dt of 0.1. As expected, the accumulation of errors decreases as the dt of each calculation decreases. This is demonstrated in Figure 4.2.

The results of the DS integration around the single vortex are shown in Figure 4.3. The DS trajectory of a particle follows an exact path repeatedly around the center of the vortex. Even though the grid shown in Figure 4.3 is fairly coarse (dx is 2), there is no degradation of the track as when calculating the same trajectory with the DT method (Figure 4.1). However, for the DS method, decreasing the grid spacing would improve the accuracy in more complicated scenarios such as time varying flow fields.

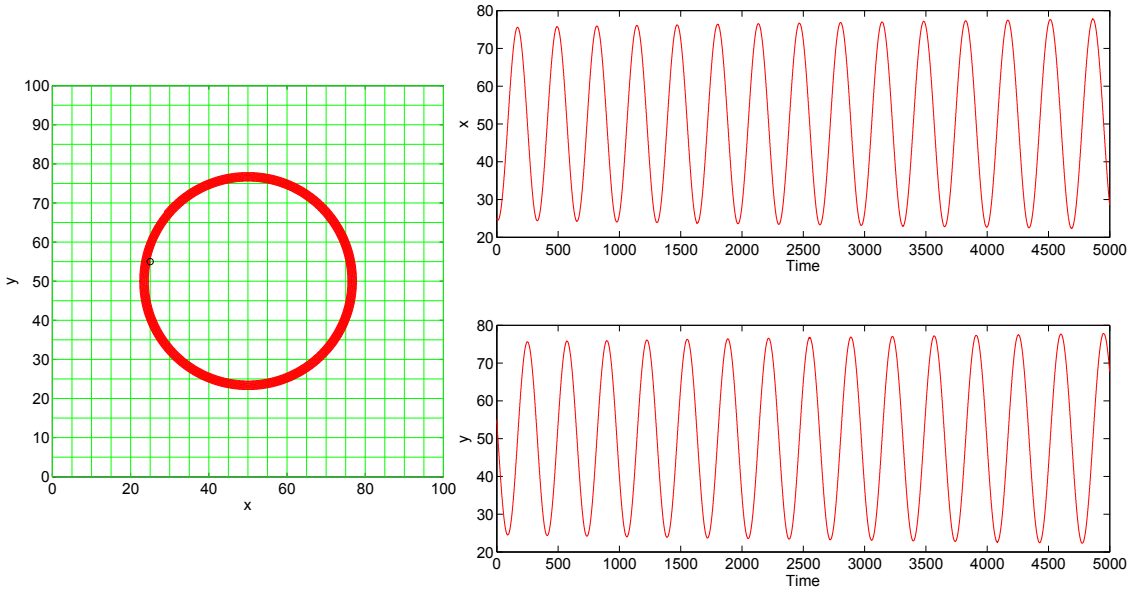

Figure 4.1: Trajectory calculated using the DT method in a simple vortex (left hand panel). The vortex is centered at (50, 50) with the initial release point at (25, 55) indicated by the black circle. The right hand panels show the change in x and y position with time, revealing the number of revolutions around the vortex origin. In addition, with each revolution around the vortex there is a slight degradation of the trajectory resulting from an accumulation of errors. In this example dt is 0.1 and the calculation is for 5000 time units.

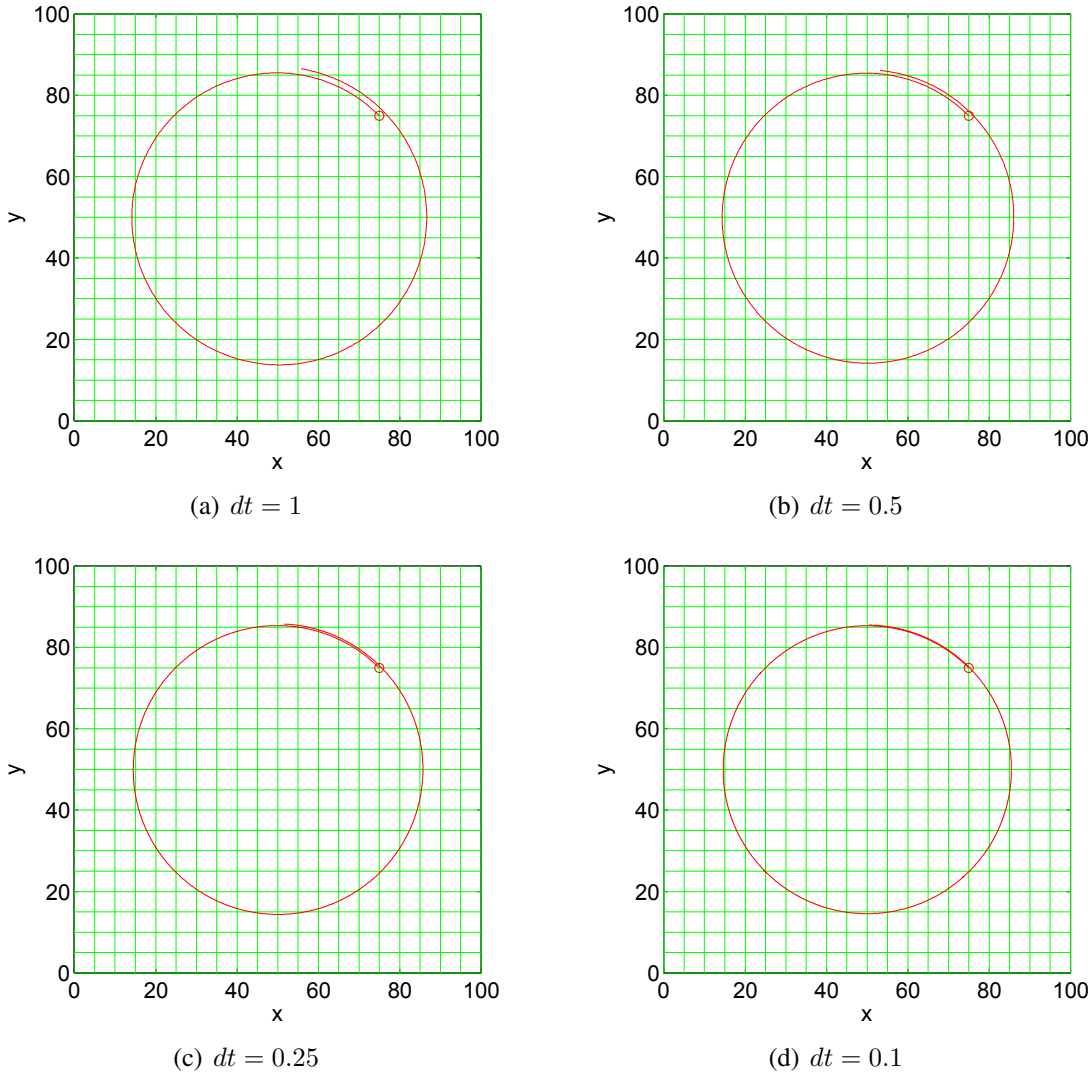

(a) $dt = 1$

(b) $dt = 0.5$

(c) $dt = 0.25$

(d) $dt = 0.1$

Figure 4.2: Effect of time step on accuracy of a trajectory calculated using the DT method. Particle trajectories around a steady vortex are calculated using the DT model with increasing values of dt: (a) 1, (b) 0.5, (c) 0.25, (d) 0.1. As dt is increased, accumulation of errors increases. The particle release point is indicated by the red circle at (75, 75). The vortex was centered at (50, 50).

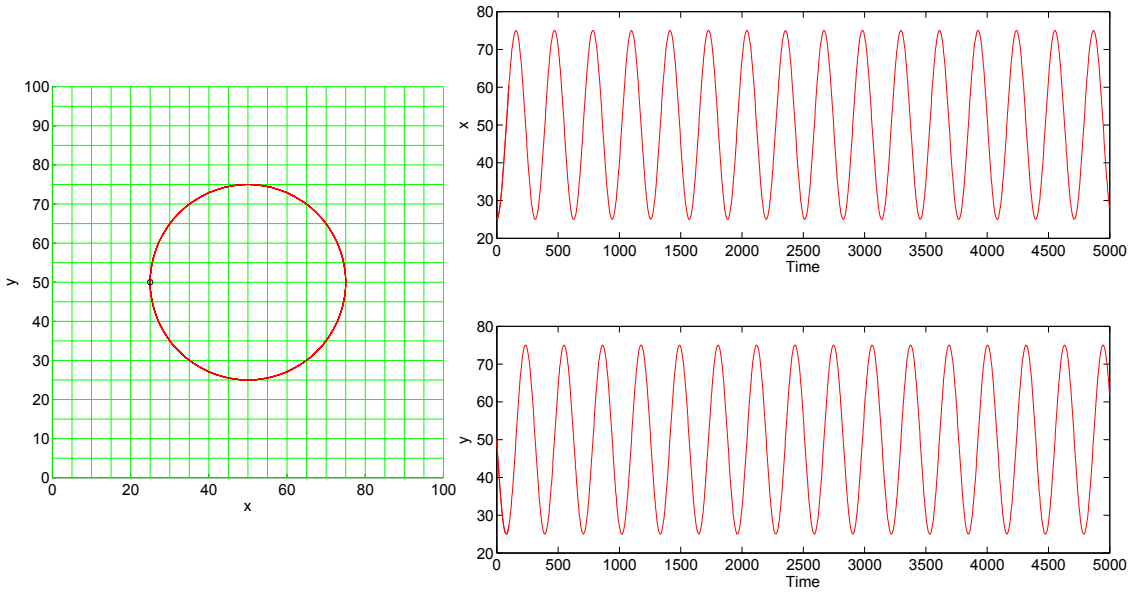

Figure 4.3: Particle trajectory around a single vortex calculated using the DS method. With each revolution around the vortex there is negligible degradation of the trajectory. Grid boxes have size: L is 2. Otherwise as in Figure 4.1.

4.2 Aref's Blinking Vortex

The previous section deals with a velocity field that is time independent. The addition of time dependence to flows considerably complicates the predictions. Trajectories calculated analytically, using Aref's method described in Section 2.1, are compared with particle trajectories calculated using the DT model in Figure 4.4. As expected, the model's accuracy increases as the dt decreases. However, each decrease in dt results in an increase in computational time. Therefore, a balance must be struck between the level of accuracy and the period of time available to run the model. It can be seen in Figure 4.4 that the error in the DT method arises when the velocity changes in a discontinuous fashion.

Similarly, trajectories calculated analytically using Aref's method described in Section 2.1 are compared with particle trajectories created using the DS model is shown in Figure 4.5. For the DS method, the accuracy of the trajectory is increased by decreasing the grid spacing. It is important to note that the DS method calculates a more accurate trajectory for smaller decreases in grid spacing than the equivalent decrease in dt in DT models. However, for the DS method,the amount of memory becomes the issue rather than computational time. As the size of the grid boxes decrease, the size of the flow fields must increase in order to encompass the same area. A strength of the DS method is that the increase in computational time occurs in the calculation of the flow fields and not as significantly in the calculation of trajectories. Considering there are only 2 flow fields for the duration of this run the DS method maintains a high level of accuracy for a fast calculation time.

For comparison, Matlab's onboard numerical "ODE45" solver was also used to calculate Aref's trajectories. This onboard solver is based on a 4th order Runge-Kutta approximation scheme that independently selects an appropriate dt. Its results are shown in Figure 4.6 with the ODE45 solver shown as the green line. The accuracy of prediction was comparable with

the DT method (Figure 4.4(d)) for a much shorter computational time. The accumulation of errors becomes apparent during the 3rd blink where the ODE45 solver has a much smaller trajectory around the left hand vortex. While the computational time is comparable to the DS method, the advantage of the latter is the ability to increase accuracy through decreasing grid spacing.

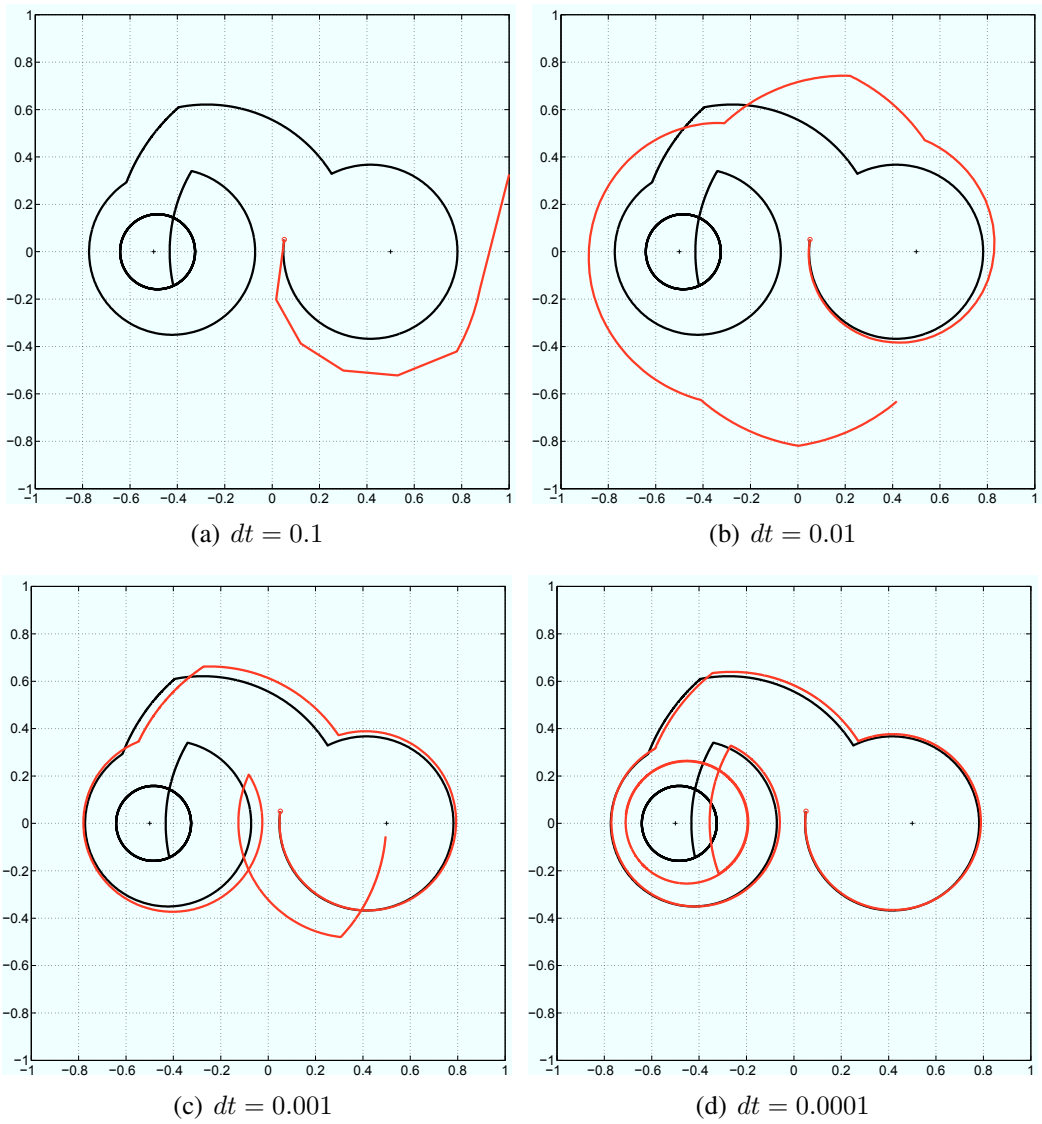

(a) $dt = 0.1$ (b) $dt = 0.01$

(c) $dt = 0.001$ (d) $dt = 0.0001$

Figure 4.4: Aref's blinking vortex and particle trajectories calculated using the DT model for four values of time step, dt. In all panels the black line is the analytically calculated trajectory and red is the DT model. A single particle is released at identical points within the grid $(0.05, 0.05)$. Vortices are centered at $(\pm 0.5, 0)$. Models were integrated for 3 "blinks" of the blinking vortex - that is, both vortices were on 3 times each. Each decrease in dt resulted in an increase of computational time such that the model ran for approximately $(a)30$ seconds,$(b)10$ min, $(c)30$ min, $(d)3$ hours. Note that when dt was decreased to 0.00001 (not shown) the model ran for 3 days with only a slight increase in accuracy from panel (d).

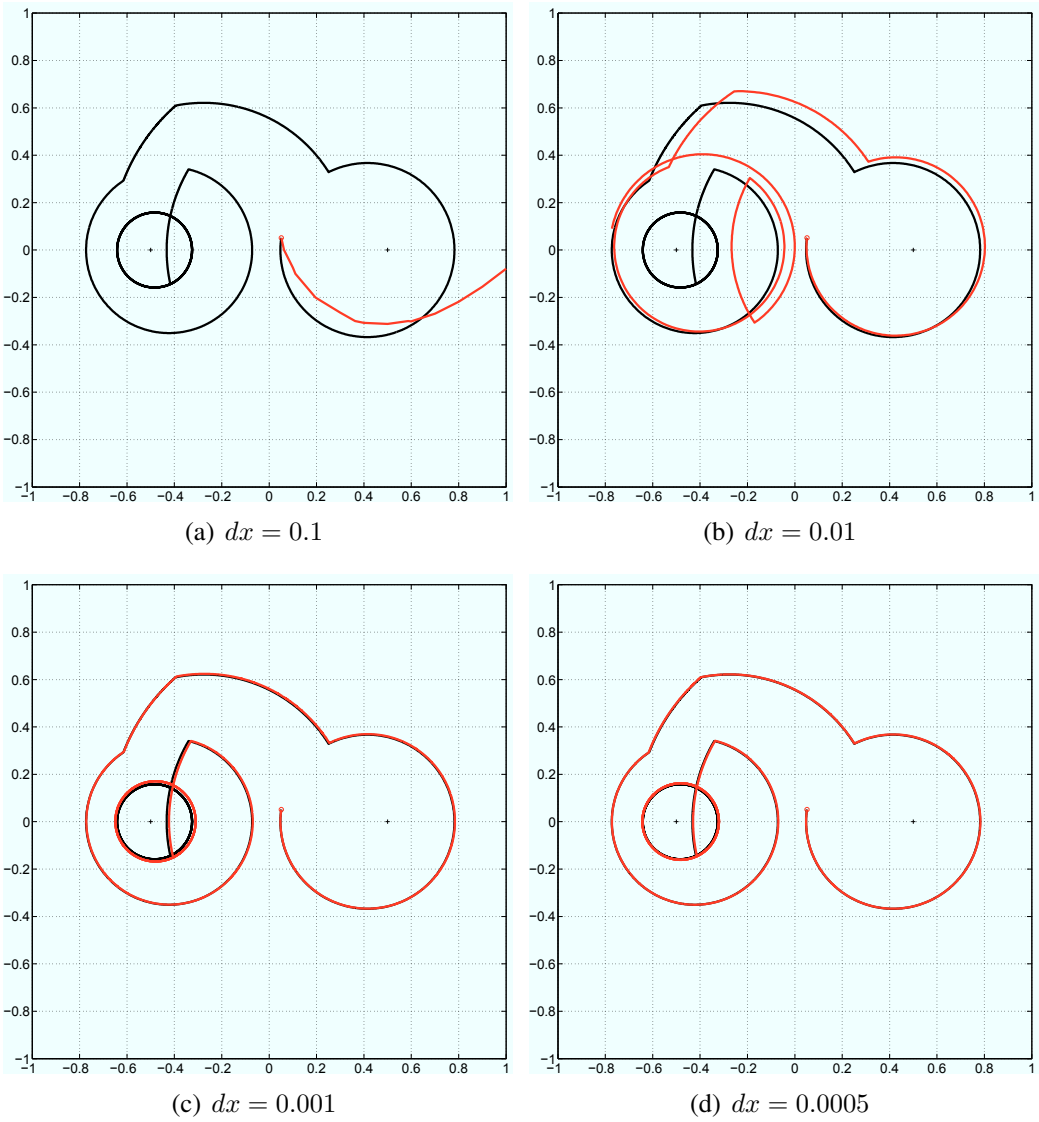

(a) $dx = 0.1$ (b) $dx = 0.01$

(c) $dx = 0.001$ (d) $dx = 0.0005$

Figure 4.5: Aref's blinking vortex and particle trajectories calculated using the DS model for four values of the size of the grid boxes, L. (Note the dotted grid shown in each panel does not reflect the different values of L.) Otherwise same format as previous figure. Computational time was approximately: $(a)30$ seconds,$(b)5$ min, $(c)10$ min, $(d)20$ min.

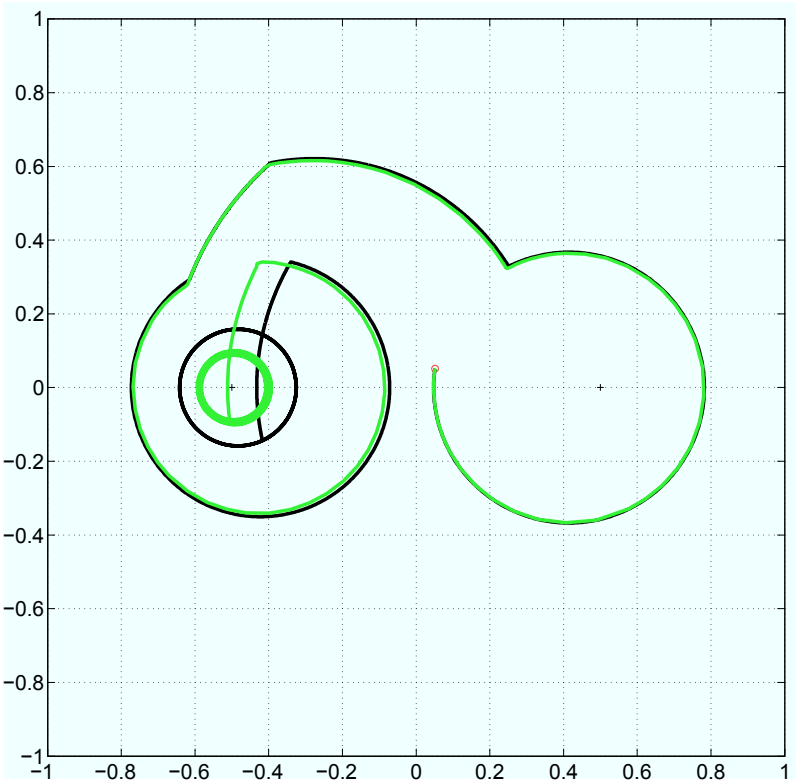

Figure 4.6: Trajectory calculated using Matlab's onboard Runge-Kutta method ("ODE45"). This method selects its own dt. The black line is the analytically calculated trajectory and green is the ODE45 model. A single particle is released at identical points within the grid at $(0.05,\ 0.05)$. Same format as previous two figures. Computational time was approximately 3 min.

To check on the longterm behaviour of the DS method, trajectories similar to those shown in Figure 2.2 were calculated for $t = T, 2T, 3T \ldots$. It is encouraging to note the DS method's calculations result in the same sort of behaviour including Lagrangian chaos originally identified by *Aref* (1983). This is demonstrated in Figure 4.7 where the positions of $40,200$ particles is shown after four blinks of the vortices ($t = 4T$). Particles were released in a 0.2 x 0.2 square as follows: ($-0.1 < x < 0.1$) and ($0.1 < y < 0.3$). Parameters regarding stirring protocol and location of the vortices are the same as in Figures 4.4, 4.5, and 4.6. Particles were colour coded by release point, varying in x, with blues released on the left ($x = -0.1$) and progressing to red on the right ($x = 0.1$).

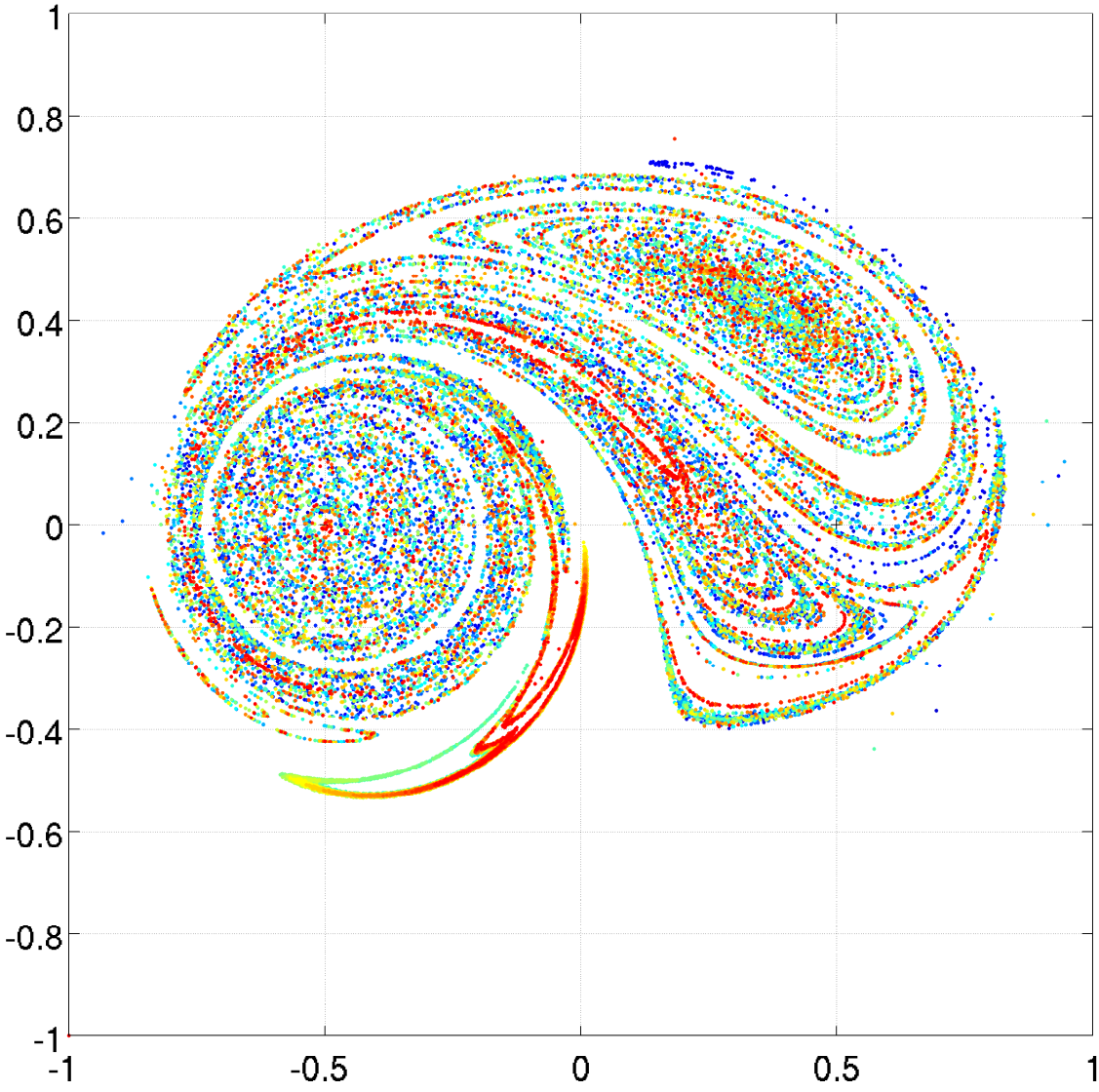

Figure 4.7: Lagrangian chaos calculated using the DS method after 4 blinks of the vortices ($t = 4T$). Approximately 40,000 particles were released in a 0.2x0.2 square from ($-0.1 < x < 0.1$) and ($0.1 < y < 0.3$). Particles were colour coded to release point, varying in x with blues starting at the left (x=-0.1) and reds on the right (x=0.1). Vortices are centered at $(\pm 0.5, 0)$.

4.3 False Aggregation of Particles

As discussed in Section 2.2, Visser demonstrated that the "naive" numerical implementation of the forward model can result in false aggregation of particles in areas of low diffusivity (*Visser*, 1997). This scenario is now examined using a naive DT and compared to the DS method with the dispersion extension described in the previous chapter. A 2D "bullseye" shaped diffusivity profile was created with the low diffusivity centered at position (50, 50) and with diffusivity increasing with distance from the center of the bullseye. Approximately 2500 particles were released in a 10x10 square centered in the top right corner at $(70, 70)$ and allowed to diffuse for 200 time units. Figures 4.8 and 4.9 show the results of the DT and DS particle tracking at the end of this time.

The DT method shows false aggregation at the center of the low diffusivity with a shift in the mean of the x and y positions from (70,70), the release point center, to (54,55) close to the position of minimum diffusivity. In comparison, the DS method shows diffusion and gradual homogenization from the point of release without aggregation in the vicinity of the minimum diffusivity. For both cases the boundaries of the model domain were reflective thereby ensuring that particles did not leave the domain. Figure 4.10 clearly shows how the mean and median of the x and y positions shift from the release region to the center of the low diffusivity if particle positions are calculated using the naive DT method. Figure 4.11 shows the DS model predicts an even diffusion away from the release region with no tendency to drift toward the position of minimum diffusivity, i.e., the mean and median are relatively stable around the release position despite the expanding final positions. Table 4.3 lists the means and medians of the particle ensembles for the two models with time.

If the DT method is integrated for longer, the time shift of the mean to the area of low diffusivity remains steady around 200-250. As expected, decreasing the gradient

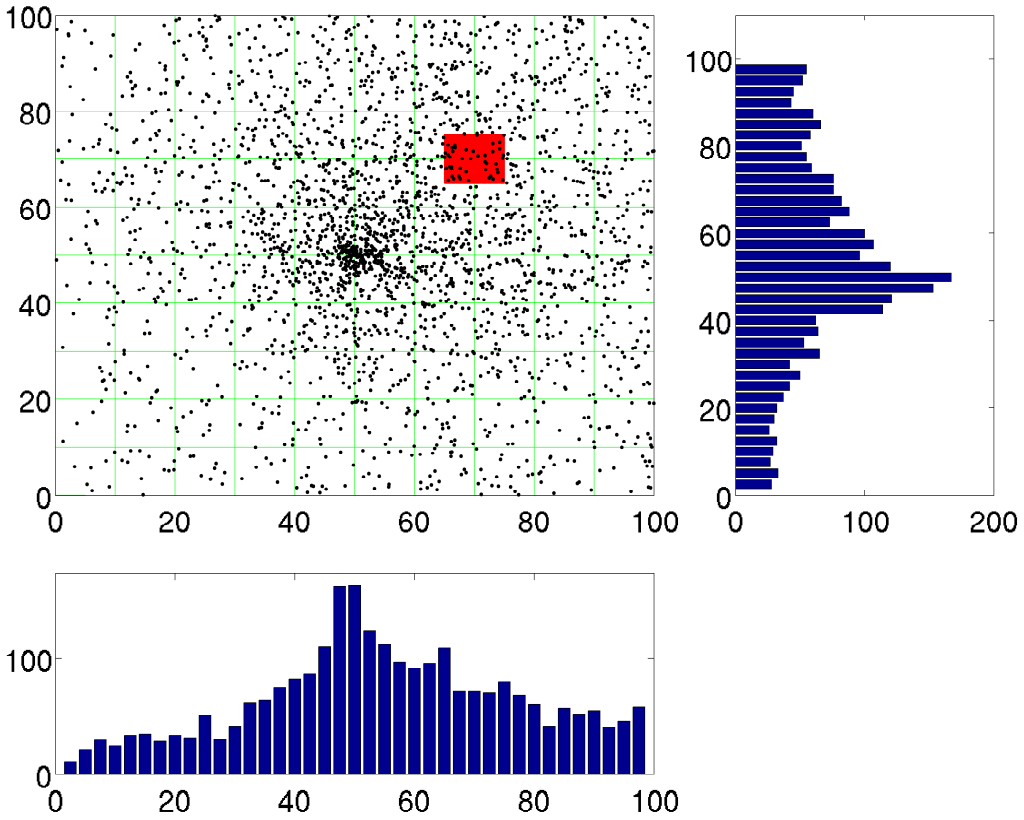

Figure 4.8: Final locations of approximately 2500 particles in a diffusive flow field calculated using a naive DT forward method for a duration of 200 [time units]. The particles were released in a box of width 10 centered on (70, 70) shown by the red square. The minimum in diffusivity is at (50, 50) and increases outwards as demonstrated in Figure 4.9.

of diffusion increases this time considerably. In the DS case, a slow homogenization of particles results in a drift of the mean towards the center. This is not a result of a false aggregation, rather it is because the center of low diffusivity was centered at (50,50). Figures for longer iterations are given in Appendix C.

In conclusion, the DS model outperforms the DT method for the idealized cases considered: the accuracy of the predictions was higher and, for large numbers of particles, the DS method is much faster. Decreasing the time step improves the accuracy of the DT approach but that comes at the cost of increased computation time. On the negative side the DS method can require a lot more memory for highly detailed flow fields.

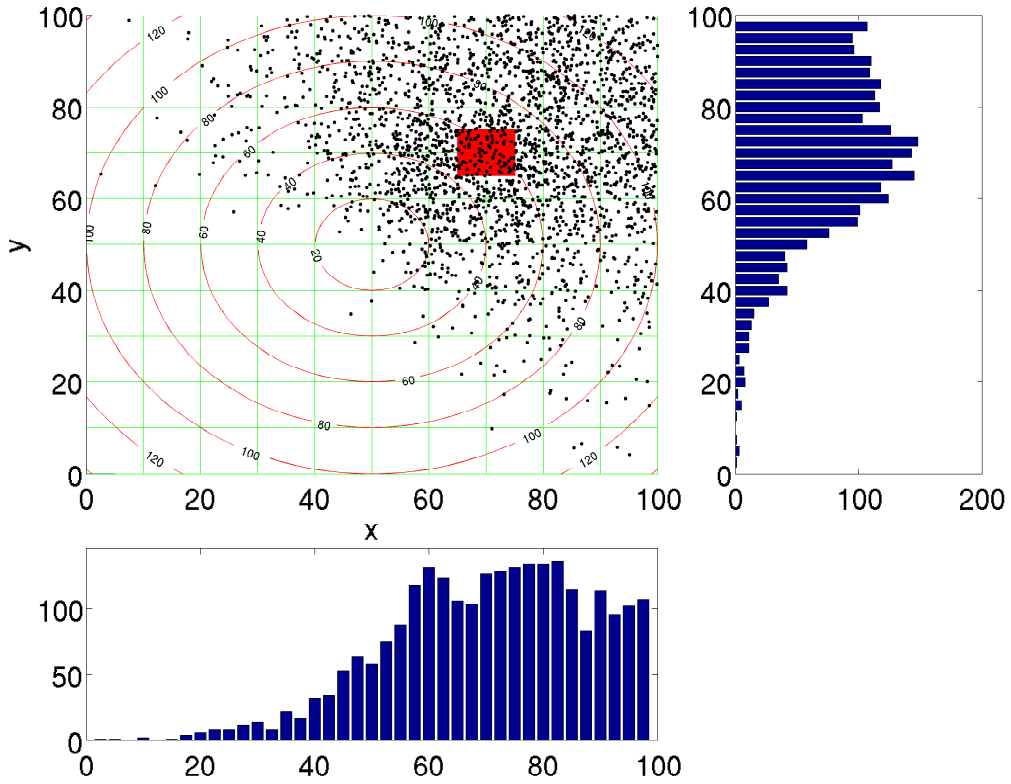

Figure 4.9: Final locations of particles in a diffusive flow field calculated using DS for a duration of 200 [time units]. The particles were released in a box of width 10 centered on (70, 70) shown by the red square. The minimum in diffusivity is at (50, 50) and increases outwards as indicated by the contour lines.

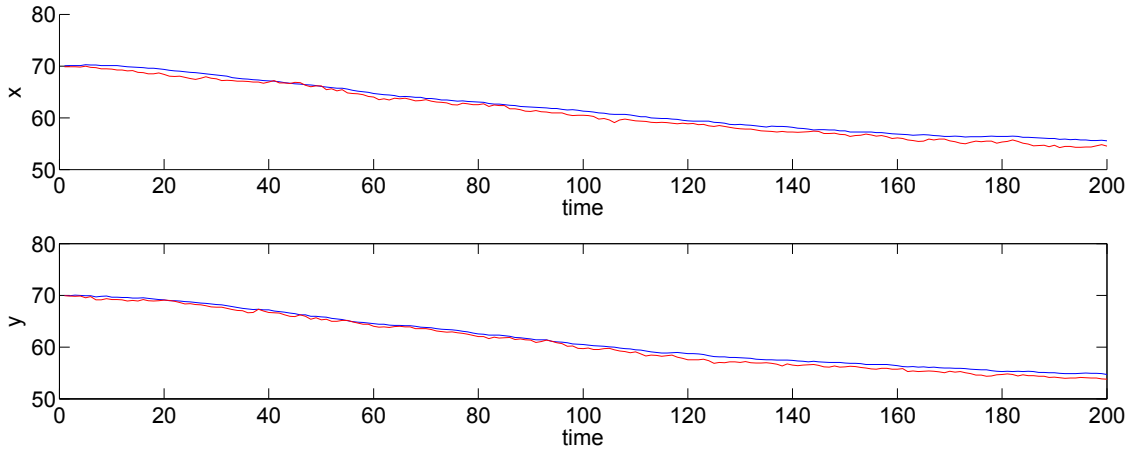

Figure 4.10: Time variation of the mean and median of x and y for changing particle positions using the naive DT model. The blue line is the mean and the red line is the median. The particles were released in a box centered on (70, 70) and the minimum in diffusivity is at (50, 50).

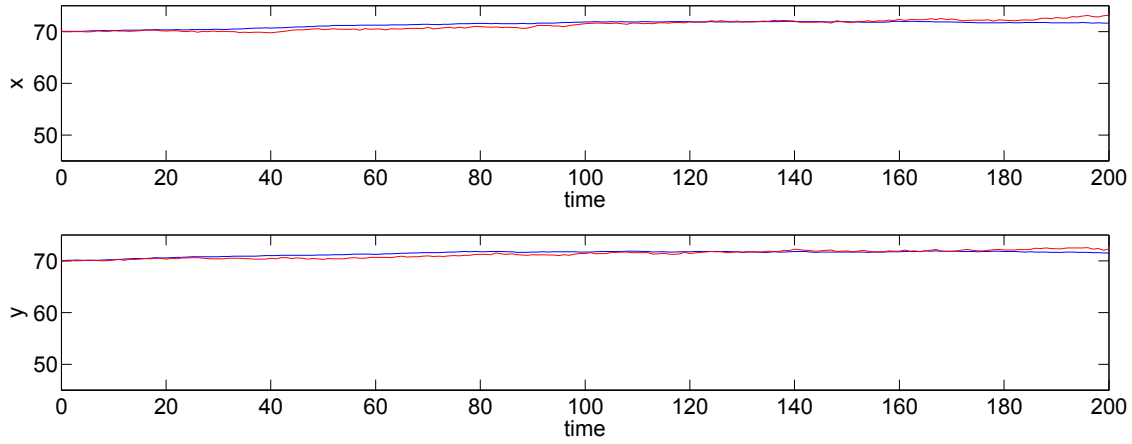

Figure 4.11: Time variation of the mean and median of x and y for changing particle positions using the DS model. The blue line is the mean and the red line is the median. The particles were released in a box centered on (70, 70) and the minimum in diffusivity is at (50, 50).

Duration	Discrete Time		Discrete Space	
	mean x [median x]	mean y [median y]	mean x [median x]	mean y [median y]
200	54.55 [56.68]	55.24 [54.13]	71.62 [73.14]	71.51 [72.30]
500	49.96 [50.32]	50.54 [50.41]	66.90 [70.52]	67.10 [70.55]
1000	50.19 [50.10]	50.65 [50.32]	61.22 [65.73]	60.59 [64.29]
3000	49.87 [49.78]	49.49 [49.49]	51.80 [51.48]	51.88 [52.57]

Table 4.1: False aggregation of particles. Long term time dependence of the mean and median of the x and y positions of an ensemble of particles calculated by the naive DT and the DS method. The particles were released in a box centered on (70, 70) and the minimum in diffusivity is at (50, 50).

CHAPTER 5

OBSERVATIONS AND MODELS OF THE SCOTIAN SHELF AND GULF OF MAINE

The Scotian Shelf is a roughly 700 km stretch of continental shelf off the coast of Nova Scotia, Canada (e.g., *Uchupi*, 1968). It is bounded by the Laurentian Channel to the north-east, and by the Northeast Channel and the Gulf of Maine to the south-west. It is relatively wide and shallow, varying in width from 120 to 240 km with an average depth of 90 m (*MacLean et al.*, 2011). The topography is fairly complicated with deep basins and channels separated by shallow offshore banks. To the southwest, the Gulf of Maine is a semi-enclosed $90,700$ km^2 inland sea with an average depth of 150 m (e.g., *Uchupi*, 1968). It is bounded by the northeastern American states of Maine, New Hampshire, Massachusetts and the Canadian provinces of Nova Scotia and New Brunswick. Similar to the Scotian Shelf, the Gulf of Maine has numerous deep basins and shallow banks. The largest bank, Georges Bank, is capped on its northeast edge by the Northeast Channel and to the southwest by the Great South Channel. These two channels are the primary inflow and outflow channels of the marine waters to the Gulf (e.g., *Thompson*, 2010).

The Scotian Shelf and Gulf of Maine are of interest for several reasons. The regional circulation has a major impact on commercial fishing (e.g., *Hannah et al.*, 2001). In addition, many aquaculture sites are located in the region and there has been an increase in the number of hydrocarbon exploration sites, as well as other energy producing plants, in

recent years (*MacLean et al.*, 2011; *Thompson*, 2010). The numerous ports of the region reflect extensive marine activities related to commercial shipping, coastal tourism and Maritime Defence applications (*MacLean et al.*, 2011; *Thompson*, 2010).

5.1 Overview of the Regional Circulation

Three currents strongly influence circulation on the Scotian Shelf: the Labrador Current, the Nova Scotia Current, and the Gulf Stream (e.g., *MacLean et al.*, 2011). The effects of these currents vary seasonally. In general the flow is from the northeast to the southwest paralleling the Nova Scotia coast (e.g., *MacLean et al.*, 2011; *Hebert et al.*, 2013). As shown in Figure 5.1, the Labrador Current bifurcates at the tail of the Grand Banks of Newfoundland with a portion flowing to the east, inshore of the North Atlantic Current (*Fratantoni and Pickart*, 2007). This "shelfbreak" current continues equatorward along the edge of the Scotian Shelf and is known as the shelfbreak jet (*Fratantoni and Pickart*, 2007). The effect of the Labrador Current is felt more strongly in the northern section of the Scotian Shelf. Relatively cool, fresh water flowing from the Gulf of St. Lawrence divides at the northern tip of Nova Scotia, with a portion flowing down the Atlantic coast as the Nova Scotia Current. The remainder follows the Laurentian Channel to the shelf break where it joins with the cold, fresh southbound Labrador current to flow down the shelf edge (*MacLean et al.*, 2011). Warm salty water from the Gulf Stream flowing northward mixes with the cooler fresher water over the shelf and form the Slope Water jet which periodically leaks onto the shelf via channels at the shelf break (*MacLean et al.*, 2011).

Hannah et al. (2001) review what is known of the regional circulation including the larger, well known flow features and the partial gyres around Browns Bank and Sable Island Bank. With regard to ocean circulation models, (*Hannah et al.*, 2001) state

> "a large number of field and model studies have contributed to our understanding of the circulation on the western/central Scotian Shelf ... [the

studies] fall far short of providing the spatial coverage required for Lagrangian circulation evaluations."

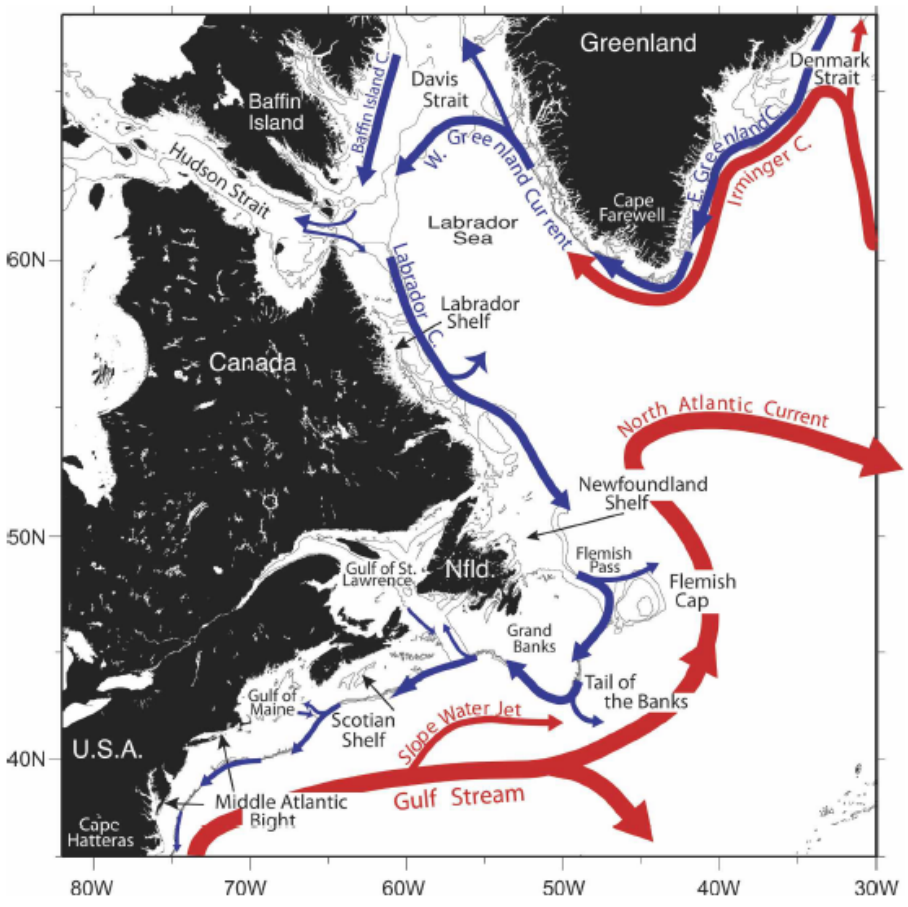

Figure 5.1: Large scale view of the regional circulation off the East Coast of Canada to explain Scotian Shelf circulation, including major influencing currents. The path of the shelf break jet is designated by blue arrows while the warmer, Gulf Stream origin currents are drawn in red. From *Fratantoni and Pickart* (2007)

The circulation of the Gulf of Maine follows a seasonal cycle that is generally opposite to that of the Scotian Shelf with the strongest currents in summer and weak to almost non-existent in winter (*Thompson*, 2010). As demonstrated in Figure 5.2, cold water enters the gulf via the Nova Scotia current and the Northeast Channel, and then turns north to enter the Bay of Fundy (*Thompson*, 2010). The current is then deflected southwestward and forms the Gulf of Maine Gyre. Tidal fluctuations and shallow water over Georges

Bank form a secondary, clockwise-spinning gyre *Thompson* (2010). The water can then leave the gulf through the Northeast Channel, the Great South Channel or over the eastern portion of Georges Bank.

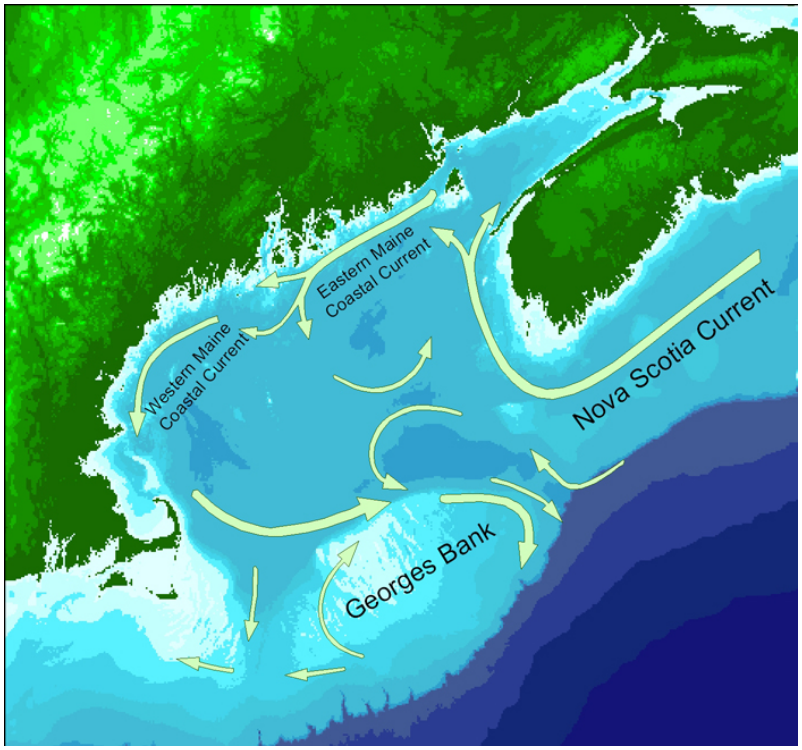

Figure 5.2: Currents off the Scotian Shelf and in the Gulf of Maine. From http://www.gulfofmaine-census.org/about-the-gulf/oceanography/circulation/

5.2 Regional Model of the Scotian Shelf and Gulf of Maine

The flow fields used in this thesis were generated by Anna Katavouta as part of a downscaling study from global to regional scales. (Anna Katavouta is a graduate student in the final stages of her PhD programme at Dalhousie University.) The global fields were generated by the HYCOM/NCODA system. The 3D, time varying current fields used in the present study were generated by a regional model that is one-way nested to the global HYCOM system. The regional model was developed by Anna Katavouta based on the Nucleus for European Modelling of the Ocean (NEMO version 3.1) framework.

The domain of the regional model is shown in Figure 5.3. The model has a horizontal resolution of 1/36°and 52 vertical levels with a spacing that varies from 0.7 m at the surface to 233 m for the deepest level.

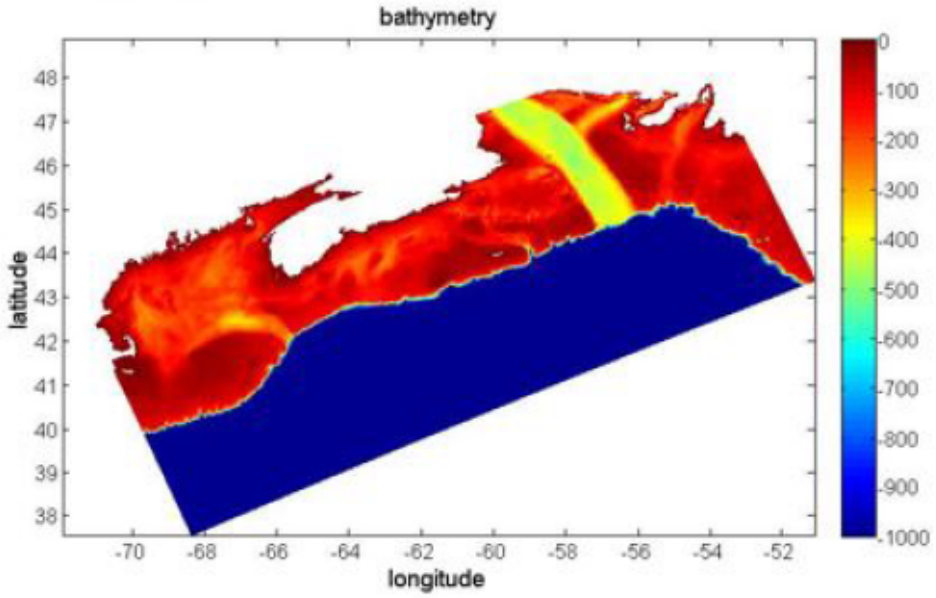

Figure 5.3: Domain of the regional ocean model and the large scale bathymetric features. Red indicates shallower water and blue indicates deeper areas. Kindly provided by Anna Katavouta.

The regional model is forced at the surface by six atmospheric variables: precipitation, wind, temperature, humidity, and longwave and incoming shortwave radiation. Five tidal constituents (M2, S2, N2, K1, O1) were used to define the tidal component of the lateral boundary conditions. The nontidal component of the lateral boundary conditions was interpolated from the global HYCOM output. A more detailed explanation of the regional model is provided in the PhD thesis of Anna Katavouta. Based on extensive comparisons of model output and observations, Katavouta has shown that the model can simulate many of the observed circulation features discussed in Section 5.1 including tidal heights, tidal currents, tidal residual circulation, sea level, storm surges, temperature, salinity, and currents (*Katavouta et al.*, 2015). In general the model performs very well on the Scotian

Shelf and in the Gulf of Maine region and in particular in areas where the interaction of strong tidal currents with local bathymetry is important, e.g., Georges Bank, Browns Bank, Sable Island (*Katavouta et al.*, 2015). It does not perform as well in the adjacent deep water as it is not able to accurately predict the timing and location of eddies and meanders (*Katavouta et al.*, 2015). However, this issue is being resolved through downscaling methodologies.

5.3 Deep Basins of the Scotian Shelf

The hypsometric curve is a useful way of summarizing the mean depth of a region. It shows the proportion of land area that exists at various elevations. For the Scotian Shelf it has been used (Figure 5.4) to show the proportion of the shelf at depths above a given level.

Another way of visually summarizing the bathymetry is to picture the Scotian Shelf draining away in the same way as a bathtub. At the surface, there is only one large basin. As the water drains, the shelf floor begins to be revealed, and the shelf divides into separate basins. This visualization is demonstrated in Figure 5.5. Specifically, in Figure 5.5(b) 100 m of water has been drained. The area that would now be dry is shown in red, and the area that would be water covered is shown in blue. In this way it can be seen that at a depth of 170 m there are several distinct basins while at 120-150 m many of these basins are connected. It is straightforward to summarize the number of distinct (unconnected) basins by simply counting them for different draining depths. This new type of visualization complements the hypsometric curve and is demonstrated in Figure 5.6. The right hand side of Figure 5.6 shows the average size of basins as a function of depth. Figure 5.6 is used later to help define the deep basins and their interconnections.

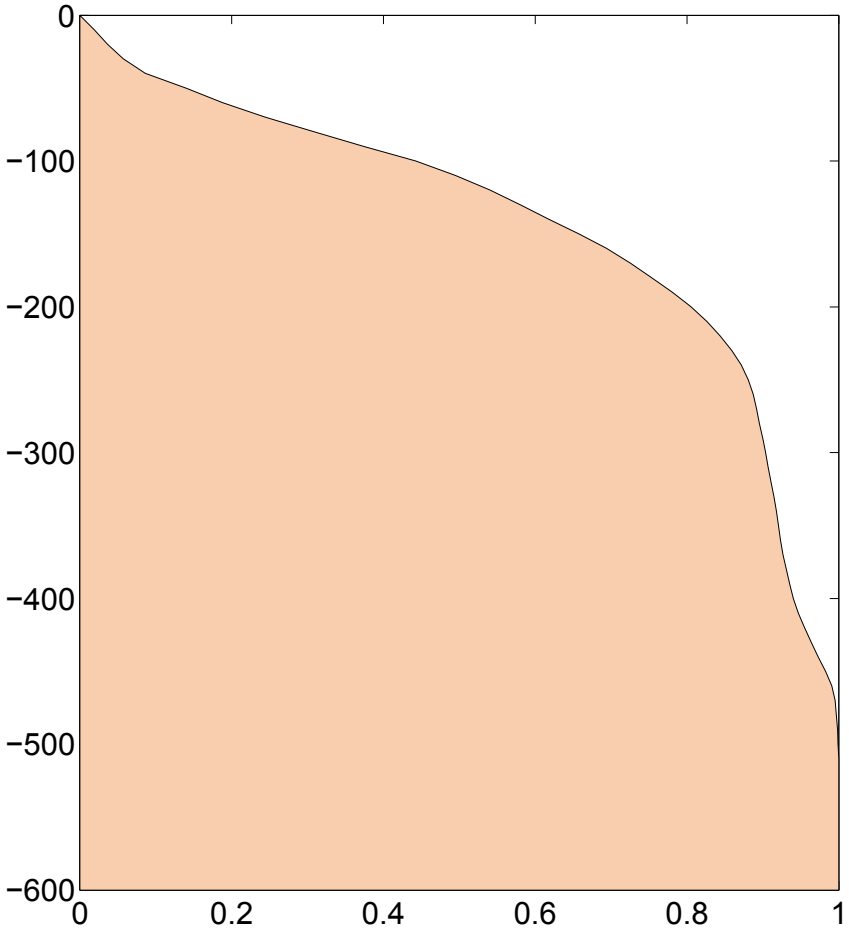

Figure 5.4: Hypsometric curve for the Scotian Shelf. Depth is on the y-axis in [m] and the relative proportion of dry area on the x-axis. As water is "drained" away from the Scotian Shelf the relative proportion of dry land area to wet land area increases.

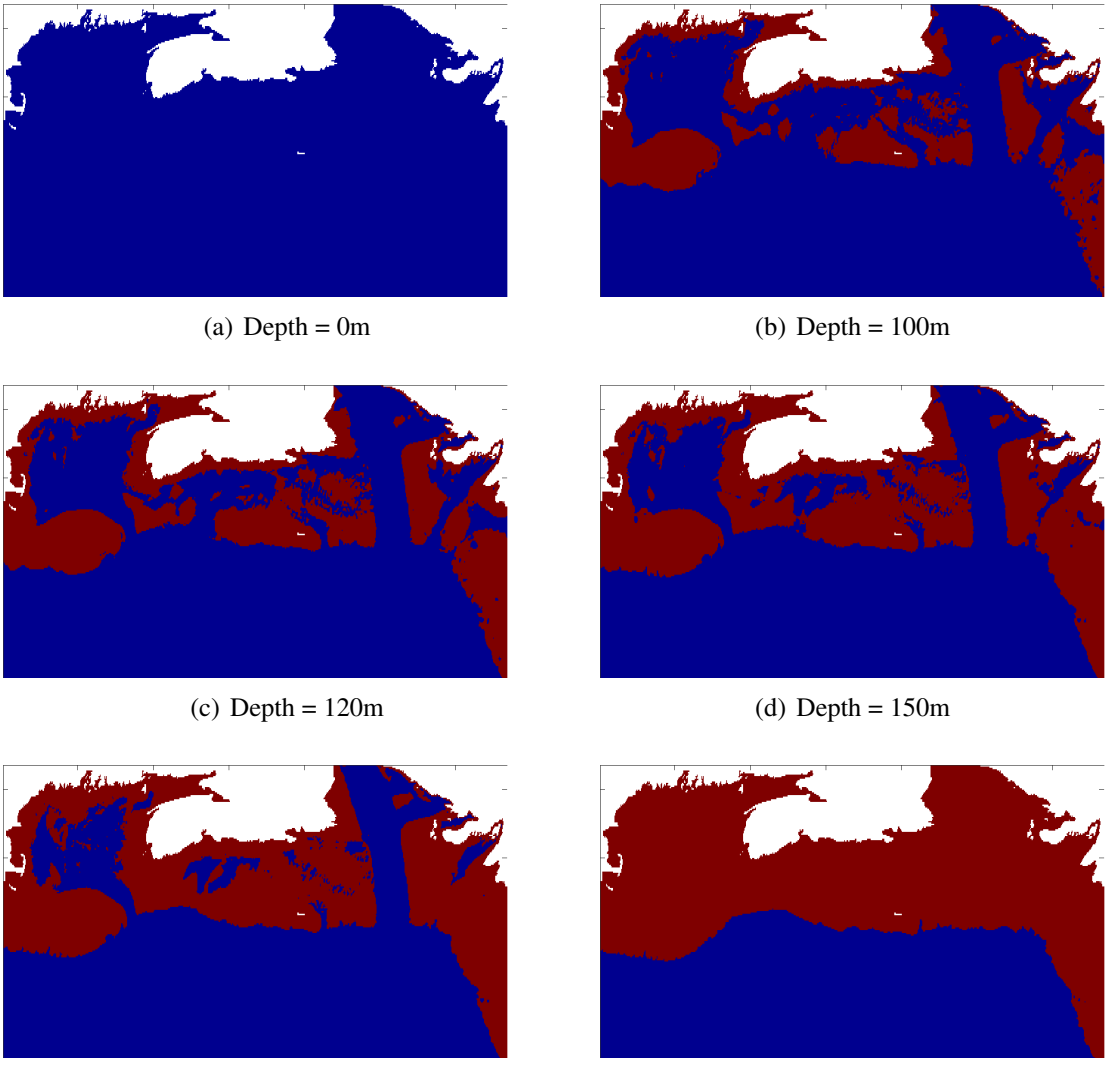

(a) Depth = 0m

(b) Depth = 100m

(c) Depth = 120m

(d) Depth = 150m

(e) Depth = 170m

(f) Depth = 510m

Figure 5.5: Effect of "draining" the Scotian Shelf on the number of distinct deep ocean basins. Red indicates bottom topography that would be dry if the water level on the Scotian Shelf dropped by: (a)0 m (b)100 m (c)120 m (d)150 m (e)170 m (f)200 m. Blue shows regions that would still have water.

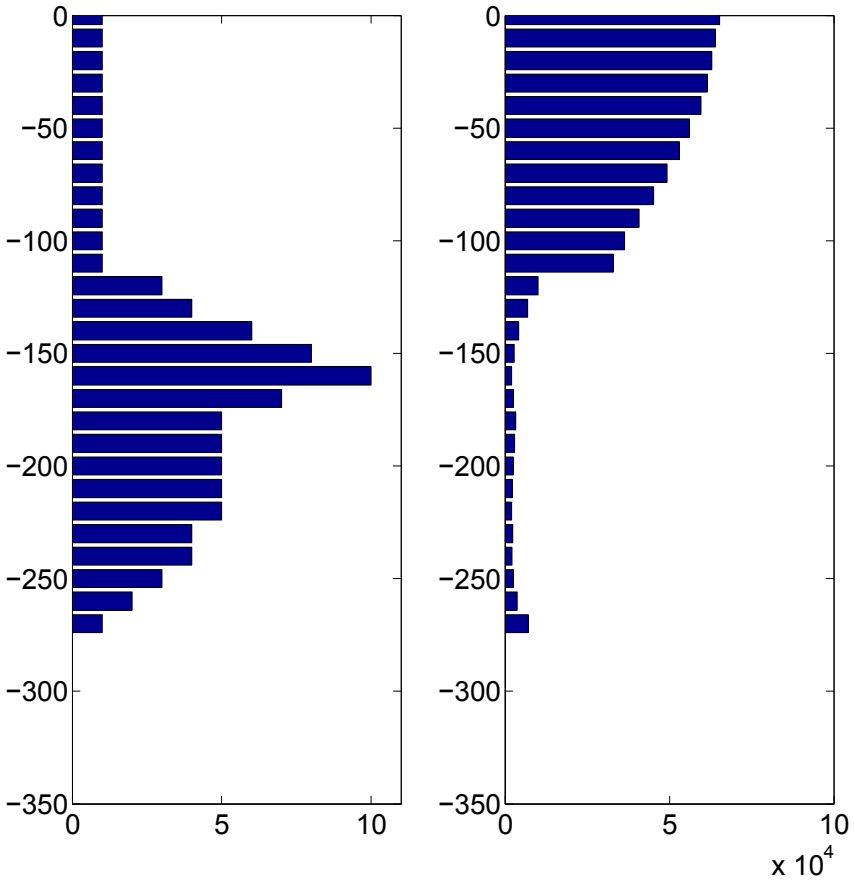

Figure 5.6: The number of basins, and the average size, on the Scotian Shelf by depth. Left hand panel shows the number of basins by depth. The right hand panel shows the average size of the basins, measured in terms of the number of grid boxes within each basin. Each grid box has an area of approximately 6 km^2.

CHAPTER 6

RETENTION AND CONNECTIVITY OF DEEP BASINS ON THE SCOTIAN SHELF

A large amount of information can be contained within a single Eulerian flow field predicted by an ocean model. Consider the flow fields generated by the regional model described in Chapter 5; the number of gridded current velocities, for the whole domain at all depths and time steps, is on the order of 10^9. In this chapter it will be shown how Lagrangian based methods can be used to better visualize this vast amount of information with a particular focus on the deep basins of the Scotian Shelf and their connections with the adjacent North Atlantic. The Lagrangian approach provides answers to a number of important questions: How long do particles remain in a given basin? How do particles travel between basins and the shelf break? Where are the connections? Images such as Figure 6.1 give an idea of where to start looking for the answers. In this figure, particles were released along the 200 m isobath of the shelf break on January 1 st, 2010 and allowed to drift in daily changing flow fields for 90 days. If seasonal variations in this pattern are of concern, similar displays for different seasons can readily be created (Figure 6.2). The effect of changing from daily changing flow fields to hourly can help address how important is it to include tides in trajectory calculations (Figure 6.3)? It is shown below that new insights, which complement those developed in an Eulerian frame, are revealed through the use of Lagrangian displays of the flow fields on the Scotian Shelf.

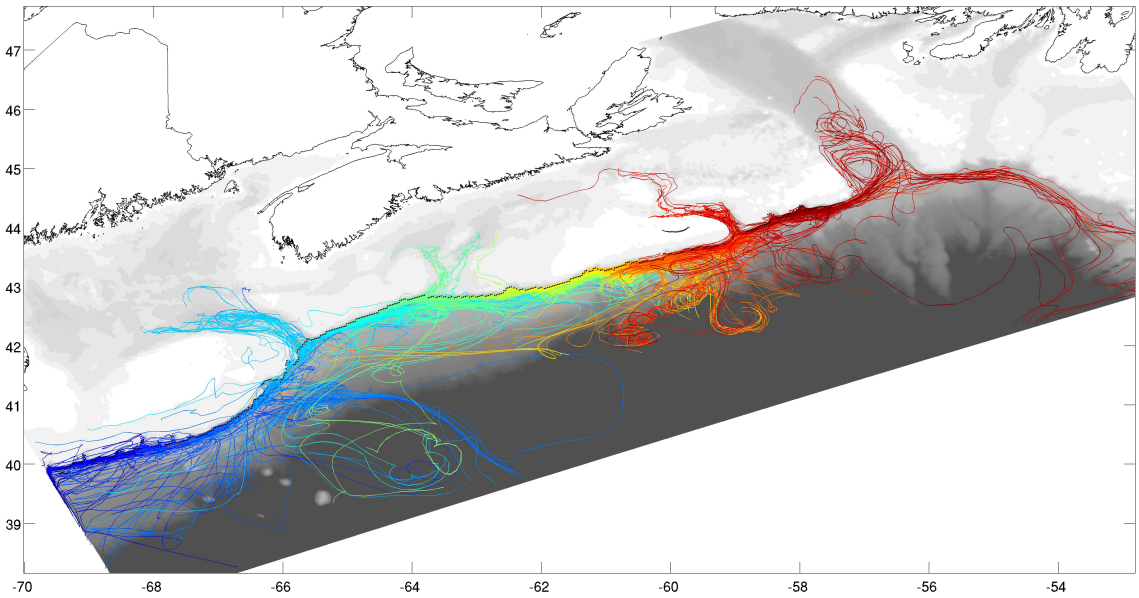

Figure 6.1: Trajectories of particles released along the shelf break in winter. Particles were released at 200 m and allowed to travel for 90 days in *daily* changing flow fields. Particles were released on January 1st, 2010. The color indicates release location (blue to the southwest, red to the northeast).

Particle tracking can be used to identify source regions for objects although, as discussed in Chapter 2, simply reversing the flow fields is not justifiable if the flow field is nondivergent and the diffusivity varies in space. It is possible however to find source regions using a forward integration method but with a backward perspective. This eliminates the complications of reversing the flow field. This method is typically iterative and lends itself well to probabilistic descriptions as described in Chapter 3 (*Breivik et al.*, 2012; *Isobe et al.*, 2009). To illustrate, consider a large-scale particle release with at least one particle released within every grid box throughout the regional model's domain. As each particle drifts for a set period of time, the trajectories can be selected according to a given condition. For example, one could chose only particles that are within a given basin on the first day of the release, or select only those trajectories than end up in a given basin at some later time. This way of selecting trajectories leads to estimates of conditional probabilities of particle position at a given time, t, given where they were at some other location at time t_c. The question of where will they go corresponds to conditioning on $t_c < t$ and the question

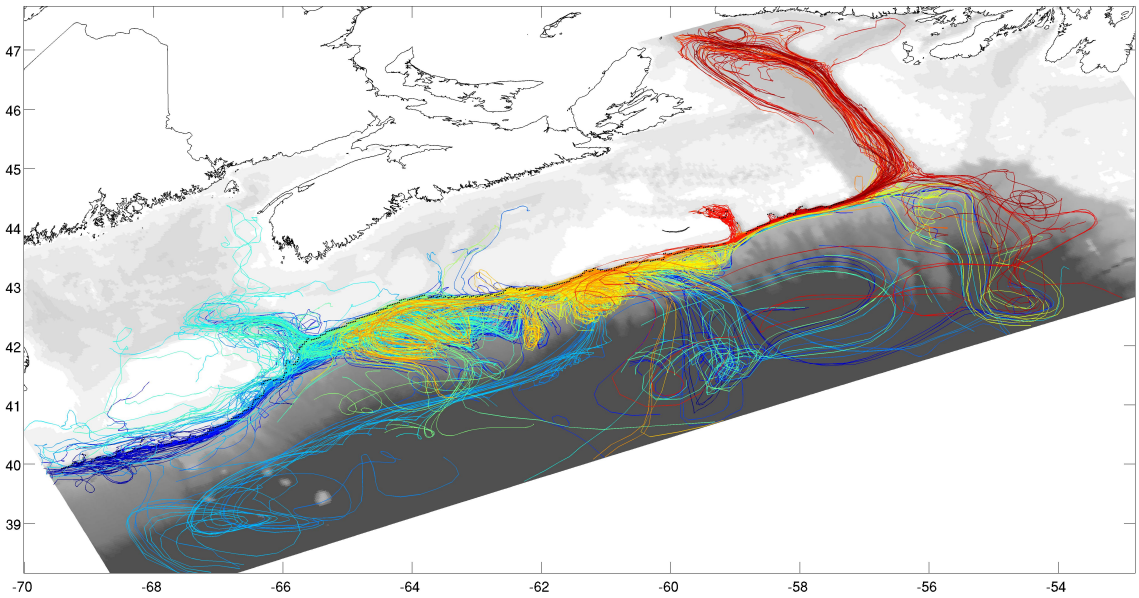

Figure 6.2: Trajectories of particles initiated along the shelf break in summer. Same details and format as previous figure but for a release date of July 1st, 2010.

of where they come from corresponds to conditioning on $t_c > t$. This method of selective trajectory comparison can also be used to reveal basin retention times as a function of depth and season. Particles that use particular channels, or cross certain sills, can also be selected to reveal critical features of the circulation and exchange.

When looking at figures such as Figures 6.1, 6.2 and 6.3, the connections between basins, and between basins and the shelf break, became readily apparent. Emerald and Lahave Basin (Figure 6.4) are now selected for further study. Figure 5.5 shows that Emerald Basin is the deepest: its maximum depth is about 275 m while Lahave Basin's is about 245 m. These two basins are connected in two places at a depth between 160 and 170 m. A sill connects the basins to the shelf break. This sill connects with Lahave Basin at around 145 m and with Emerald Basin at around 135 m (Figure 6.4).

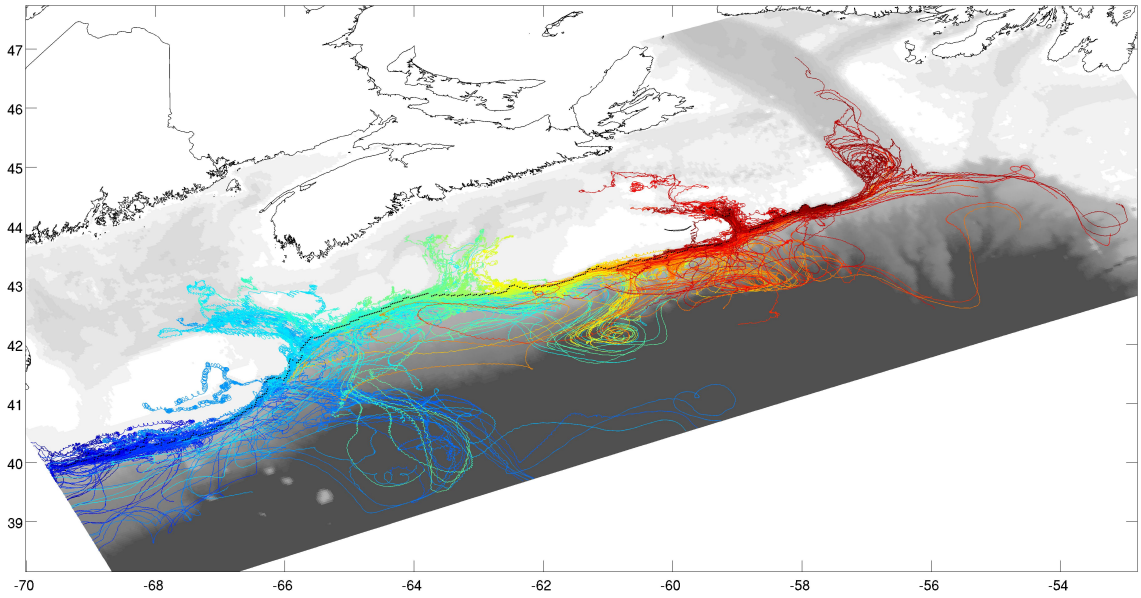

(a) Winter

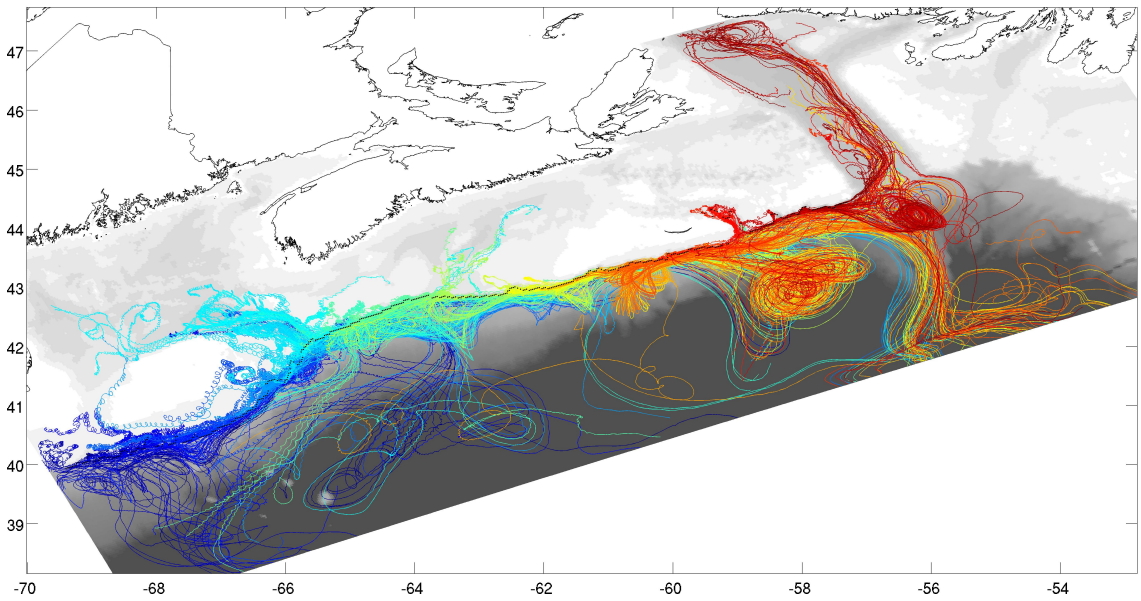

(b) Summer

Figure 6.3: Trajectories of particles released along the shelf break in winter and summer. Same details and format as Figures 6.1 and 6.2 except that the flow fields were defined *hourly* and thus include the effect of tides.

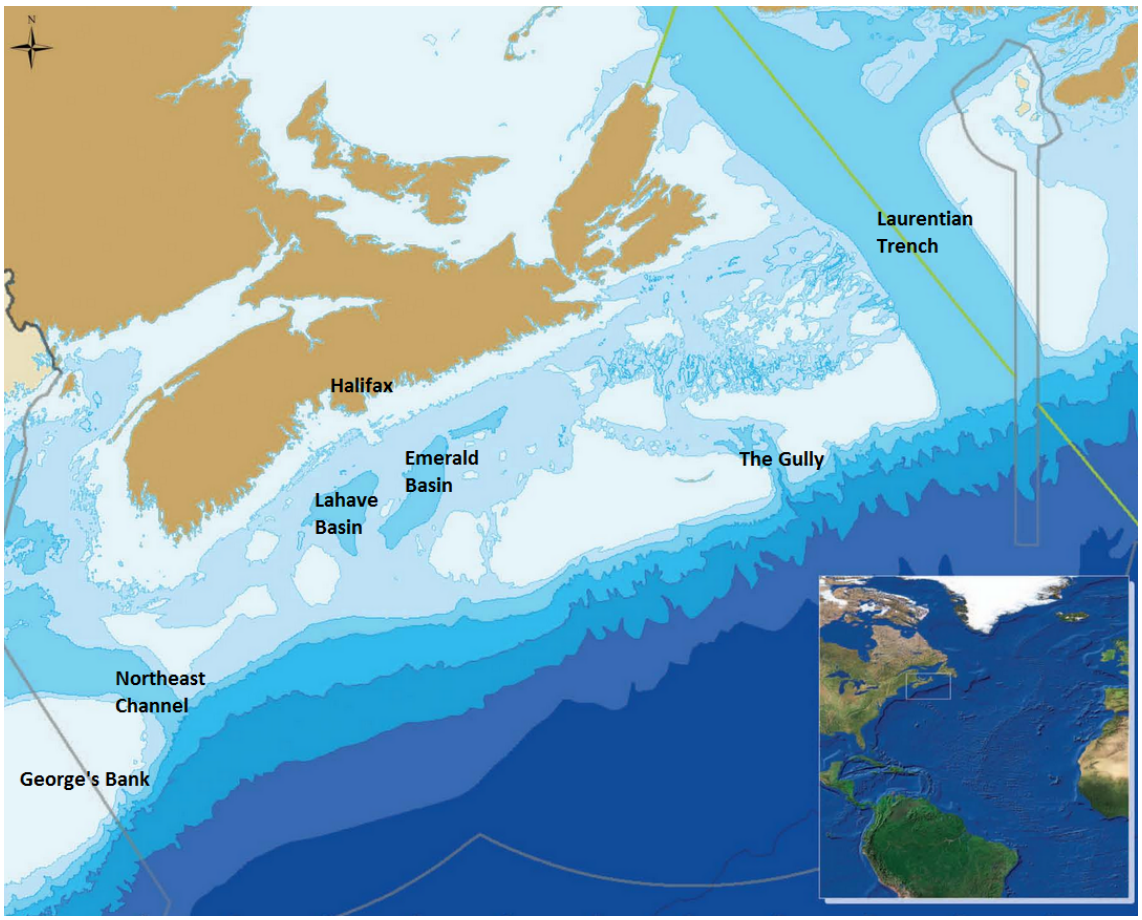

Figure 6.4: The main features of the Scotian Shelf including the location of Georges Bank, Emerald and Lahave Basin, and the Laurentian Trench. From $http://www.inter.dfo-mpo.gc.ca/folios/00252/images/lg_img004.jpg$.

6.1 Retention within Deep Basins

Retention can be thought of as the tendency for a water parcel, tracer or biological organism to remain within a specific region, such as a deep basin, for a set period of time. Retention can be quantified using many different methods including transition matrices or transport tables (*Thompson et al.*, 2002). Probability intensity plots are a straightforward and intuitive way of visualizing retention. A probability intensity plot is created by adding a colour code to a 2 dimensional histogram superimposed over the regional bathymetry. This can convey the outcome of many particle trajectories simply, as opposed to a "spaghetti" trajectory plot which becomes complicated quickly.

A full domain release for all depth levels as described above was performed using daily changing flow fields from the regional model for the years $2010, 2011, 2012$. Particles were released on the first day of the winter and summer seasons (January and July 1st respectively) and allowed to drift for 90 days. For simplicity, the release date will be referred to as day 1 and the respective season end as day 90. In Figures 6.5 and 6.6, the left panels show the sources (particles' starting location on day 1) given that the particle ended up below 100 m in the given basin on day 90. The right hand panels show destinations of particles (final positions on day 90) for every particle that started below 100 m, in the given basin on day 1. The "minimum depth" of 100 m was selected for particle exclusion because above this depth, all basins are connected as shown in Figures 5.5 and 5.6.

The particle density plots shown in Figures 6.5 and 6.6 were generated using daily snapshots of the regional model's flow fields. (After these density plots were calculated and interpreted, it was realized that daily snapshots were less than ideal because in some locations unrealistically large vertical velocities were generated. To overcome this aliasing problem, and also to accurately describe the Stokes drift associated with diurnal and semi-diurnal tidal motions, an additional set of runs using hourly flow fields was performed.

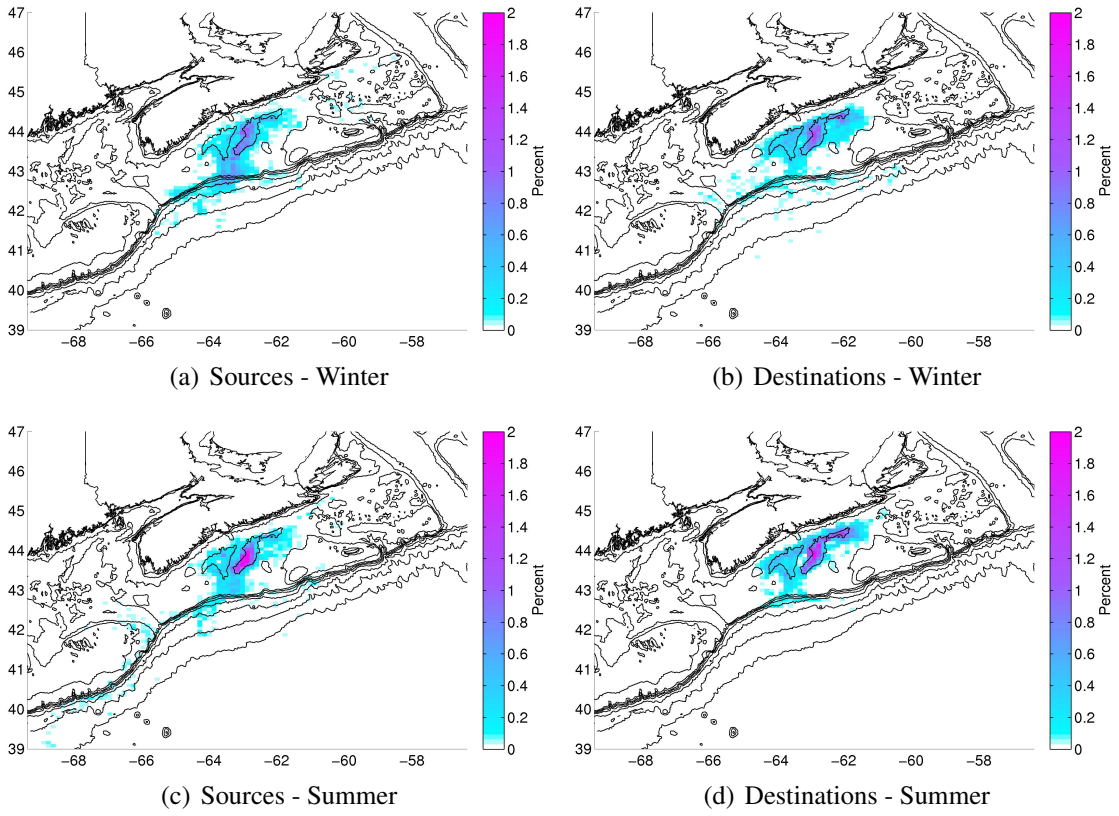

(a) Sources - Winter

(b) Destinations - Winter

(c) Sources - Summer

(d) Destinations - Summer

Figure 6.5: Emerald Basin particle density after 90 days for 2010 to 2012. Left hand panels show sources for Emerald Basin (where the particles come from). Right hand panel shows the final locations of particles that started in Emerald Basin (where the particles go). The advecting flow fields were daily snapshots as discussed in Chapter 5. The dispersion was set to zero. Particles were released at all depth levels over the entire domain and selectively screened. Particles within the basin polygon above 100 m were discounted from these results.

This led to an assessment of the effect of different flow field time spacings on the density plots.) Using higher frequency flow fields such as hourly, can reduce the error in position, particularly those affected by large vertical tidal velocities that are aliased by the daily snapshots. Figures 6.7 and 6.8 show intensity plots calculated using hourly flow fields. As before, particles were initiated in a full domain run. Hourly flow fields were available for the winter and summer of 2010 only. Again, particles were released on January and July 1st respectively and allowed to drift for 90 days.

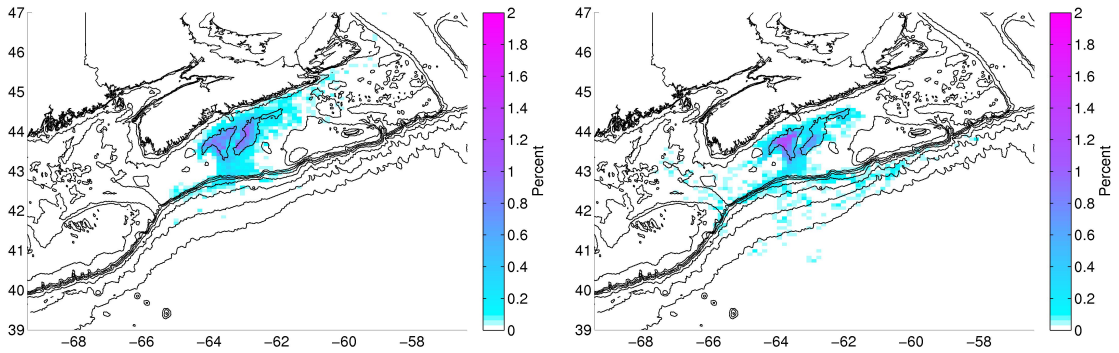

(a) Sources - Winter

(b) Destinations - Winter

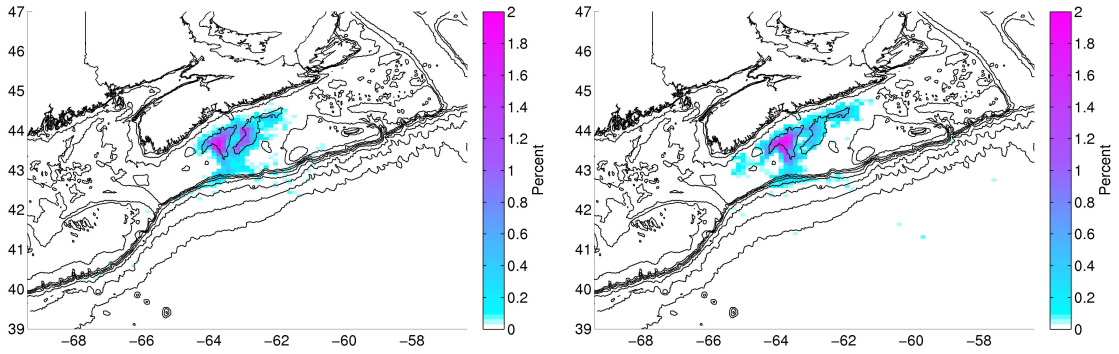

(c) Sources - Summer

(d) Destinations - Summer

Figure 6.6: Lahave Basin particle density after 90 days for 2010 to 2012. Otherwise same as Figure 6.5.

The particle densities shown in Figures 6.5 to 6.8 indicate retention patterns by basin and season. Locations where a higher percentage of particles originate, or end up, are indicated by purple "hotspots." The large scale features of the intensity plots calcuated using hourly and daily flow fields are similar with hotspots typically located within the source basin. Therefore, if one is interested in the large scale it is not necessary to include the tides when generating particle density plots such as those shown in Figures 6.5 to 6.8. However, the detailed features of the intensity plots depend on the tides.

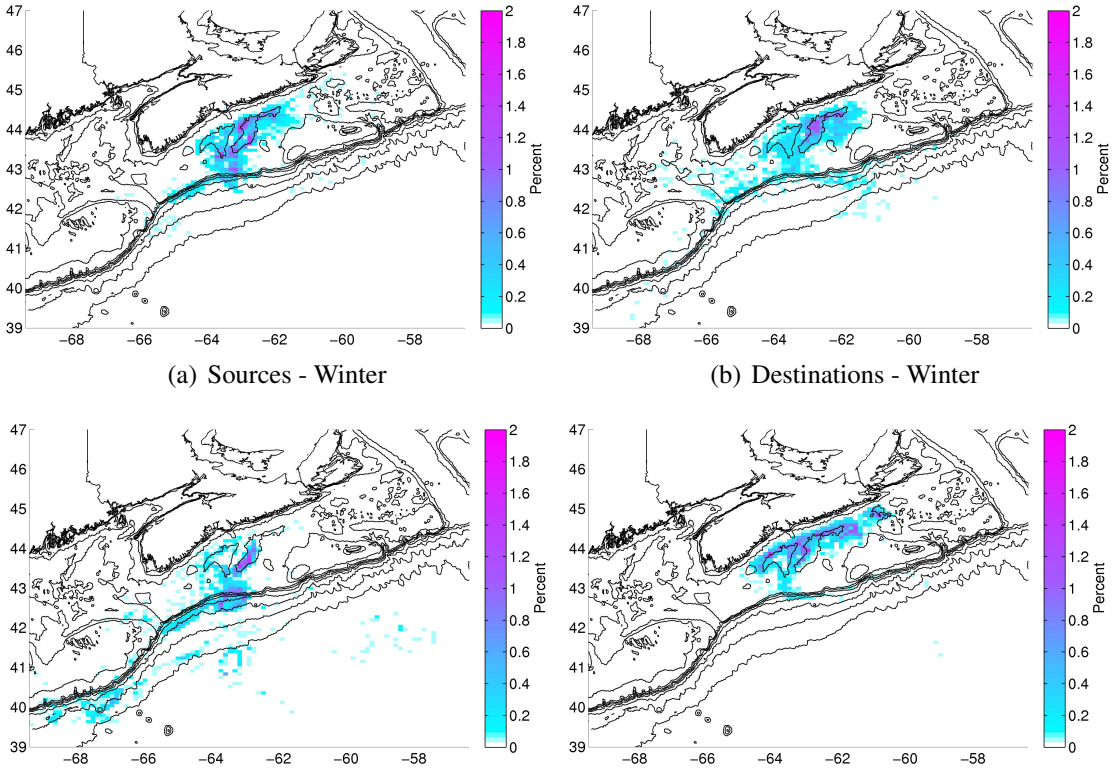

(a) Sources - Winter

(b) Destinations - Winter

(c) Sources - Summer

(d) Destinations - Summer

Figure 6.7: Emerald Basin particle density based on *hourly* flow fields for 2010. Otherwise same as Figure 6.5.

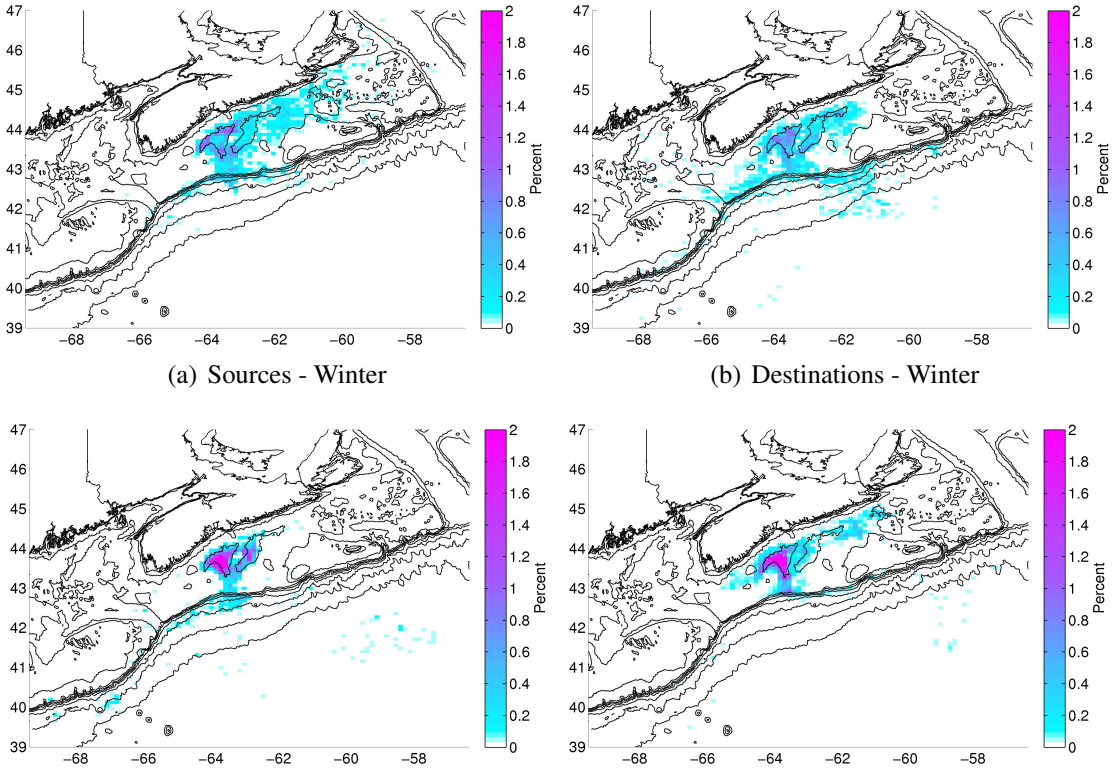

(a) Sources - Winter

(b) Destinations - Winter

(c) Sources - Summer

(d) Destinations - Summer

Figure 6.8: Lahave Basin particle density based on *hourly* flow fields for 2010. Otherwise same as Figure 6.5.

To quantify retention for a specific basin, the number of particles remaining in the basin, below a given depth, was monitored as a function of time. It was found that, in general, the proportion declined exponentially with time toward a value that was effectively constant. This lead to the definition of two indices to quantify retention for a given basin: an e-folding time that describes the initial loss of particles, (e.g., *Emerson and Hedges*, 2008), and a constant value indicating the proportion retained on longer time scales.

More specifically, a large ensemble of particles was released in the given basin , once a day for the first month of the season of interest. Each particle was then tracked for 90 days using Ariane without dispersion and the daily flow fields for 2010 to 2012. The number of particles remaining in the basin at time t following release was then modelled as follows:

$$N(t) = N_R + N_E \, \mathrm{e}^{-t/\tau} \tag{6.1}$$

where N_R is the proportion of particles remaining on day 90, N_E is the proportion of particles that have left the basin by day 90, and τ is the e-folding time in days. Note $N_R + N_E = 1$. Plots of the observed proportion, and the fits of the above model, as a function of τ are shown in Figure 6.9 for two basins and two seasons. For all four cases the particles were released below 100 m. Table 6.1 lists the estimated parameter values for each case and the coefficient of determination, R^2, which is a straightforward measure of model fit. In each case R^2 is very close to 1 indicating a very good agreement between the observed values of $N(t)$ and the fitted curve. It can be seen that $35\% - 42\%$ of particles that originate in Emerald Basin remain after one season. By way of contrast the seasonal variation for Lahave Basin is much larger; only 30% are retained after one winter, and almost 50% after a typical summer. It is speculated that adding dispersion would increase the number of particles leaving a given basin, however no runs were performed to confirm this as the current version of Ariane does not have this capability.

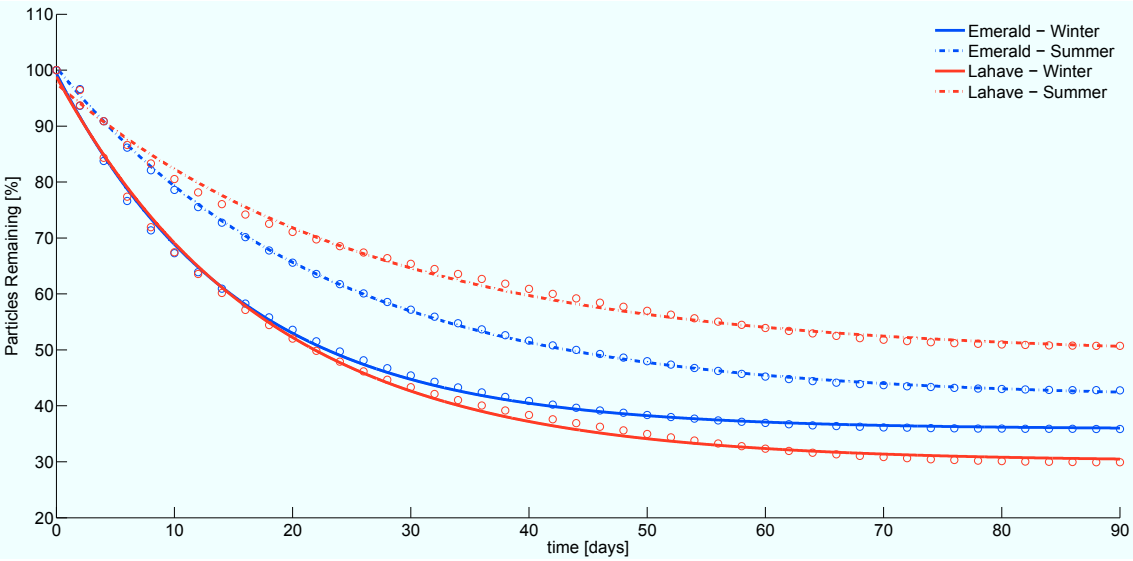

Figure 6.9: Retention times per basin by season for Emerald and Lahave Basins in winter and Summer. Open circles indicate data from particle trajectories while dotted and solid lines are fitted curves corresponding to those listed in Table 6.1.

Basin	Season	Fitted equation	R^2	e-folding
Emerald	Winter	$35.85 + 63.57e^{-0.066t}$	0.9971	15.15 days
Emerald	Summer	$41.37 + 59.14e^{-0.045t}$	0.9994	22.22 days
Lahave	Winter	$30.07 + 68.80e^{-0.057t}$	0.9966	17.54 days
Lahave	Summer	$49.03 + 48.61e^{-0.038t}$	0.9938	26.32 days

Table 6.1: Retention indices for Emerald and Lahave Basin in summer and winter. The form of the fitted model is given in equation (6.1). The coefficient of determination, R^2, is also given.

The retention indices listed in Table 6.1 are all for particles released at depths below 100 m: henceforth the "minimum release depth." The majority of basins are connected at depths of 100 m (Figures 5.5 and 5.6) and so particles released above 100 m are expected to be lost very quickly. At depths greater than the connections between the basins (i.e., depths greater than about 170 m) more particles are expected to be retained. These expectations are confirmed for Emerald Basin in Table 6.2, where the retention indices are listed for different minimum release depths, and also in the particle density plots shown in Figure 6.10.

Depth [m]	Fitted equation	R^2	e-Folding Time
100	$35.85 + 63.57e^{-0.066t}$	0.9971	15.15 days
150	$50.72 + 49.74e^{-0.044t}$	0.9992	22.73 days
170	$60.86 + 40.42e^{-0.035t}$	0.9993	28.57 days
200	$70.96 + 31.08e^{-0.033t}$	0.9976	30.30days

Table 6.2: Retention indices for Emerald basin by depth in the winter. Particles were released within Emerald Basin below the minimum depth at daily intervals for the month of January. The form of the fitted model is given in equation (6.1). The coefficient of determination, R^2, is also given.

Further figures and tables for Emerald in summer and Lahave in both seasons are given in Appendix E.

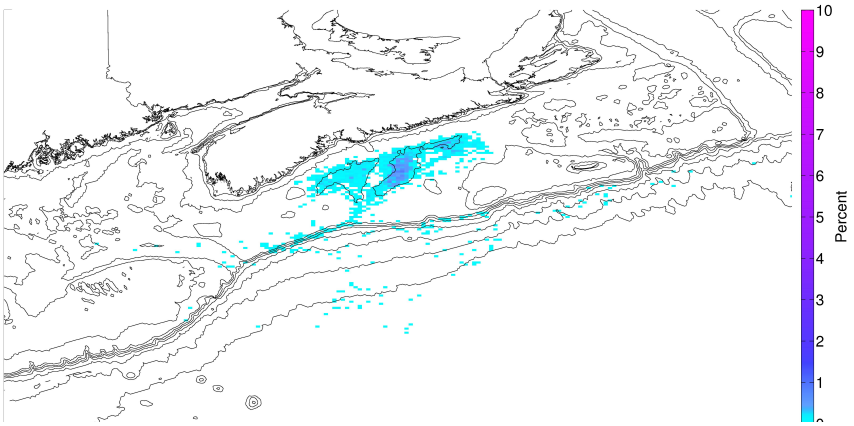

(a) Depth = 100m

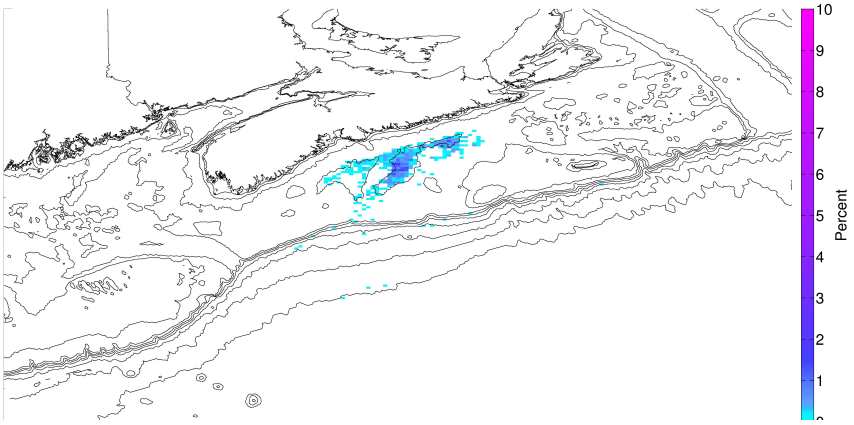

(b) Depth = 150m

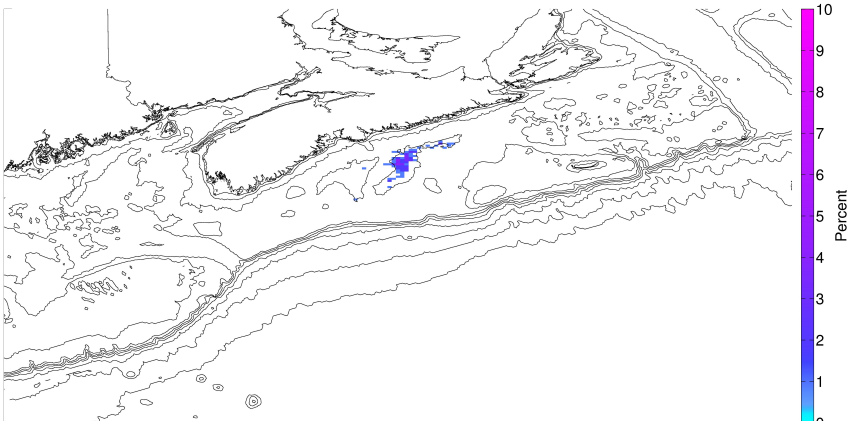

(c) Depth = 200m

Figure 6.10: Retention of particles in Emerald Basin for January 2010-2012 by minimum release depth. Particles were released over the full domain on January 1st and allowed to drift for 90 days. Colour indicates the locations of particles remaining in the basin as a percentage of those initiated in the basin (on day 1), below (a) 100 m (b) 150 m and (c) 200 m respectively. Blues and turquoise indicate low percentages, purples and magenta indicate high percentages. Note the colourbar ranges from 0 to 10%. Flow fields were daily snapshots as discussed in Chapter 5.

6.2 Connectivity Between Deep Basins

Although a significant proportion of particles are retained within a given basin, a substantial portion can end up in adjacent basins. Selective screening of particle trajectories reveals interbasin pathways, and connections between the basins and the shelf. Emerald and Lahave Basin are connected at their northeastern and southwestern tips providing two possible pathways. Figures 6.11(a) and 6.12(a) show that particles exiting Emerald Basin below 100 m typically enter Lahave Basin first using either connection before crossing the shelf break on the southwest side of the channel (Figure 6.12). Particles entering Emerald Basin from the south do so directly, using the eastern edge of the sill connecting the basins to the shelf break.

The variation in the strength of the Nova Scotia Current could provide a partial explanation for differences in pathway preference. The Halifax line is a reference line which extends southwest from Halifax, Nova Scotia, and passes over Emerald Basin. Figure 6.13 shows estimates of alongshore transport across the Halifax Line inferred from observations made by three ADCP located on the 100 m, 160 m and 180 m isobaths. The grey line shows daily changing transports and the black line is a 50 day moving average. Negative values indicate flow to the southwest. This figure indicates interannual and seasonal changes in transport. In general, the Nova Scotia Current is stronger in winter and weaker in summer (*Hebert et al.*, 2013). When the Nova Scotia Current is stronger, examination of many drifter trajectories (not shown) suggests that particles in Emerald Basin are more energetic, and tend to use either the northern or southern pathway. Interestingly, in summer when the Nova Scotia Current is (comparatively) very weak, particles released in Emerald Basin tend to either use only the northern or only the southern passage. It is hypothesized, that in the absence of the energetic NSC, other processes such as slope water intrusions can dominate circulation patterns. Much more research is needed to further quantify this hypothesis.

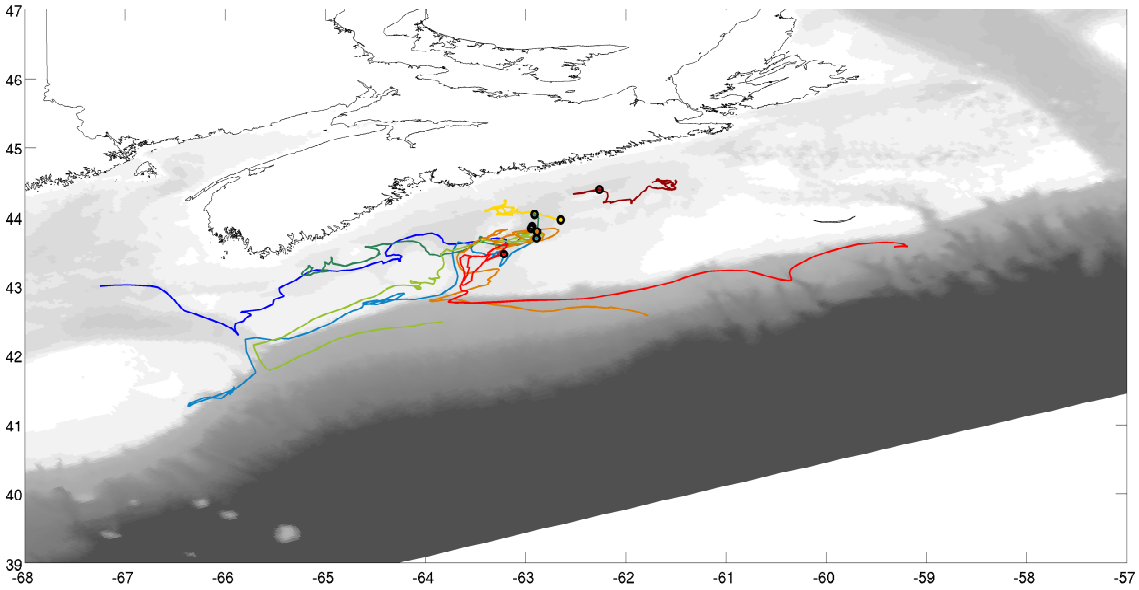

(a) Trajectories of particles exiting Emerald Basin - Winter

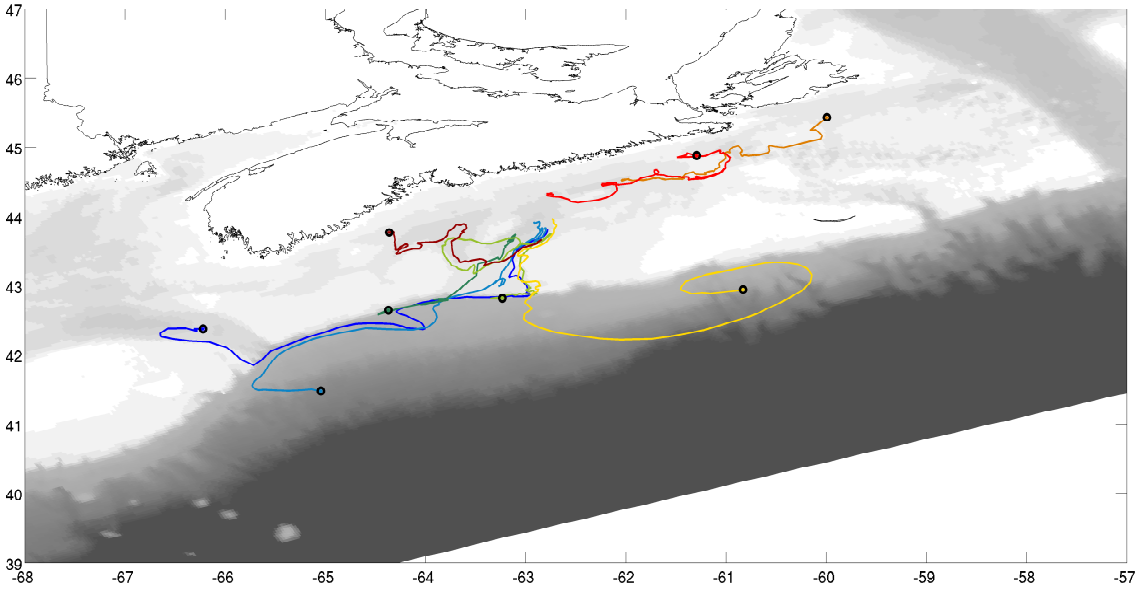

(b) Trajectories of particles entering Emerald Basin - Winter

Figure 6.11: Trajectories of particles entering and leaving Emerald Basin in winter 2010. Individual particle release position is indicated by the black circle. The trajectories were calculated using Ariane and hourly flow fields. Particles were released on January 1st, 2010 and allowed to drift for 90 days.

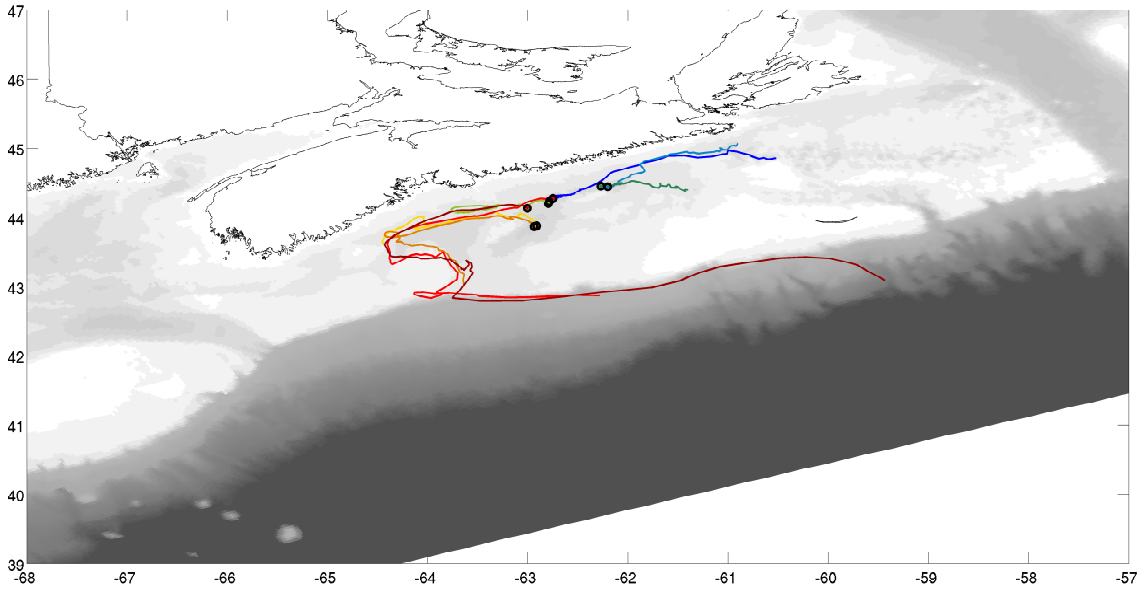

(a) Trajectories of particles exiting Emerald Basin - Summer

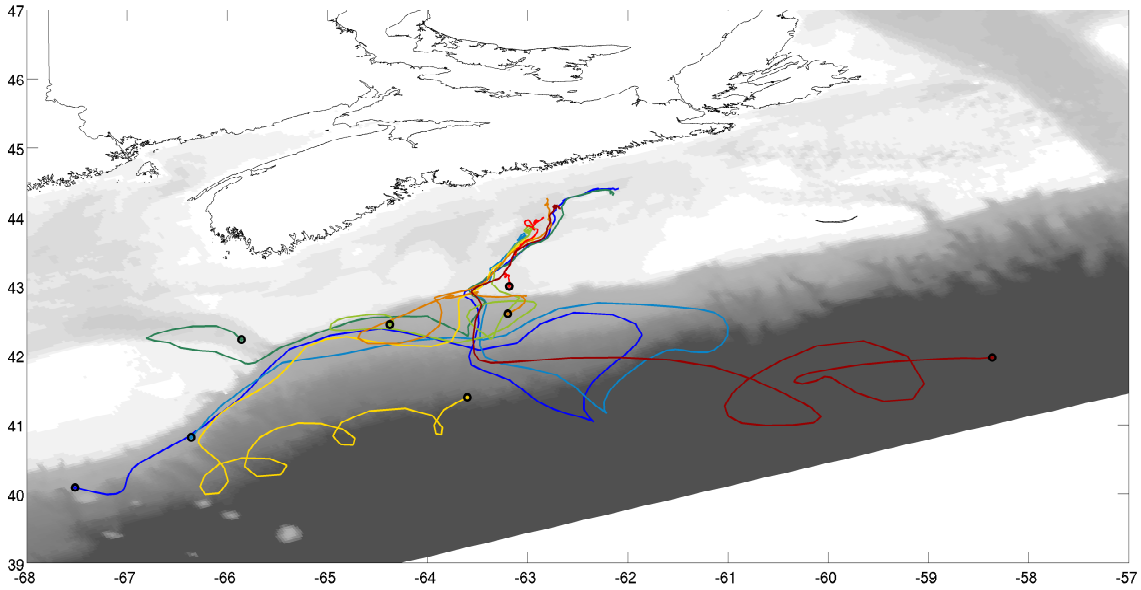

(b) Trajectories of particles entering Emerald Basin - Summer

Figure 6.12: Trajectories of particles entering and leaving Emerald Basin in summer 2010. Otherwise same as Figure 6.11.

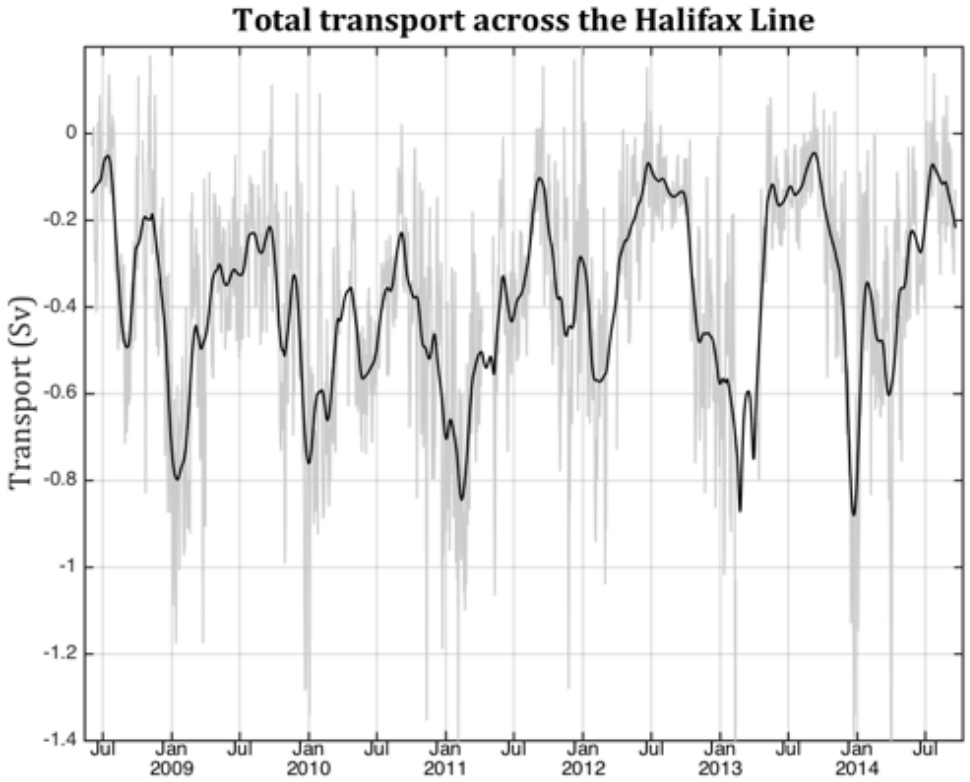

Figure 6.13: Seasonal variation of the transport across the Halifax Line. Total transport across the Halifax line in [Sv] for the years 2008 to 2014. The grey line shows the daily transports and the black line shows a 50 day moving average. Negative values indicate transport to the southwest. Figure kindly provided by Mathieu Dever (PhD student at Dalhousie).

6.3 Interannual Changes in Deep Basin Source Regions

Interannual and seasonal variations in source regions might be explained by the strength of the Nova Scotia Current (NSC). In winter Emerald Basin is sourced partially from the northeast, but more heavily from the south and southwest. During periods when the NSC is strong, the abundance of particles from the northeast increases and particles orginate further north. Figure 6.14 shows the positions of particles on January 1st that end up in Emerald Basin 90 days later. There are three plots, one for each winter of the year indicated. In 2012, the NSC is much weaker than in previous winters. Therefore it is expected that fewer particles from the northeast would end up in Emerald Basin. This is clearly demonstrated in Figure 6.14. In summer when the NSC is weaker, the northern influence is almost non-existent (Figure 6.15) with the exception of the summer of 2011 during which time the NSC was stronger than average.

Interestingly, Lahave Basin is sourced more extensively from the northeast in winter than Emerald Basin. In summer, it is almost exclusively sourced from the southwest. Again, the effect of the 2012 weaker winter NSC is evident in Figure 6.16. In 2010 and 2011 particles come from as far north as the Laurentian Trench. In 2012 the sources only start as far north as the southern edge of Cape Breton.

The above interpretation of particle movement, in terms of the NSC, is based purely on model predictions. It is therefore not surprising that there is a relationship between the two. The important suggestion made above is that the NSC can be seen as the main driver for the large scale changes in particle transport on both seasonal and interannual timescales. These seasonal changes can be quite large; for Lahave Basin, the seasonal retention indices varied by a factor of almost two between seasons. It is interesting to note that the seasonal cycle in Katavouta's model is too weak in winter. Therefore, it is expected that seasonal variation in transport and retention is likely greater in reality than shown here.

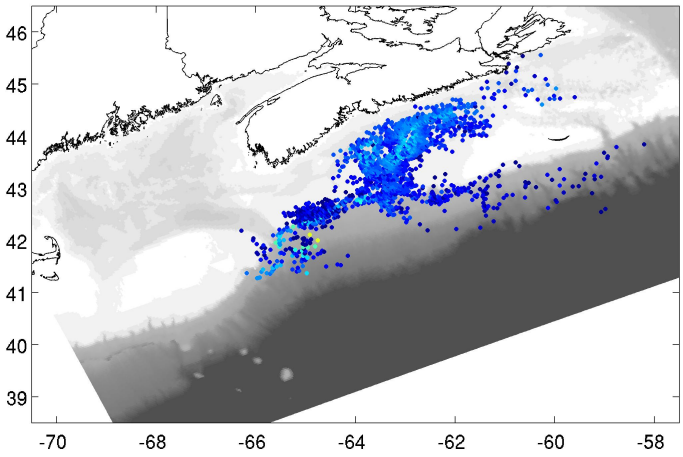

(a) 2010

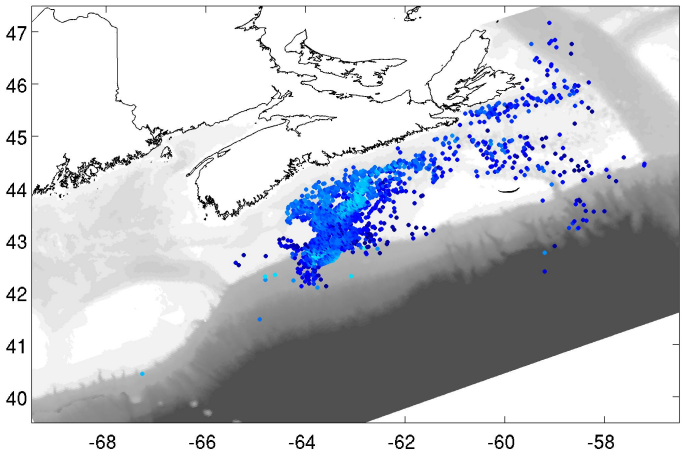

(b) 2011

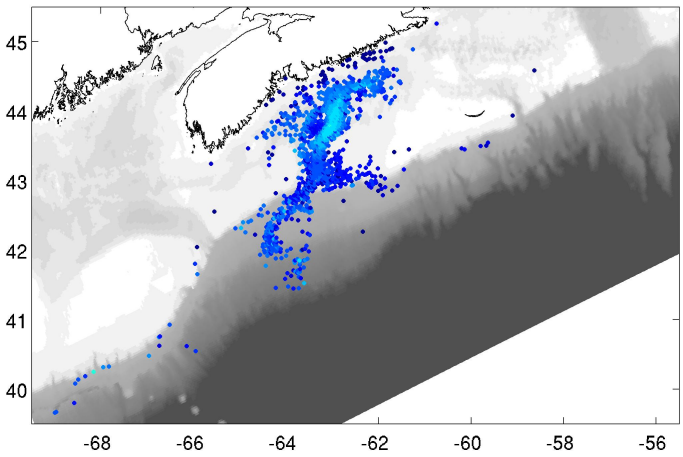

(c) 2012

Figure 6.14: Sources of particles in Emerald Basin in Winter by year. Particles were released over the full domain of the regional model on January 1st of the respective year and allowed to travel for 90 days in daily changing flow fields. All panels show the particle location (on day 1) for particles that were in the basin below 100 m on day 90. Colour indicates the depths at which the particles were released. Dark blue means surface particles; light blue means near bottom release.

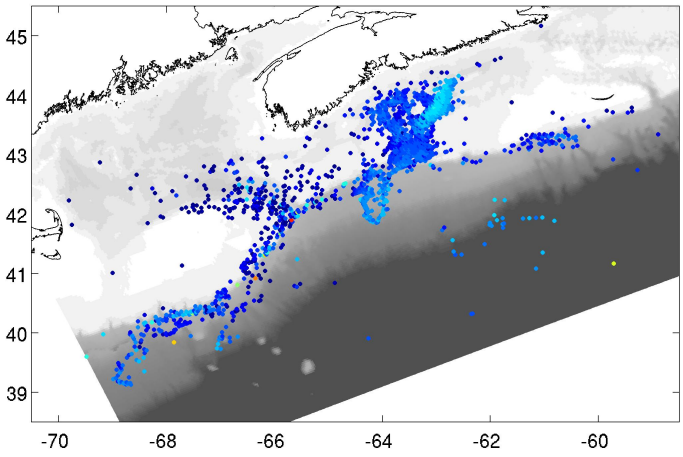

(a) Sources - 2010

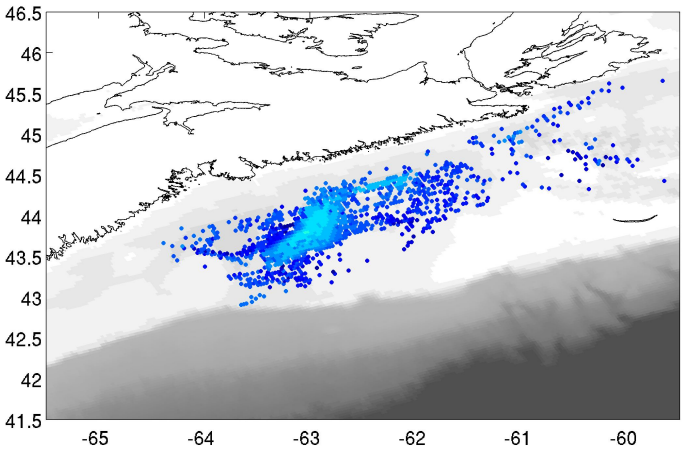

(b) Sources - 2011

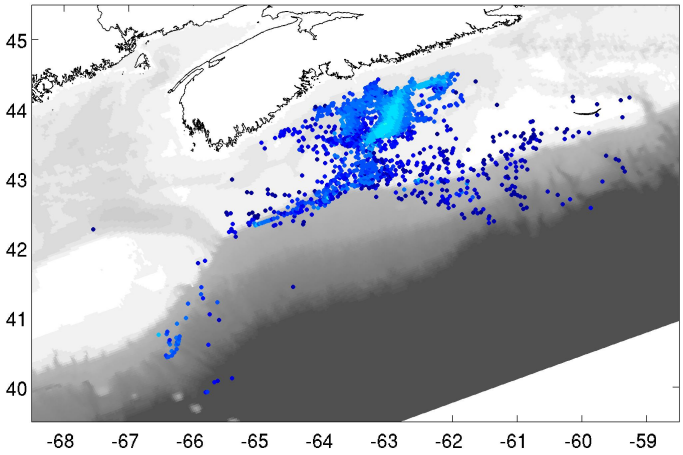

(c) Sources - 2012

Figure 6.15: Sources of particles in Emerald Basin in summer by year. Otherwise same as Figure 6.14.

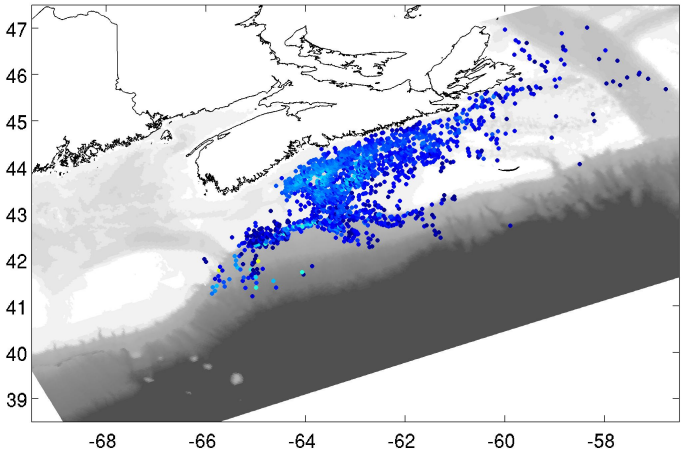

(a) Sources - 2010

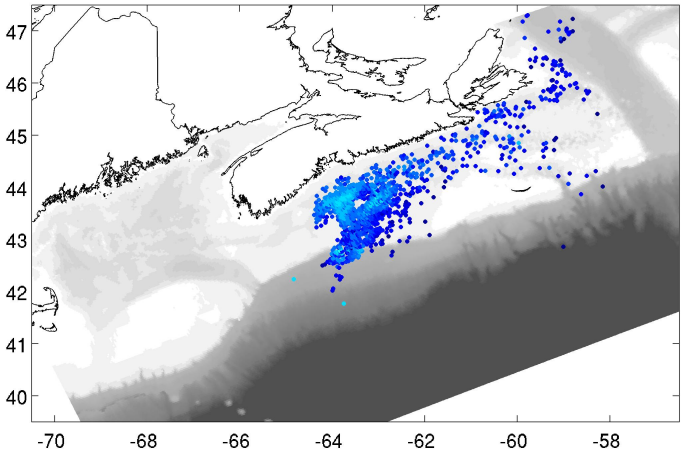

(b) Sources - 2011

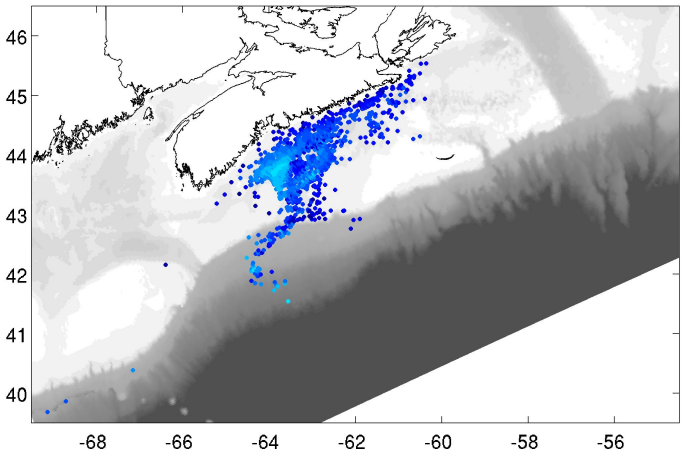

(c) Sources - 2012

Figure 6.16: Sources of particles in Lahave Basin in winter by year. Otherwise same as Figure 6.14.

CHAPTER 7

SHORT TERM PREDICTIONS OF SEARCH AND RESCUE OBJECTS ON THE SCOTIAN SHELF

One of the main challenges in a Search and Rescue (SAR) operation is the creation of an appropriately sized search area. This area must be large enough to enclose a SAR object, but small enough to be searchable by available resources within the expected survival time of a missing person. As discussed in Chapter 3, there are several sources of uncertainty to take into account that include, but are not limited to, uncertainty in the last known position and time of the SAR object's disappearance, and also errors in the forecasts of wind and current (including the contribution of subgrid scale processes).

7.1 Accounting for Uncertainty in Last Known Position and Time

Ariane does not have many built in mechanisms to account for SAR uncertainty. Section 3.2.1 demonstrates that it is possible to add dispersion to account for grid-scale perturbations not captured by the flow fields themselves. It is straightforward to add a subroutine to Ariane to incorporate uncertainty in the wind by simply adding random perturbations to the input fields. One of Ariane's strengths is flexibility in defining the initial release position and time. While the cone of drop points created by LEEWAY is somewhat customizable,

Ariane can initiate particles at any specified set of points to account for differing scenarios, such as a boat swamping at a known time but unknown position (Figure 7.1(a)) or a person falling overboard at some point during a vessel's transit (Figure 7.1(b)).

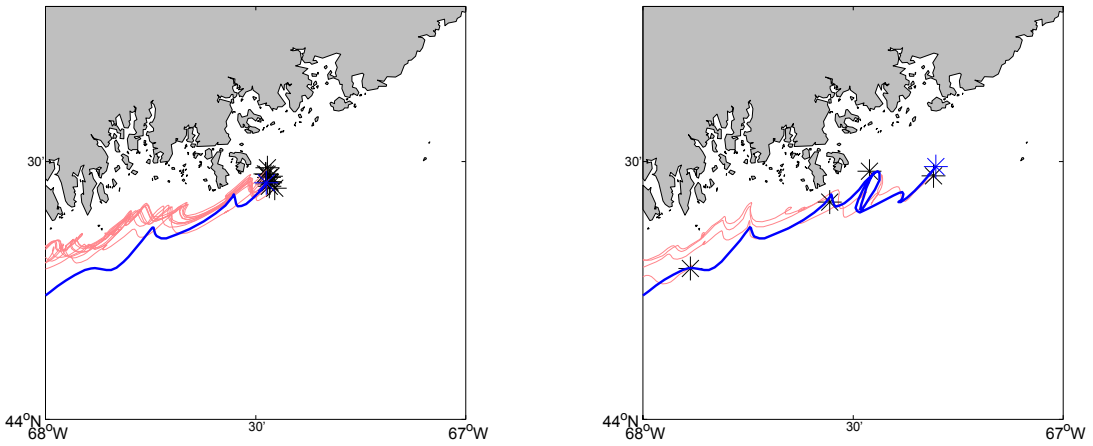

(a) Vary position of particle release

(b) Vary time of particle release

Figure 7.1: Taking into account uncertainty in initial conditions in a SAR using Ariane. The two panels show how to take into account uncertainty in the (a) position and (b) time of the last known position of the search object. For both panels the blue line indicates the observed track of a drifter, the black stars indicate release location, and the red tracks show trajectories predicted by Ariane. These panels are based on real drifter data off the coast of Maine and will be discussed later.

7.2 Two Worked Examples

In order to evaluate the performance of Ariane in a realistic setting, two observed trajectories are now compared against Ariane's predictions. The first trajectory is located on the outer Scotian Shelf and along the shelf break and is subject to meanders of the Gulf Stream and associated eddies (Figure 7.2). The trajectory was kindly provided by Dr. Tsubasa Kodaira who obtained them from the data archive of the Surface Velocity Program. The drifter was drogued at 15 m and followed from August 22nd to September 21st, 2010. This trajectory clearly demonstrates the tidal influence within a rotating feature.

The second trajectory is located in the near shore environment of the Gulf of Maine Figure 7.2). The drifter data were obtained from the NOAA website. [1] The drifter was drogued to 1 m and drifted from May 30th to June 29th, 2011. This trajectory is clearly influenced by the coastline.

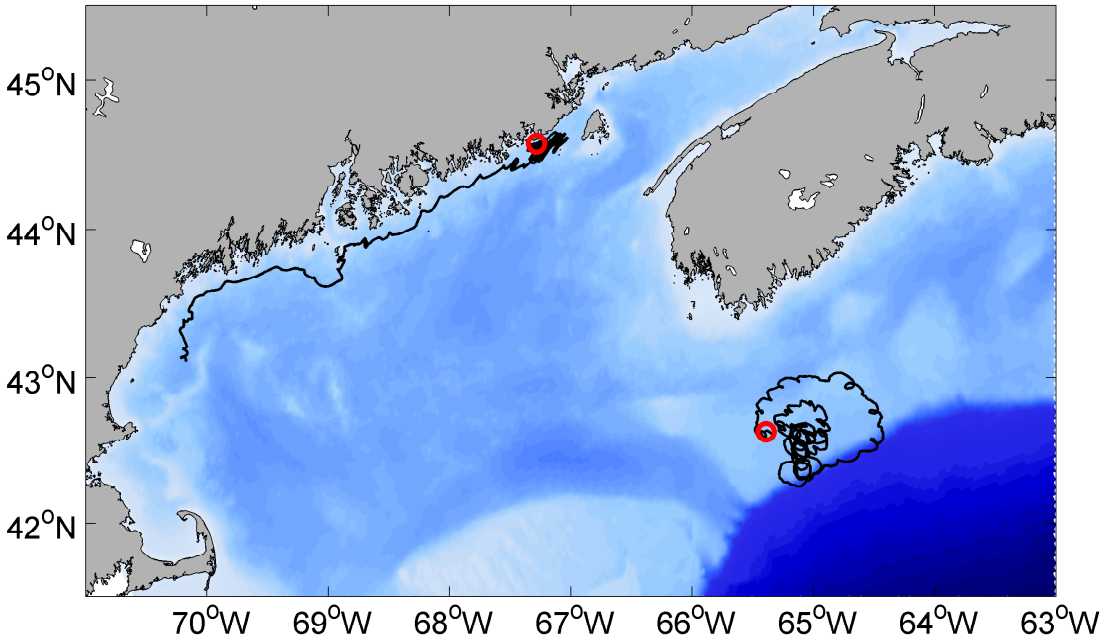

Figure 7.2: Observed drifter tracks on the outer Scotian Shelf (right) and near shore of the Gulf of Maine (left). The drifters were drogued at 15 m and 1 m respectively and were observed from August 22nd to September 21st, 2010 and May 30th to June 29th, 2011 respectively. Red circle indicates release point.

[1] http://www.nefsc.noaa.gov/drifter/index.html

Ariane's predictions were made using hourly, near surface flow fields that included the tides as discussed in Chapter 5. Particle ensembles were released within 5 km of the observed track at daily intervals for 1 month. The only uncertainty in the calculations arises from the variation of release point as the current version of Ariane does not include the ability to add dispersion. Wind fields and leeway effects were not used. Drifters in the model were surface trapped at a depth of 0.35 m due to restrictions of the available flow fields.

7.2.1 Predicting trajectories near the shelf break

Ariane's predictions were poor on the shelf break. The velocities predicted by the regional model are too strong. This is not surprising given that the model is known to perform poorly in deep water as discussed in Chapter 5. Another reason for the discrepancy is the drifter is drogued at 15 m while the predictions are trapped at 0.35 m. This almost certainly leads to an overestimation of the effect of the wind (through the surface current) on the predicted drifter trajectory. For this example, the use of the last known position as a SAR predictor would be a better choice.

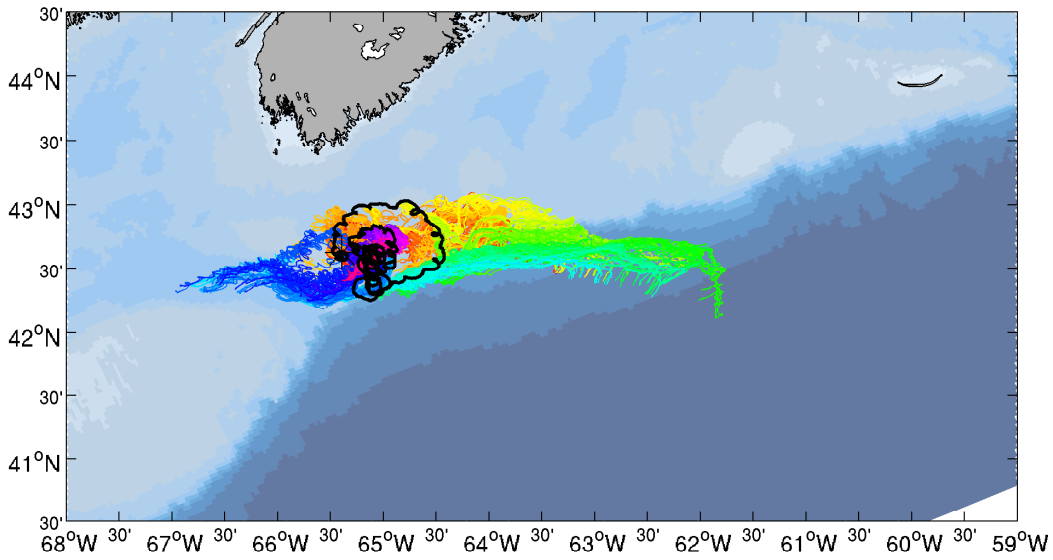

Figure 7.3: Comparing Ariane against surface drifter observations on the Scotian Shelf. Ariane's starting positions were initialized in 24 hour increments along in the vicinity of the observed track (black line) and allowed to drift from August 22nd to September 21st, 2010. Ariane's drifter trajectories are colour coded (red to purple) according to release point along the track in time and space. For example, the red colours are released on day 1 and drift for 30 days while the purples are released closer to the end of the observed track and will drift for only 1-2 days.

7.2.2 Predicting trajectories near the coast

Ariane's predictions are much improved near the coast. The velocities predicted by the regional model are generally too weak. As noted above, differences between the depth of the drifter drogue and the model may contribute to the discrepancy. For this example, the model does provide useful information on future positions of a SAR object.

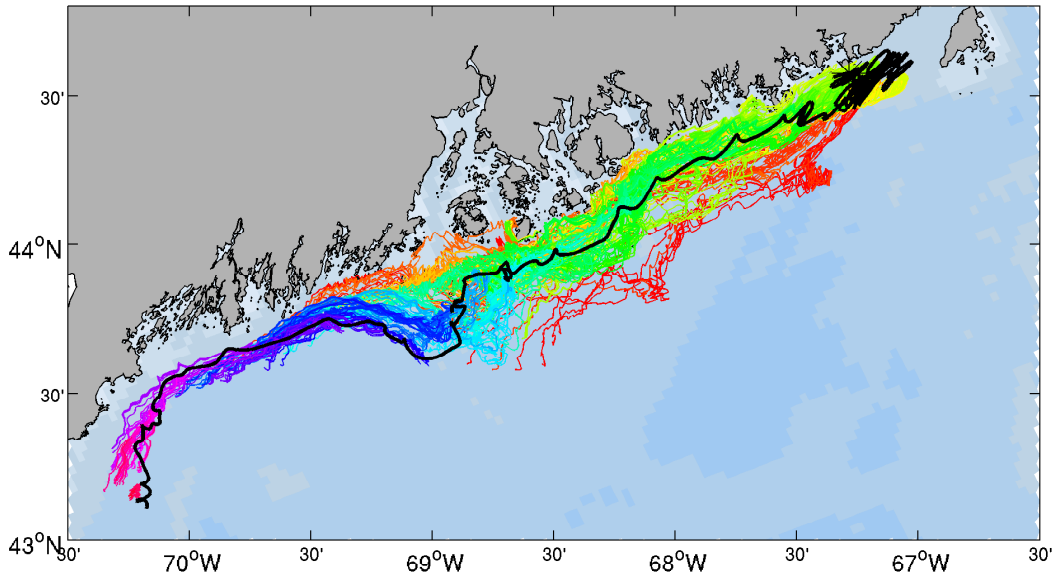

Figure 7.4: Comparing Ariane against surface drifter observations in the Gulf of Maine. Ariane's starting positions were initialized in 24 hour increments along in the vicinity of the observed track (black line) and allowed to drift from May 30th to June 29th, 2011. Ariane's drifter trajectories are colour coded according to release point.

7.3 Identifying the Predictability of a Flow Field

A useful way to visualize Aref's flow fields is to calculate a displacement map showing how a particle moves over one blink of the two vortices. This reveals (not shown) that there are certain critical locations within the flow field for which very small changes in the release position lead to very large changes after one blink of the system. This leads to the Lagrangian Chaos illustrated in Figure 2.2. It is interesting to ask if similar critical points exist along the observed trajectories shown in Figure 7.5.

Detection of “critical points”, and also “critical times” is possible using Ariane. By definition, particles that are released away from critical points but within a short distance from each other will have similar trajectories. On the other hand, two slightly displaced particles can have dramatically different trajectories if they pass close by a critical point. An example using real tidal flow fields for Haro Straight on the West Coast of Canada is shown in Figure B.3 in Appendix B. Critical times could result from errors in the wind field that become large at a given time.

One simple way of identifying a critical point is to examine the growth in separation of trajectories of particles with similar release points. High separation growth rates indicate regions of low predictability. Figure 7.5 shows the observed tracks in black with the mean predicted track in red for latitude (top) and longitude (bottom) as a function of time. The growing error in latitude or longitude (grey swatch) are shown for the near shore Gulf of Maine trajectory (left) and the outer Scotian Shelf trajectory (right). For both trajectories the error is small for the first few days. However, in the bottom left panel of Figure 7.5, corresponding to the near shore trajectory, the error in longitude increases rapidly around June 4th. Similarly, in the bottom right panel there is a rapid increase in error around September 12th for the shelf break trajectory. These sudden error growths identify “critical points” in the velocity fields. It is speculated that the critical point for the shelf break example is due to errors in the wind driven currents. For the near-shore example, it is speculated that the critical point is associated with small scale variations in the tidal flow leading to the type of Lagrangian chaos predicted by Aref’s blinking vortex.

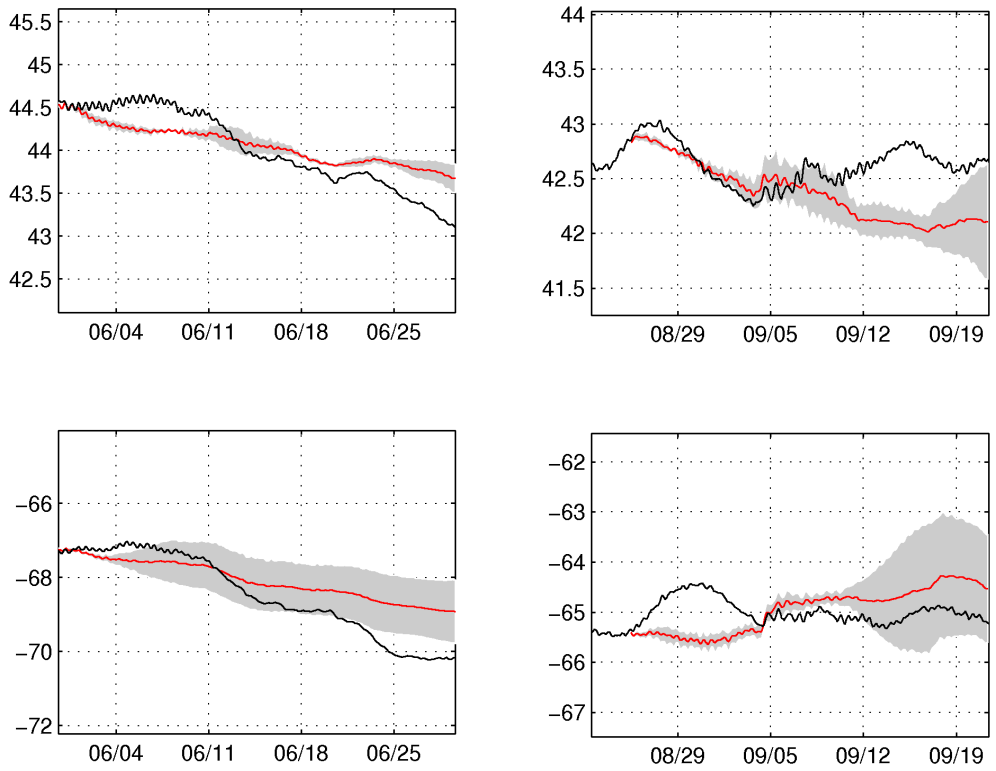

(a) Nearshore of the Gulf of Maine trajectory error

(b) Outer Scotian Shelf trajectory error

Figure 7.5: Surface flow field predictability in the Gulf of Maine and outer Scotian Shelf. Left two panels show drifter latitude and longitude (black line) by date for the near shore Gulf of Maine trajectory. Right two panels show drifter latitude and longitude (black line) by date for the outer Scotian Shelf trajectory. In all panels the mean latitude and longitude of the predicted tracks is shown in red with the error shown as a grey swatch.

One way of quantifying the performance of predictions is by plotting the minimum error between the forecasts for a given time and the observed position. This method was proposed by *Lynch et al.* (2001). They found the mean error growth rate between observed drifter tracks and predictions over Georges Bank was 3.4 km/day. Applying their method to the two examples above, Ariane's predictions have a mean error growth of 5.83 km/day for the Gulf of Maine coastal trajectories and 7.06 km/day for the deeper ocean Scotian Shelf trajectory. The error growth in both of Ariane's predictive scenarios are of the same order of magnitude as found by *Lynch et al.* (2001). While the particle tracking method of *Lynch et al.* (2001) was not discussed, their experiment had several distinct advantages regarding the ocean model: (i) current meter observations from ACDPs and satellite (ARGOS) trajectories were assimilated, (ii) meteorological data from shipborne sensors were used to improve atmospheric forcing fields.

It is clear that the performance metric proposed by *Lynch et al.* (2001) is optimistic because it uses the best forecast. A more conservative approach is to examine the complete ensemble of forecasts and compare their error growth rate to that of the last known position as a predictor of future position. This is illustrated in Figure 7.5.

CHAPTER 8

SUMMARY AND DISCUSSION

Two main classes of methods for predicting where objects come from, and go to, have been reviewed. The first solves a Fokker-Planck equation for the evolution of the probability distribution function, $p(x,t)$, of particle position (*Gardiner*, 2009). It is interesting to note that this equation is linear in $p(x,t)$ and in that sense it is relatively simple. The second class of methods involves integration of a stochastic differential equation (SDE) for the position of a single particle (*Gardiner*, 2009). The governing equation is usually highly nonlinear because the velocity is usually a nonlinear function of position and time. This study focused on the SDE approach and two types of method were described and evaluated. The most conventional method is based on discretization in time with the simplest approach being a uniform discretization with a constant dt. The second method is based on discretization of space. While this second method is less common, it is highly efficient.

Both the discrete time (DT) and discrete space (DS) methods were evaluated using three idealized examples which were chosen to represent oceanographically relevant flow regimes (a vortex, a blinking tidal flow, and a turbulent flow field with spatially varying diffusivity). Overall the DS method, based on the publicly available Ariane code, was shown to perform extremely well for all three idealized examples. (Note that idealized examples relevant to other non-oceanographic flow regimes could be constructed

to illustrate superior performance of DT methods.) It was also shown how the DS method could be readily extended to include dispersion associated with grid scale turbulence.

The hypsometric curve was extended to provide a simple way of counting deep basins as a function of depth. It was shown that the maximum number of isolated deep basins occurred at a depth of about 160 m. Between depths of 180 m and 220 m the number of isolated basins was five (e.g., Emerald, Lahave and Roseway Basin). This extension of the hypsometric curve proved useful in the design of a set of tracking experiments to quantify retention, interbasin exchange and also exchange between the shelf and deep ocean using the DS method.

Hourly and daily flow fields generated by Anna Katavouta (PhD student at Dalhousie University) were used to quantify retention within deep basins of the Scotian Shelf. It was shown that the number of retained particles initially dropped exponentially, with an e-folding time of tens of days, toward a value that changed much more slowly with time (longer than a season). It was also shown that the number of particles retained for more than a season depended on the time of year. For Lahave Basin for example, almost 50% of the particles released below 100 m remained over the summer, compared to only 30% over the winter. Interbasin exchange was visualized using conditional probability density functions of particle position to indicate where particles come from, and where they go. Their dependence on season and minimum depth of release was also quantified. This method of visualizing particle movement is already being used by colleagues at Dalhousie University working on the spatial distribution of whales in the region.

Seasonal and interannual changes in the strength of the Nova Scotia Current (NSC) were quantified using transport estimates calculated by Mathieu Dever (PhD student at Dalhousie University) from ADCP measurements for the period 2008 to 2014. The present study showed a strong covariation of the NSC transport and the movement of particles from

their deep basin origins across the shelf. It is hypothesized that the NSC is an important driver of the particle density distributions on both seasonal and interannual times scales. This is of practical interest because the strength of the NSC is the subject of an ongoing monitoring programme.

The DS method was also used to predict the observed movement of near surface, drogued drifters. Better results were obtained for the inner shelf region of the Gulf of Maine compared to the vicinity of the shelf break. This is not unexpected given the difficulty in correctly predicting the position and intensity of offshore meanders and eddies using an ocean model that does not assimilate observations. The trajectory predictions for the inner shelf showed that the regional circulation model with DS tracking does have useful skill. The importance of correctly modelling critical locations that can limit predictability (reminiscent of the critical points that control the Lagrangian chaos in Aref's blinking vortex) was highlighted.

With regard to future work, there is potential to improve significantly the representation of dispersion in the DS method. This would make the method a much more useful tool for SAR applications where it is essential to include uncertainty in wind fields and ocean currents. It has already been shown here how to add grid scale turbulence through the use of random stream function values defined at the corners of the grid boxes. In terms of practical implementation it is important to note that the random stream values can be calculated within the Ariane program itself and they are only required for grid boxes containing particles. This will reduce greatly the computational cost of this scheme. Another potentially useful extension could be to allow the random fluctuations to be correlated through time. i.e., add persistence to the turbulent velocities (*Lynch et al.*, 2015).

Future work could also focus on the addition of particle "personality" to the tracking scheme. This would greatly assist in both chemical and biological applications. Colleagues

are already implementing this technique to predict copepod abundance and distribution within Emerald, Lahave and Roseway Basin. The changing temperature and salinity along a particle's path could also be tracked in order to monitor the marine environment (e.g., temperature, salinity or density) experienced by the particle. It would then be straightforward to develop a subroutine to allow particles to select a preferred condition and thereby respond to the environment.

Ariane is designed to work with finite difference grids. To my knowledge this approach has not been extended to work with finite element grids. Given the ability of such grids to provide high resolution in the coastal regions where it is required, such an extension would appear to be worthwhile.

APPENDIX A

MATLAB VERSION OF ARIANE

As a demonstration of the exact reproduction of the Ariane methodology described in Section 3.2, streamlines for surface trapped particles were calculated using Ariane and the Matlab version using steady, time independent flow field and changing, time dependent flow fields. The results are shown in Figure A.1 with the trajectory calculated by Ariane displayed as the hashed blue line while the trajectory generated by the Matlab code is shown by the solid red line. Both examples were generated using a NEMO flow field on a C-grid for barotropic tidal flow in the vicinity of Haro Strait and the Strait of Juan de Fuca kindly provided by Dr Vasily Korabel. Particles were initiated off the southern tip of Vancouver Island in the vicinity of Victoria, BC. Their start position is indicated by the black star in both images. The trajectory shown in Figure A.1(a) was produced using a daily averaged flow field with particle positions calculated over the span of twenty-four hours in an unchanging flow field. Figure A.1(b) shows trajectories produced from an hourly changing flow field, for the duration of fifty hours.

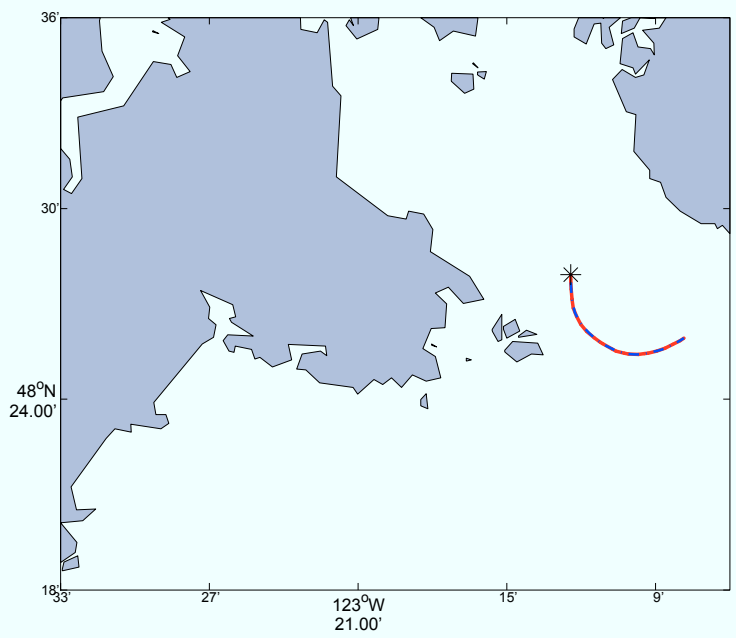

(a) Particle trajectories in a steady NEMO flow field over the course of 24 hours.

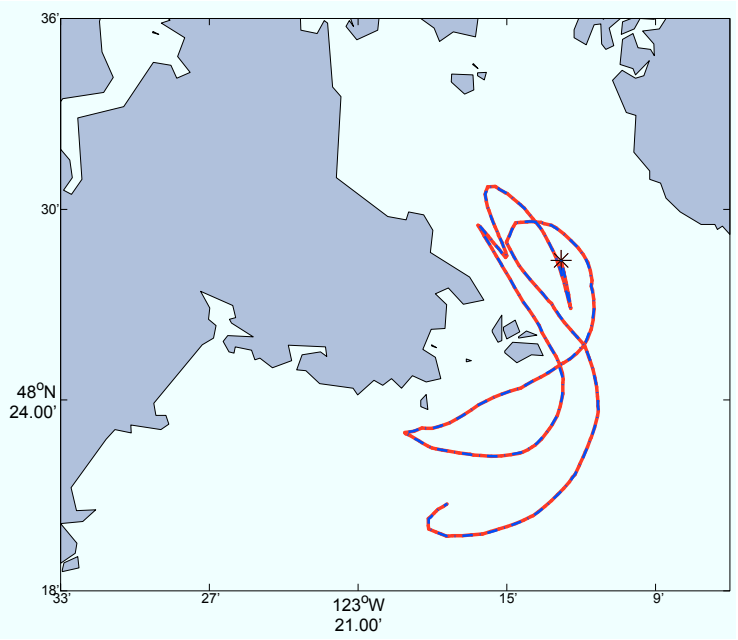

(b) Particle trajectories in a changing, time dependent NEMO flow field over the course of 50 hours.

Figure A.1: Comparison of Ariane trajectories against Matlab code. Particles were initiated off the southern tip of Vancouver Island in the vicinity of Victoria, BC. Their start position is indicated by the black star in both images. Left hand panel shows daily averaged flow field with particle positions calculated over the span of twenty-four hours in an unchanging flow field. Right hand panel shows trajectories produced from an hourly changing flow field, for the duration of fifty hours. In both panels Ariane's trajecory is shown as the blue hashed line and the trajectory calculated using the Matlab reproduction is shown as the red line.

APPENDIX B

ADDING DISPERSION TO ARIANE

As described in Chapter 3, dispersion was added to the DS method. Typical dispersion experienced in a null field with increasing time and constant D shown in Figure (B.1). In comparison, Figure (B.2) demonstrates how the dispersion relationship discussed in Section 3.2.1 becomes significantly less accurate as the level of dispersion approaches the size of the grid spacing. Therefore, care must be taken when choosing levels of dispersion to add to flow fields.

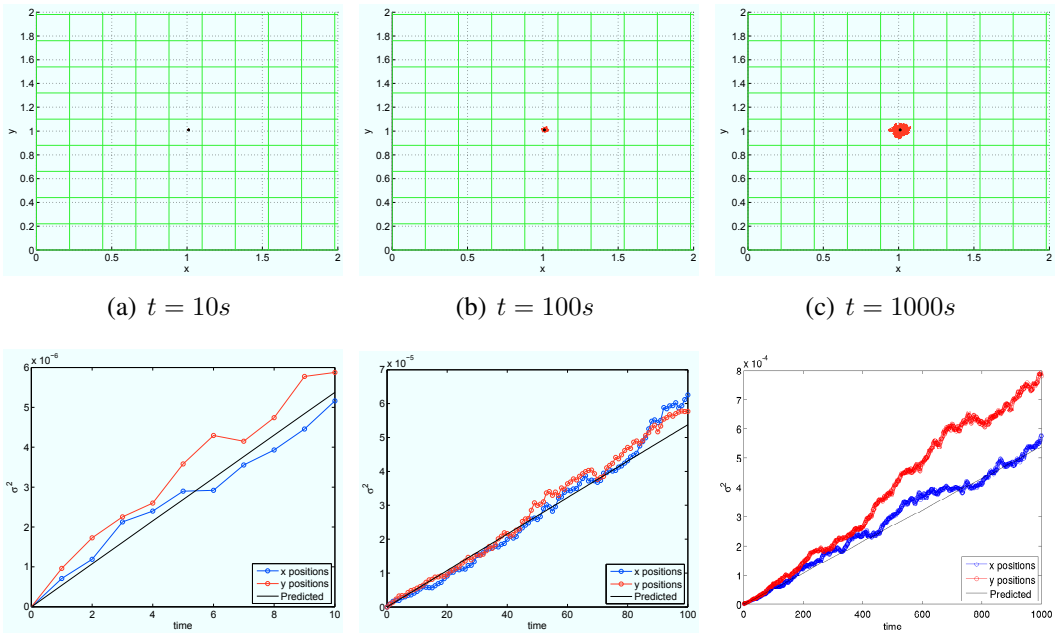

(a) $t = 10s$ (b) $t = 100s$ (c) $t = 1000s$

(d) $t = 10s$ (e) $t = 100s$ (f) $t = 1000s$

Figure B.1: Adding dispersion to Ariane. 500 particles were released at point (1,1) indicated by the black cross. The top panels show particle trajectories calculated using the DS method in a constant dispersive flow at time (a) 10, (b) 100 and (c) 1000. The bottom panels show the variance of the ensemble of particle positions as a function of time assuming constant D. The blue(red) line shows the variance of $x(y)$ position at time (d) 10, (e) 100 and (f) 1000. The theoretical predictions by (3.20) are shown by the black line. $(D = 10^{-7})$

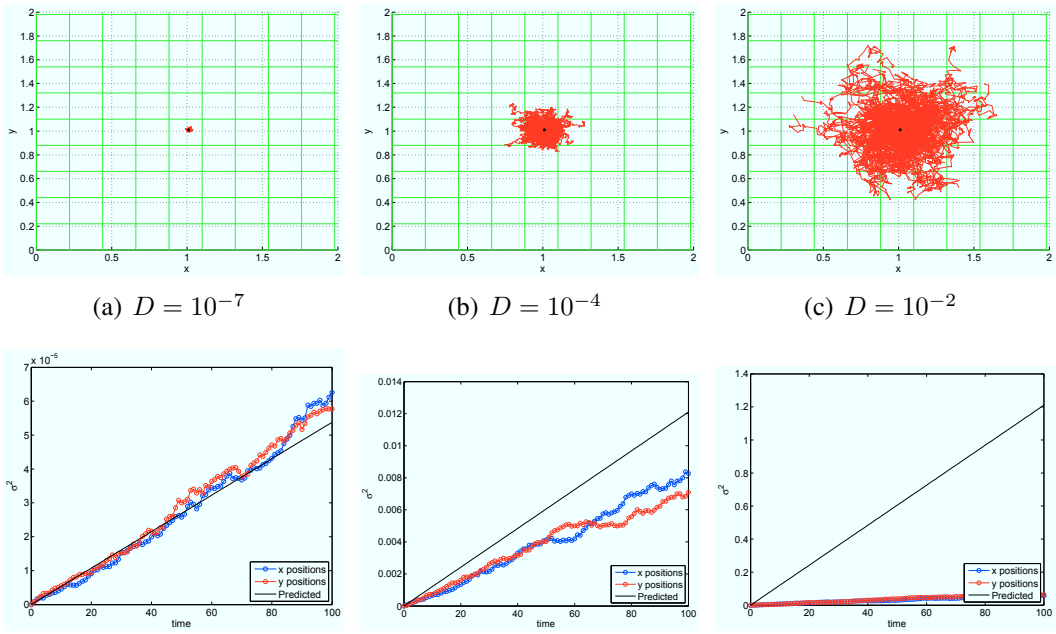

(a) $D = 10^{-7}$ (b) $D = 10^{-4}$ (c) $D = 10^{-2}$

(d) $D = 10^{-7}$ (e) $D = 10^{-4}$ (f) $D = 10^{-2}$

Figure B.2: Adding dispersion to Ariane with changing dispersion values. 500 particles were released at point (1,1) indicated by the black cross. The top panels show particle trajectories calculated using the DS method, for 100 time units in a changing dispersive flow with D values: (a) 10^{-7}, (b) 10^{-4} and (c) 10^{-2}. The bottom panels show the variance of the ensemble of particle positions as a function of time assuming constant D. The blue(red) line shows the variance of $x(y)$ position at time (d) 10^{-7}, (e) 10^{-4} and (f) 10^{-2}. The theoretical predictions by (3.20) are shown by the black line.

Expanding this to the case of the time varying flows off the coast of Victoria, BC, discussed in Appendix A, varying levels of dispersion were added to the original trajectory shown in Figure A.1. As demonstrated in Figure B.3, a slight variation in a particle's trajectory can have a big impact on the final position. A "critical point" in the flow field (as discussed in Chapter 7) is apparent in panel $(b - d)$ of Figure B.3. Just to the right of the drop position (indicated by a black star) the particles either curve back down to the south or continue north. This results from particles being at that point of flow at a slightly different time.

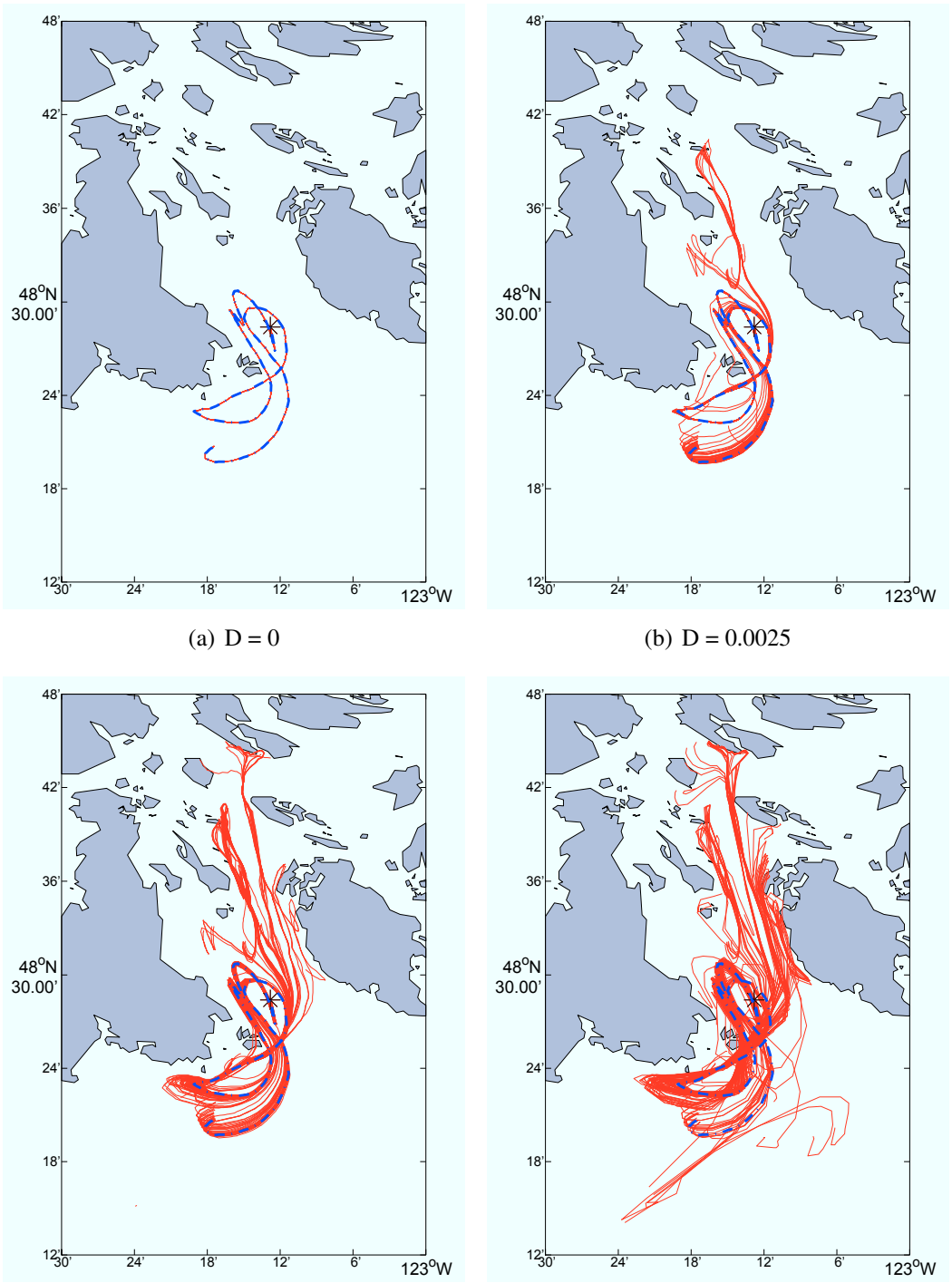

(a) D = 0

(b) D = 0.0025

(c) D = 0.0625

(d) D = 0.25

Figure B.3: Trajectories of 100 particles in hourly varying flow fields in Haro Stait over 50 hours. Calculated using the Matlab reproduction of the Ariane model with varying levels of dispersion added. The blue hashed line indicates the original trajectory shown in Figure A.1(b) while the red solid lines indicated individual particle trajectories. Dispersion values are: (a) 0, (b) 0.0025, (c) 0.0625 and (d) 0.25

APPENDIX C

SUPPLEMENTAL FIGURES FOR CHAPTER 4

The DT and DS methods were applied for three idealized examples. Figures here are provided as supplemental figures for Subsections 4.2 and 4.3.

C.1 Aref's Blinking Vortex

Particle trajectories calculated using the DT and DS methods (red line) against Aref's analytically calculated trajectory (black) are shown with a decreasing dt and dx respectively. In all figures the left hand panels show the calculated trajectories. Right hand panels show the change in x position and the change in y position with time.

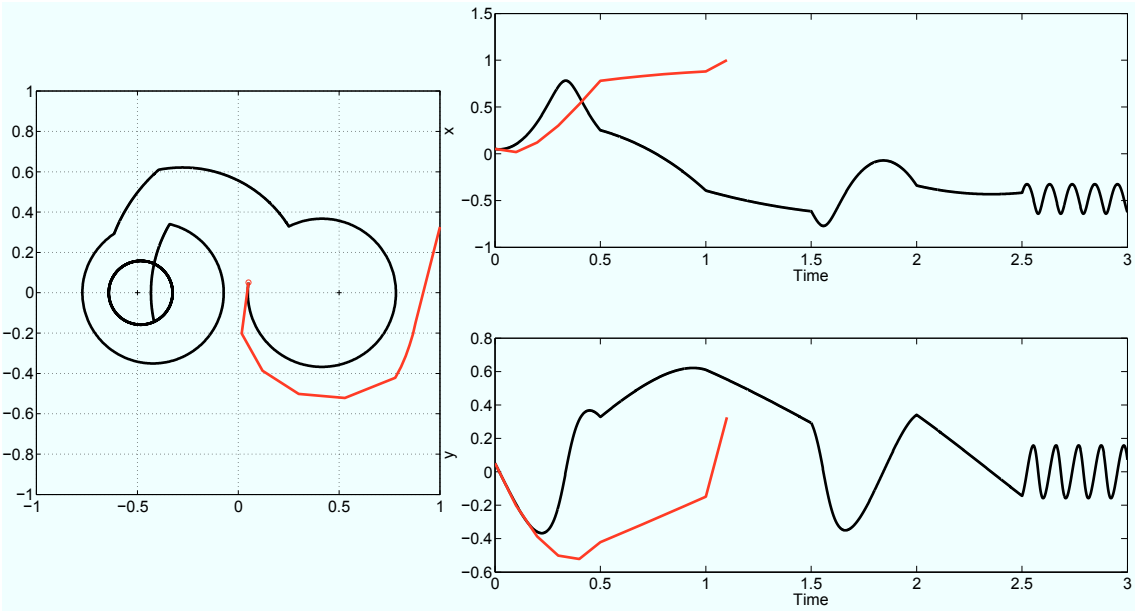

Figure C.1: Particle trajectory calculated using DT method (red line) against Aref's analytically calculated trajectory (black). Left panel shows the trajectory around the center. Right hand panels show the change in x position and the change in y position with time. dt is 0.1.

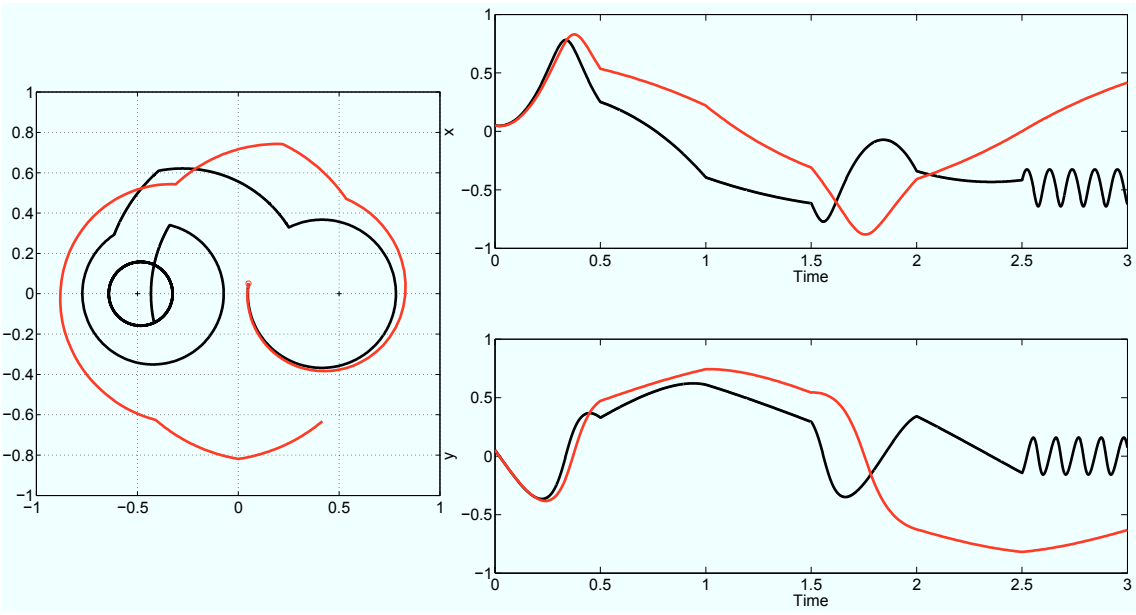

Figure C.2: Particle trajectory calculated using DT method (red line) against Aref's analytically calculated trajectory (black). dt is 0.01; otherwise as Figure C.1.

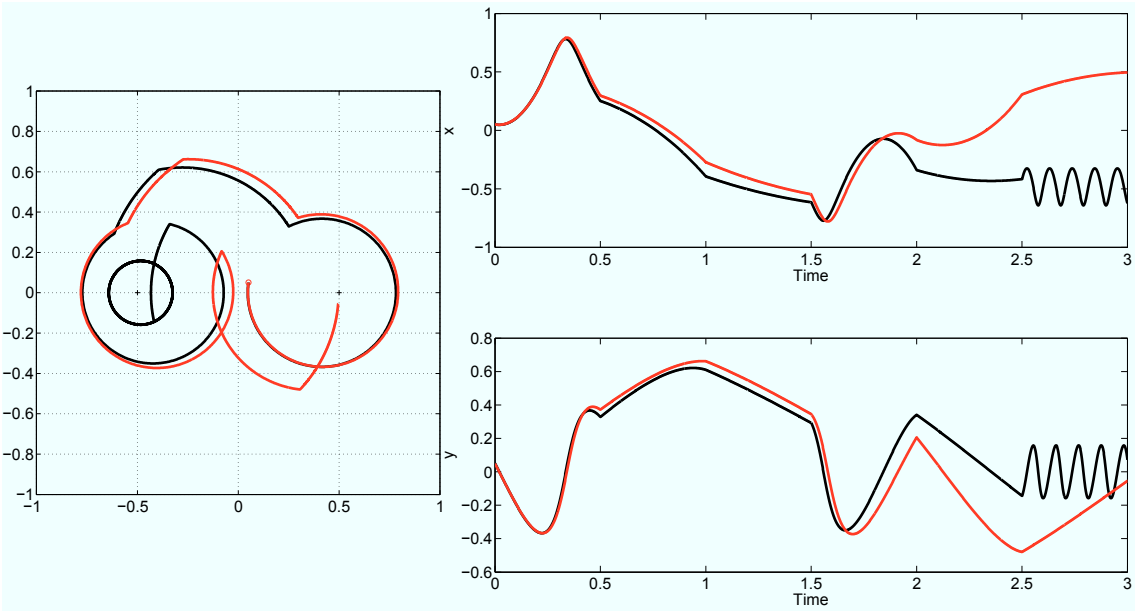

Figure C.3: Particle trajectory calculated using DT method (red line) against Aref's analytically calculated trajectory (black). dt is 0.001; otherwise as Figure C.1.

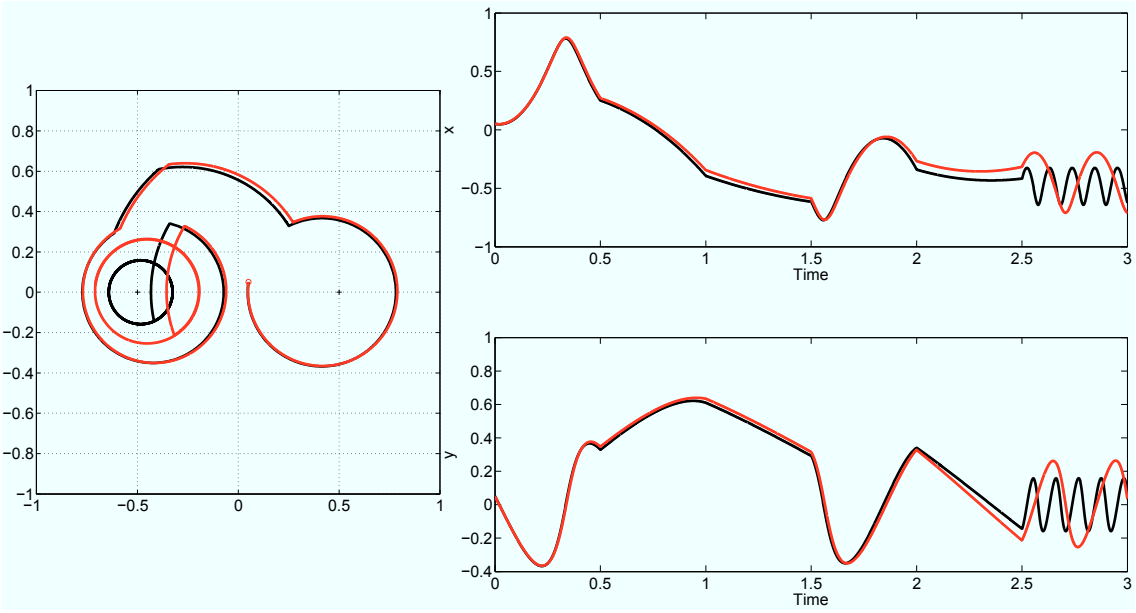

Figure C.4: Particle trajectory calculated using DT method (red line) against Aref's analytically calculated trajectory (black). dt is 0.0001; ; otherwise as Figure C.1.

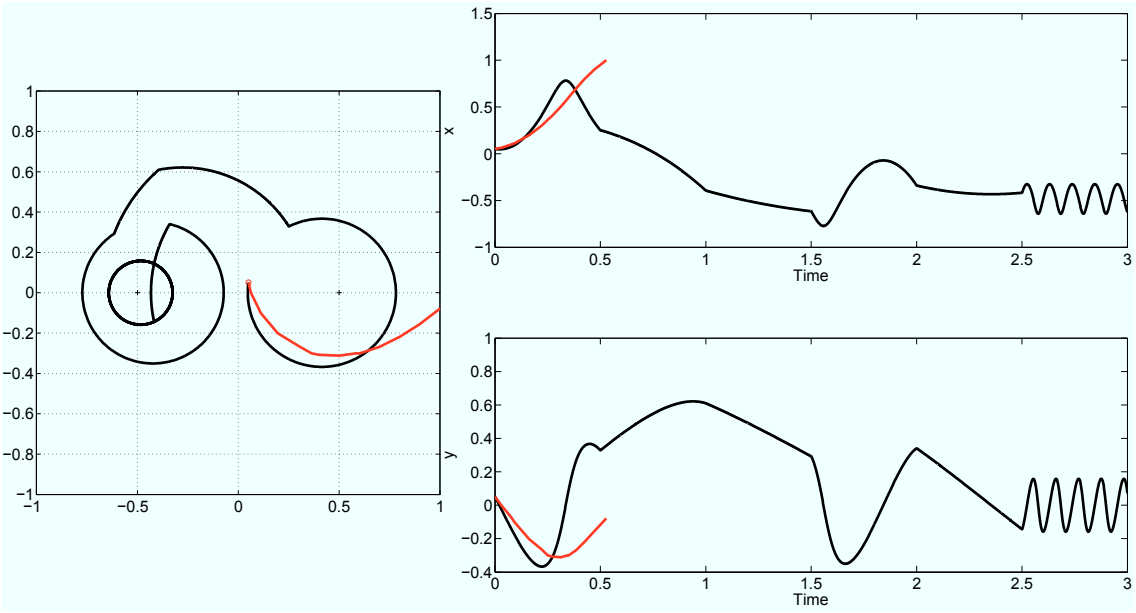

Figure C.5: Particle trajectory calculated using DS method (red line) against Aref's analytically calculated trajectory (black). Left panel shows the calculated trajectories. Right hand panels show the change in x position and the change in y position with time. dx is 0.1.

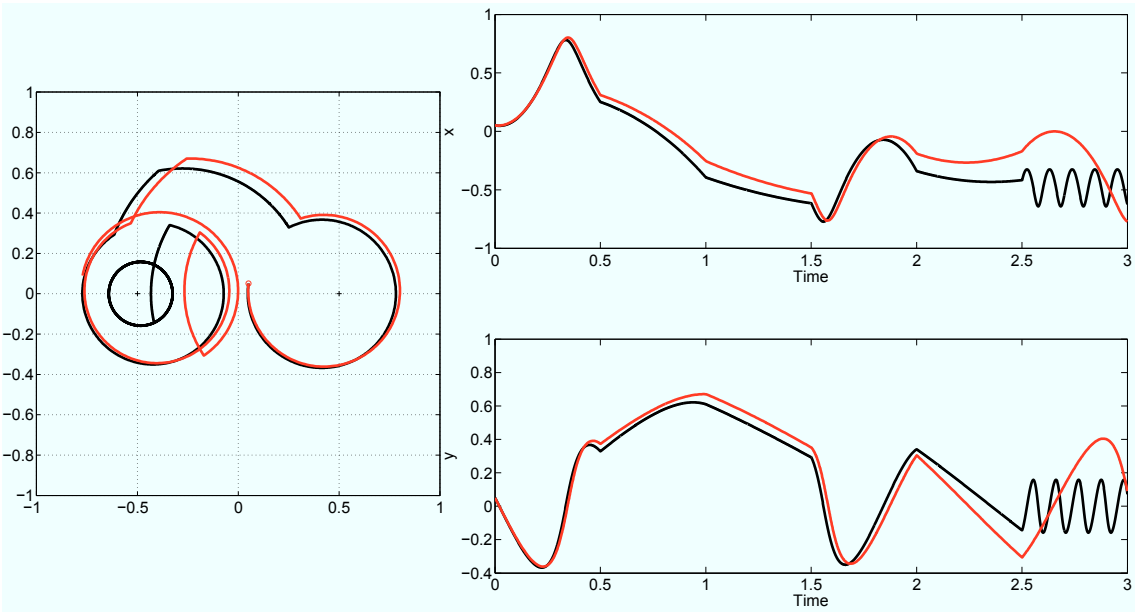

Figure C.6: Particle trajectory calculated using DS method (red line) against Aref's analytically calculated trajectory (black). dx is 0.01; otherwise as Figure C.5.

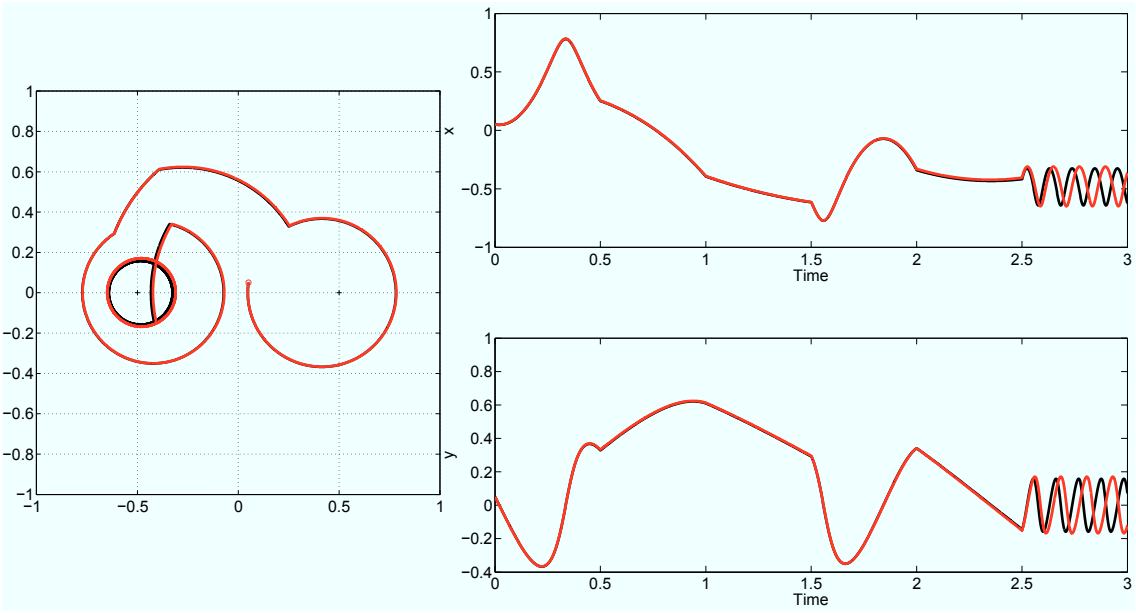

Figure C.7: Particle trajectory calculated using DS method (red line) against Aref's analytically calculated trajectory (black). dx is 0.001; otherwise as Figure C.5.

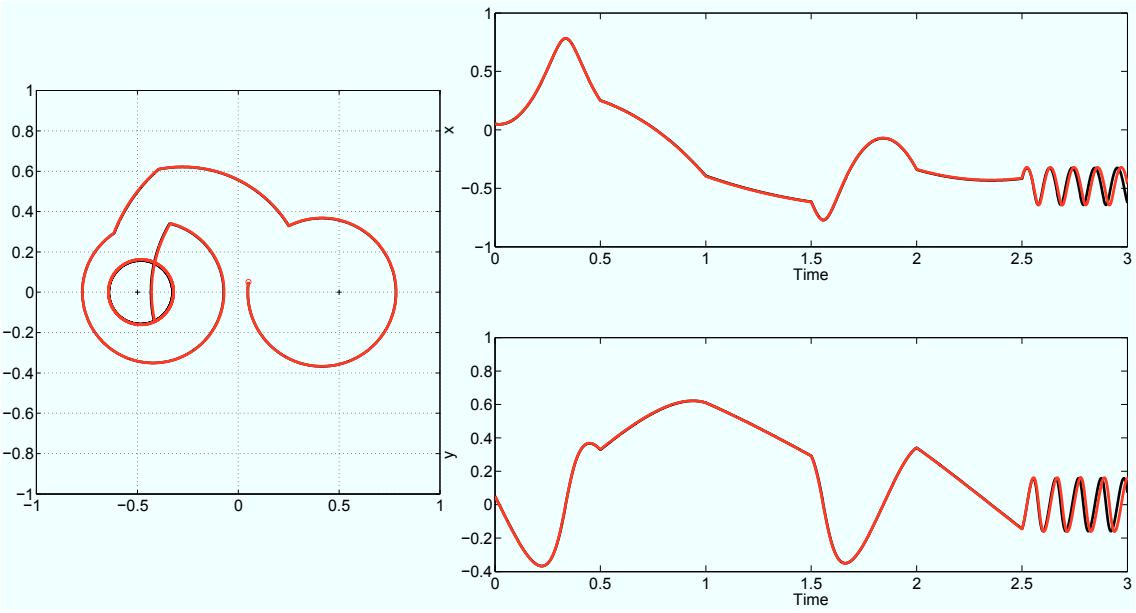

Figure C.8: Particle trajectory calculated using DS method (red line) against Aref's analytically calculated trajectory (black). dx is 0.0005; otherwise as Figure C.5.

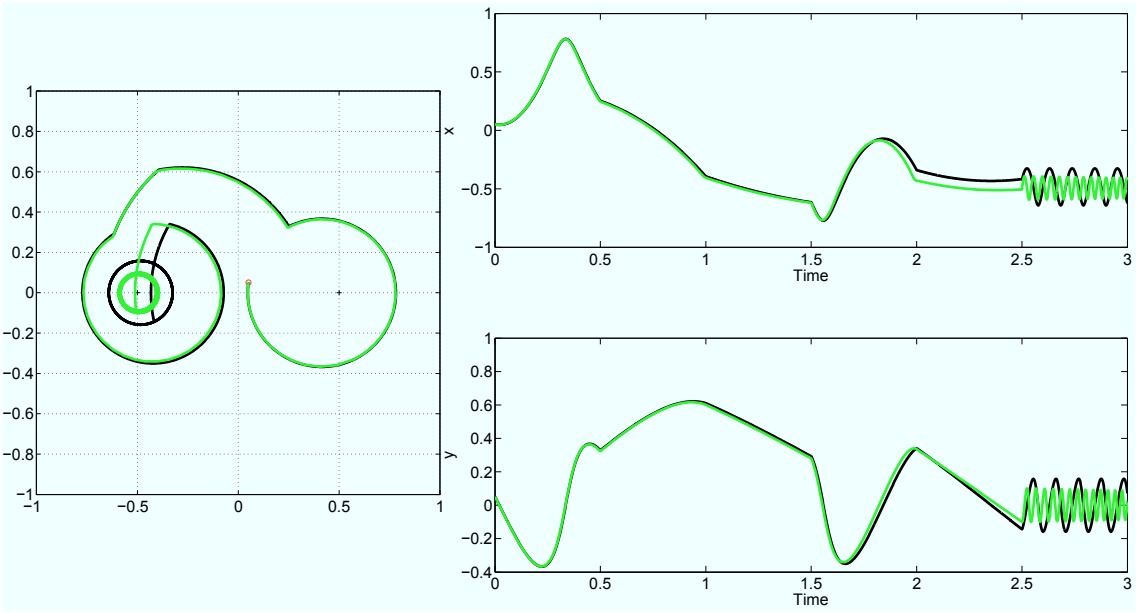

Figure C.9: Particle trajectory calculated using Matlab's onboard Runge-Kutta method: "ODE45" (green line) against Aref's analytically calculated trajectory (black). Left panel shows the trajectory around the center. Right hand panels show the change in x position and the change in y position with time.

C.2 Visser's False Aggregation

Final particle positions are calculated using the DT and DS methods (red line) in Visser's spatially varying diffusivity fields after various lengths of time. The DT method has false aggregation in the area of low diffusivity while the DS method does not. Low diffusivity was created in a bullseye pattern such that the low diffusivity was at the center (50,50) and increased out to the outside, reflective edges of the box.

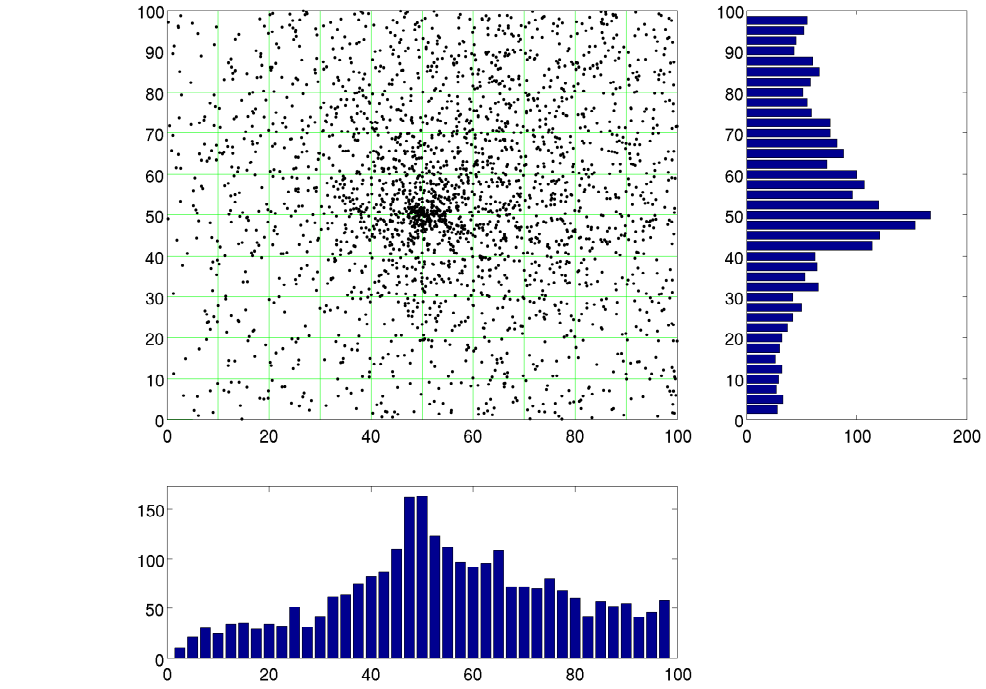

(a)

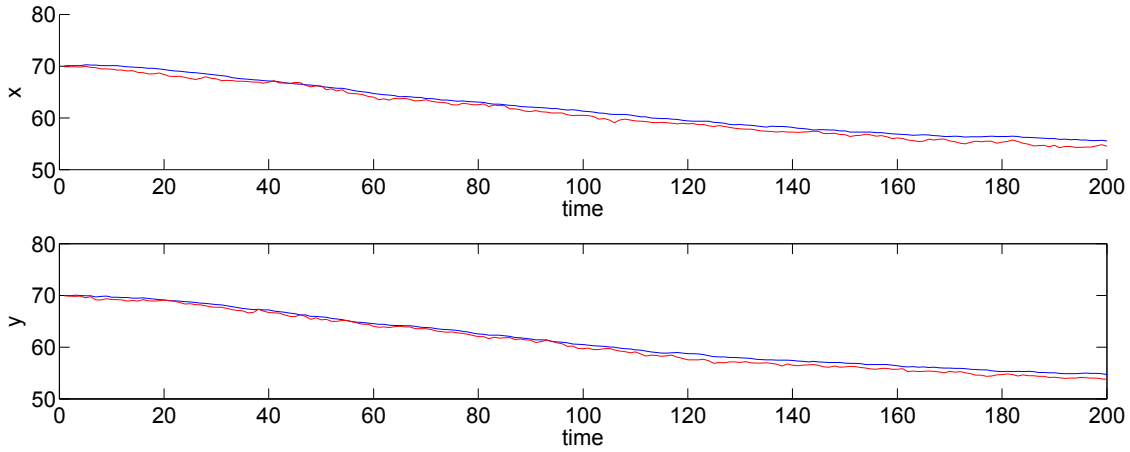

(b)

Figure C.10: Discrete Time: Particle positions after 200 in a field of differing spatial diffusivity. (a) demonstrates how the DT model has false aggregation in the area of low diffusivity. Low diffusivity was created in a bullseye pattern such that the low diffusivity was at the center (50,50) and increased out to the outside, reflective edges of the box. Bottom and right panels of (a) show numbers of particles by x and y position respectively. Lower panels show the changing mean (blue) and median (red) with time.

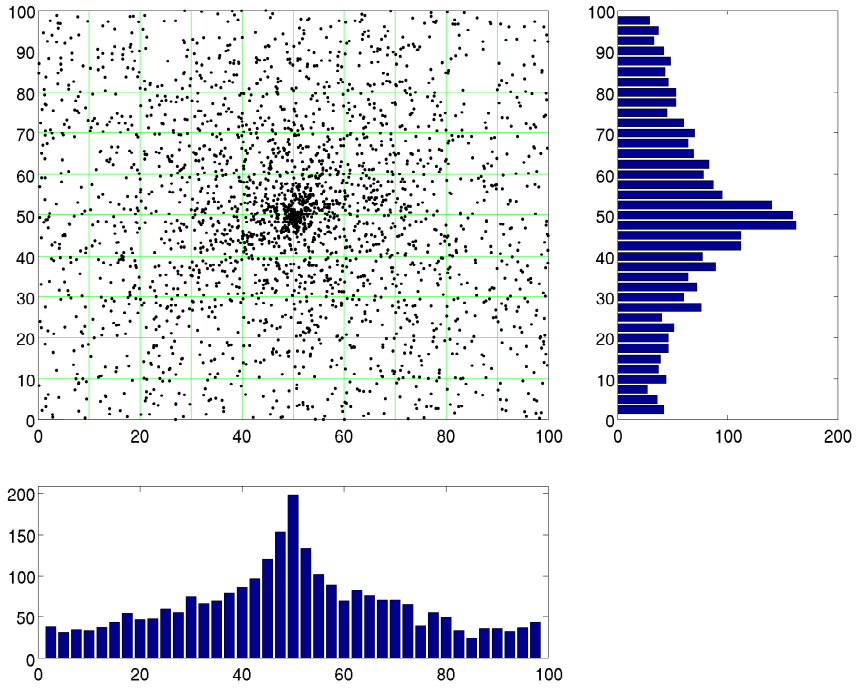

(a)

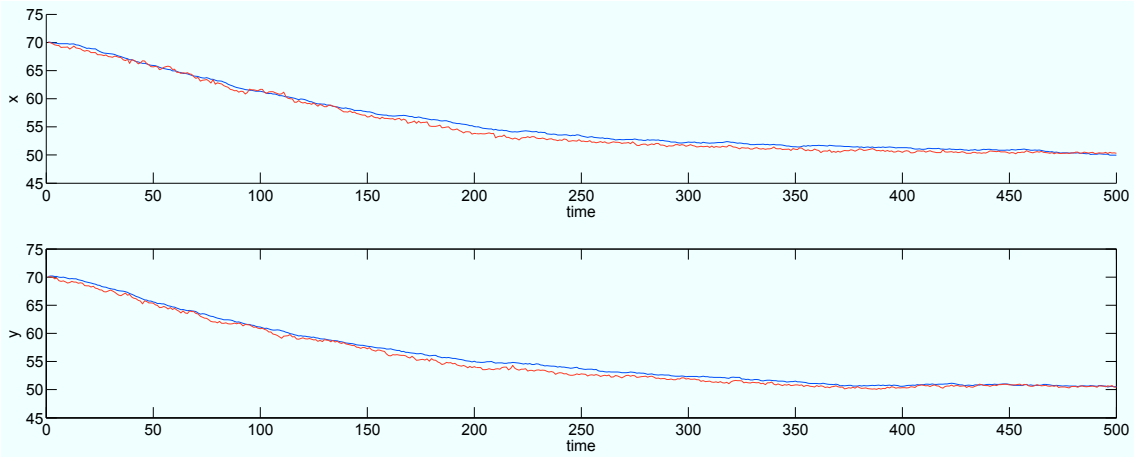

(b)

Figure C.11: Discrete time: Visser's False Aggregation. Top panel shows particle positions after 500 in a field of differing spatial diffusivity. Otherwise as in Figure C.10.

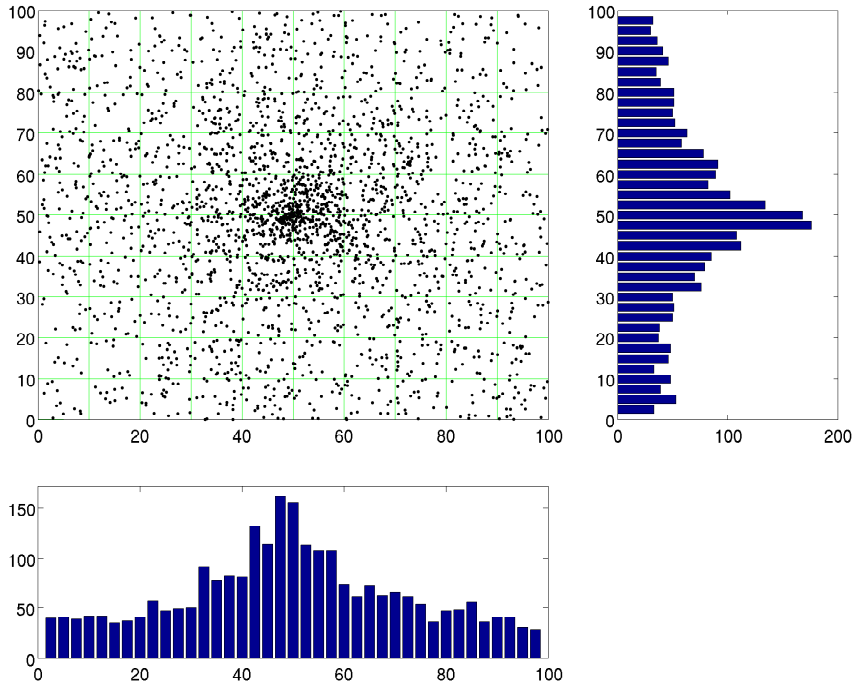

(a)

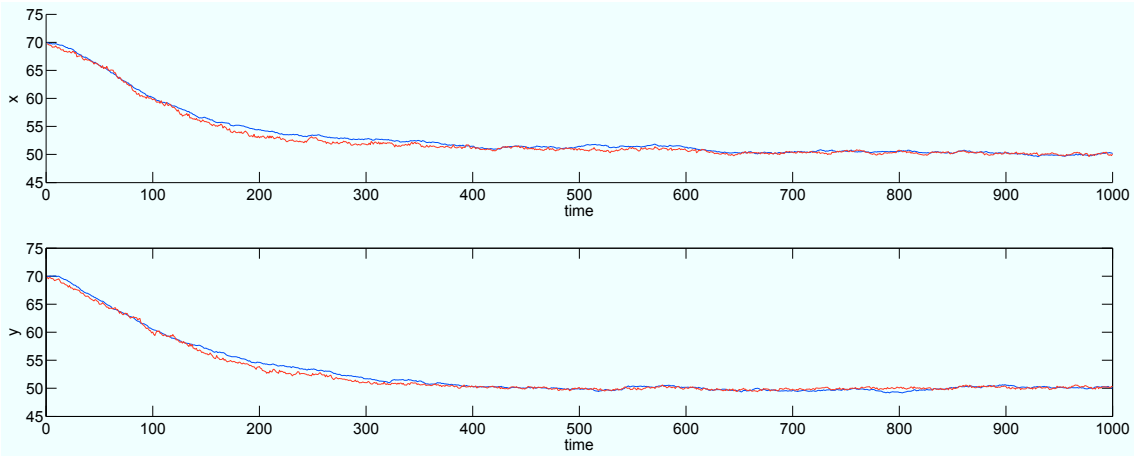

(b)

Figure C.12: Particle positions after 1000 in a field of differing spatial diffusivity. Otherwise as in Figure C.10.

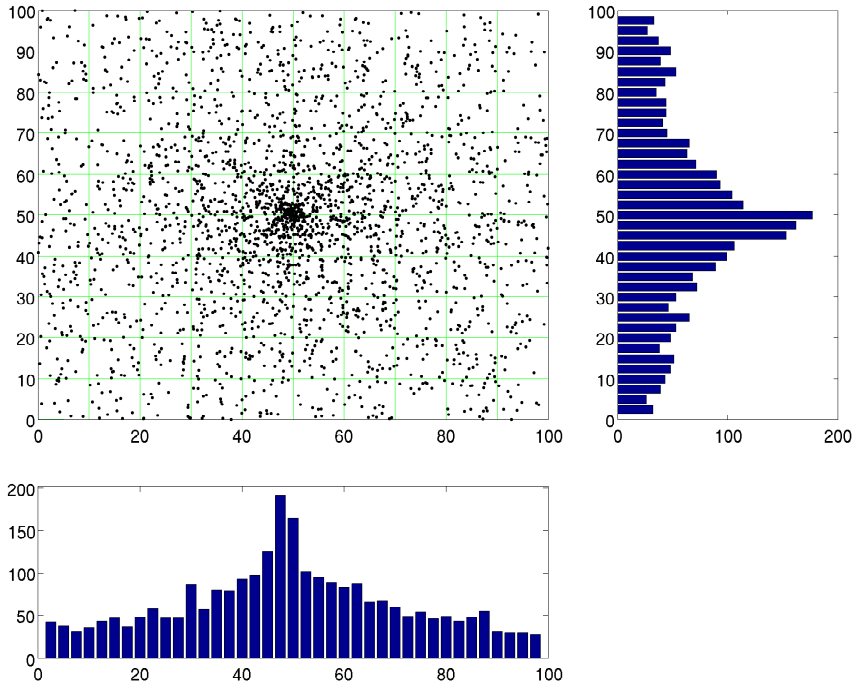

(a)

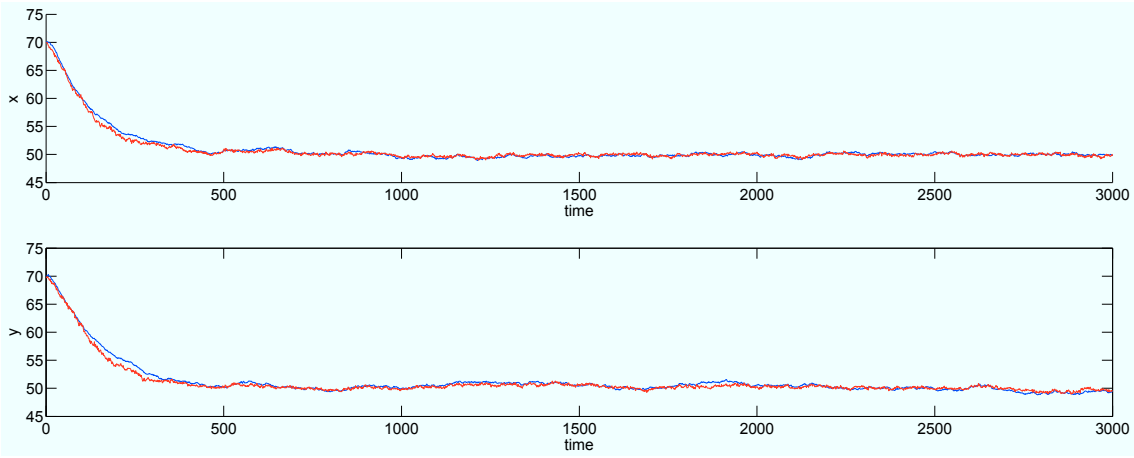

(b)

Figure C.13: Particle positions after 3000 in a field of differing spatial diffusivity. Otherwise as in Figure C.10.

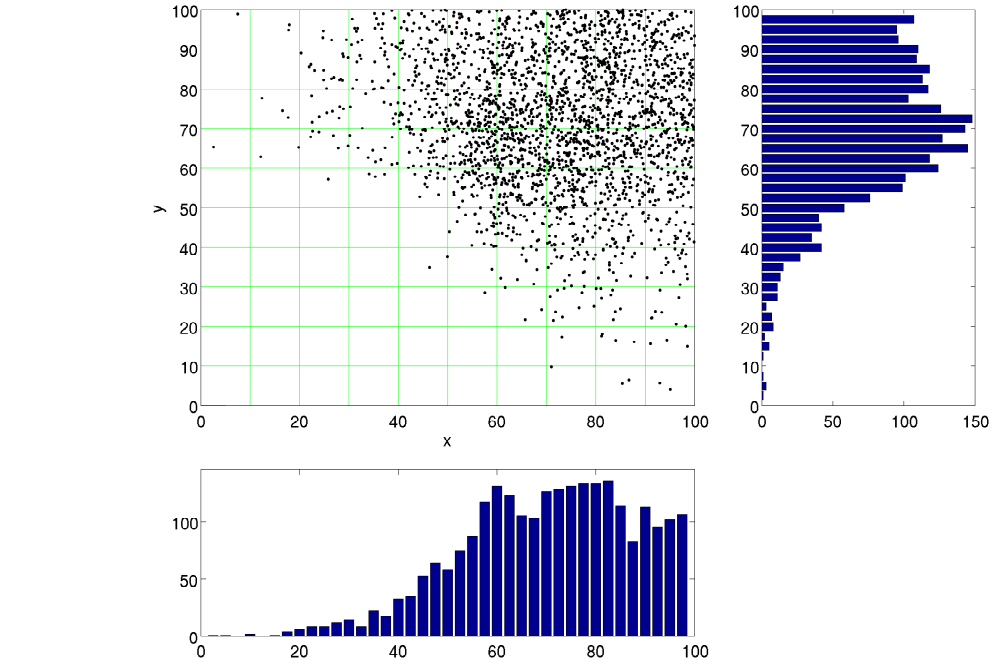

(a)

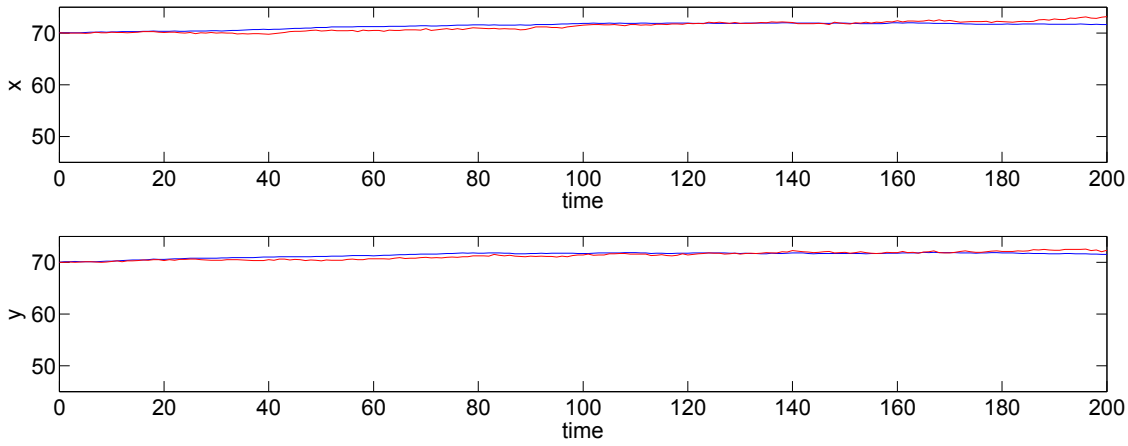

(b)

Figure C.14: Particle positions after 200 in a field of differing spatial diffusivity demonstrates how the DS model shifts towards homogenization rather that false aggregation in the area of low diffusivity. Otherwise as in Figure C.10.

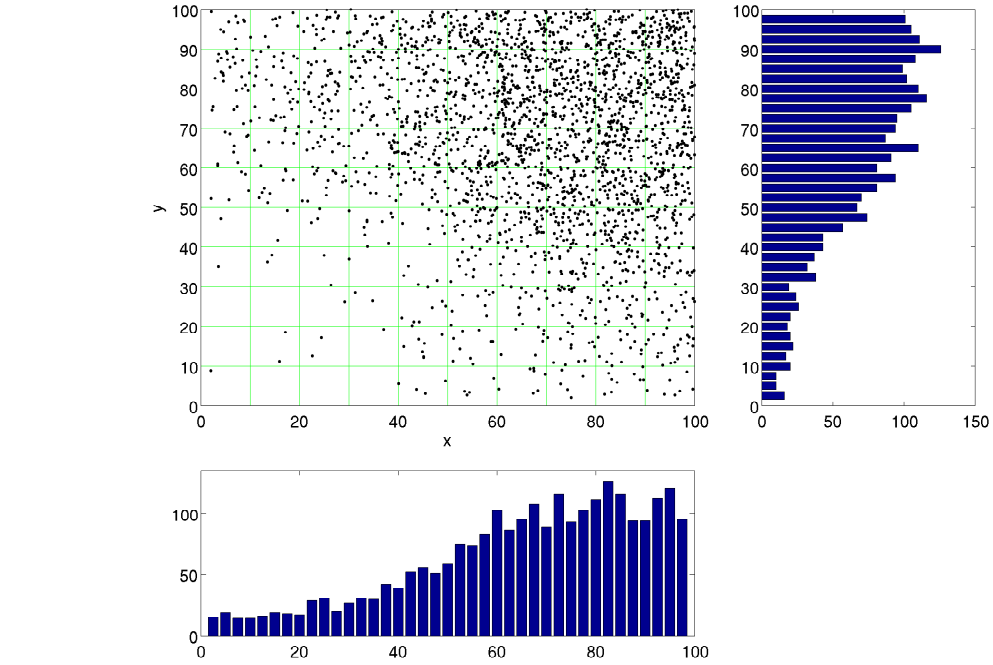

(a)

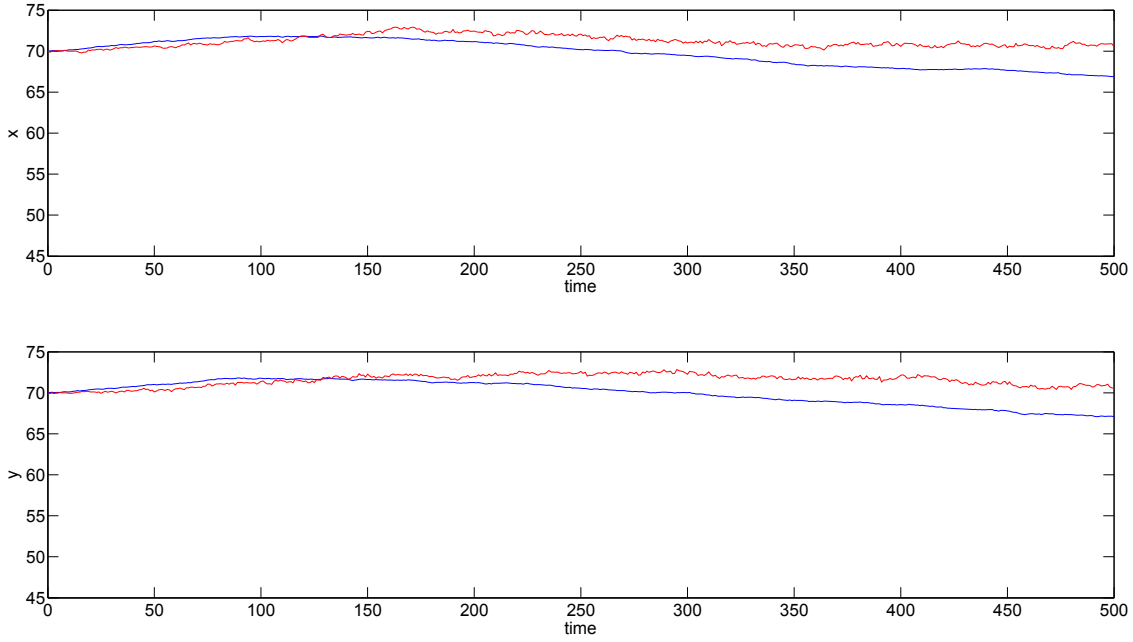

(b)

Figure C.15: Particle positions after 500 in a field of differing spatial diffusivity for the DS method. Otherwise as in Figure C.10.

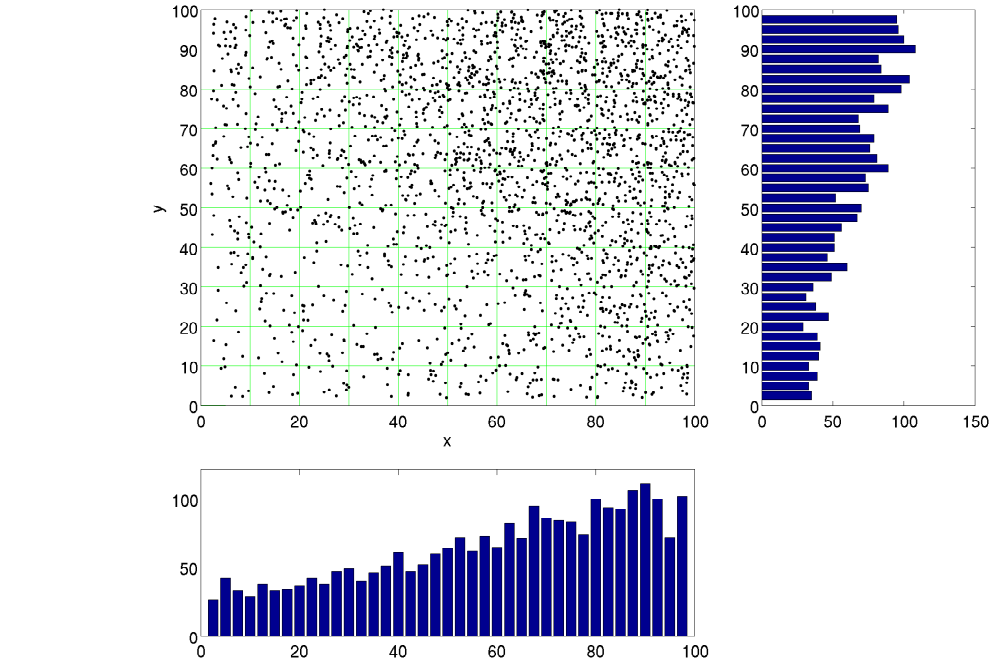

(a)

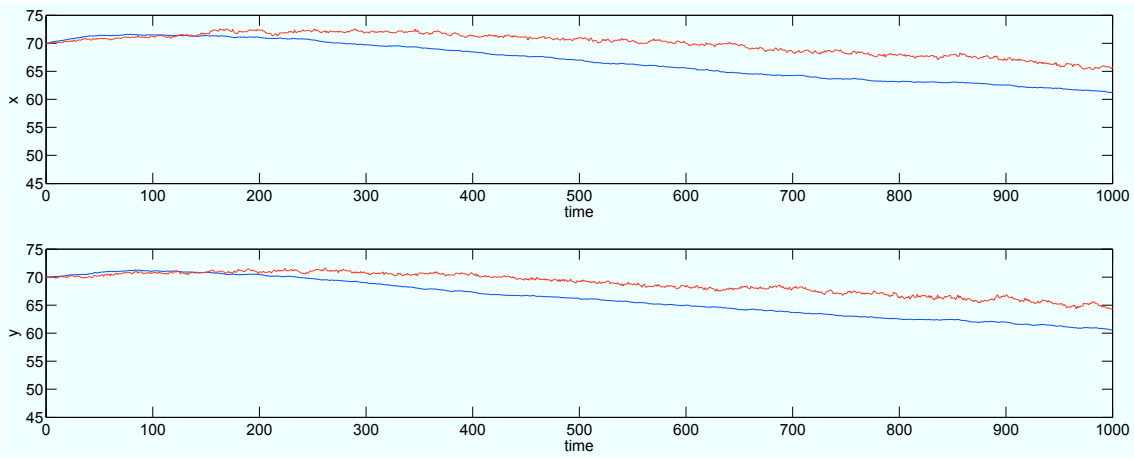

(b)

Figure C.16: Particle positions after 1000 in a field of differing spatial diffusivity for the DS method. Otherwise as in Figure C.10.

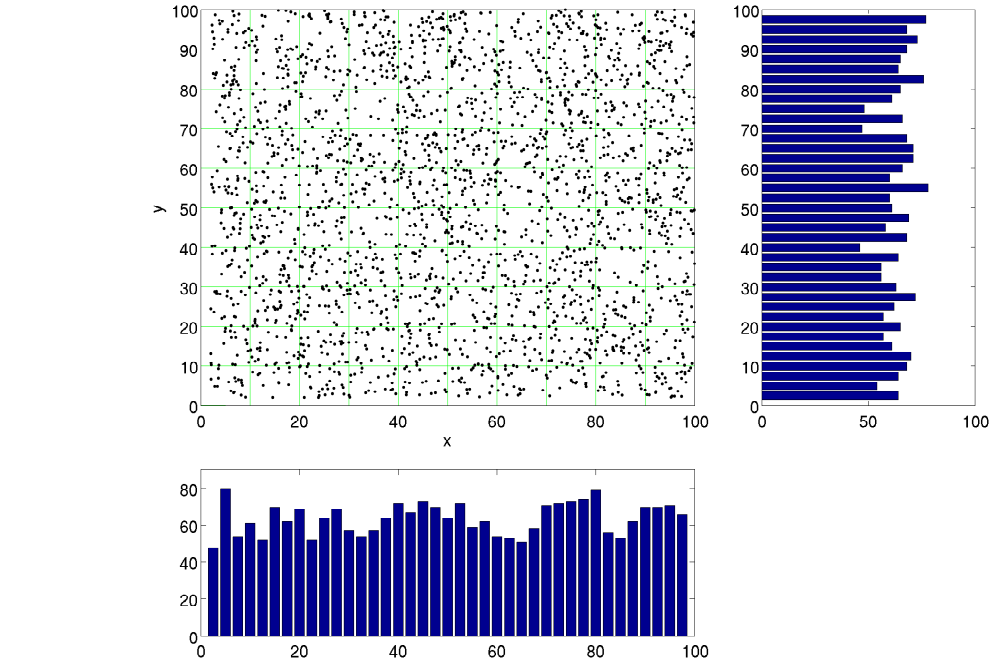

(a)

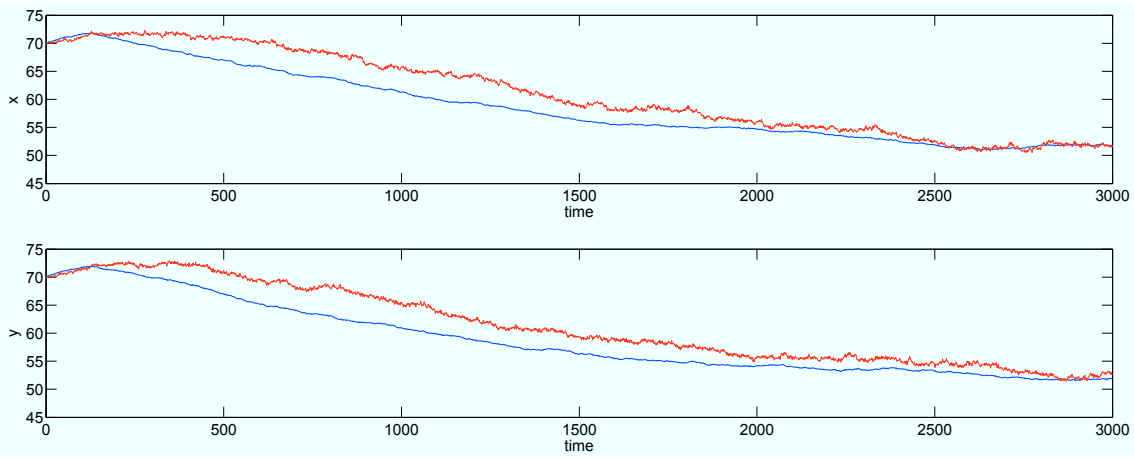

(b)

Figure C.17: Particle positions after 3000 in a field of differing spatial diffusivity for the DS method. Otherwise as in Figure C.10.

APPENDIX D

SOURCE REGIONS AND PARTICLE DESTINATIONS

Included here are supplemental Figures for Chapter 6. Figures D.1 and D.2 show the final position of particles released within Emerald and Lahave Basin respectively for the combined years 2010-2012. Particles were released below 100 meters within each basin and trajectories were calculated using Ariane and daily changing flow fields. In both figures, particles were released on the first day of the season and allowed to travel for 90 days. It is important to note that the flow fields are daily snapshots occurring at 00:30 each day and not daily means.

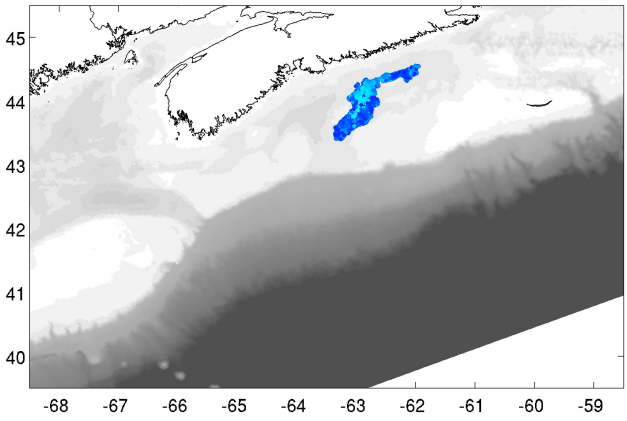

(a) Emerald Basin

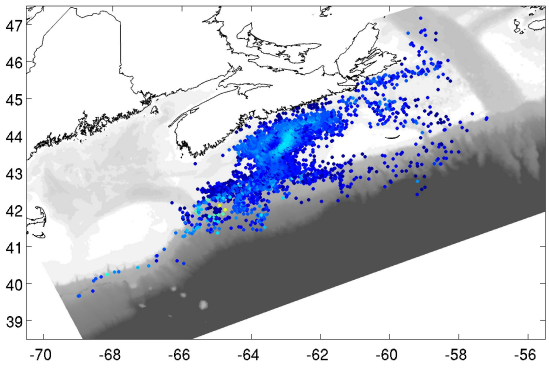

(b) Sources - Winter

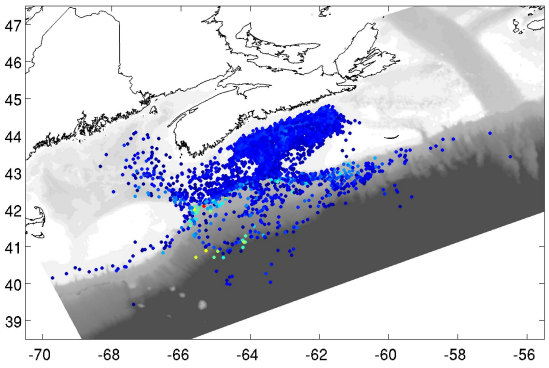

(c) Destinations - Winter

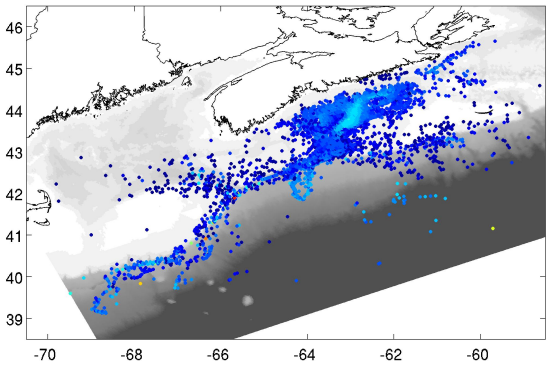

(d) Sources - Summer

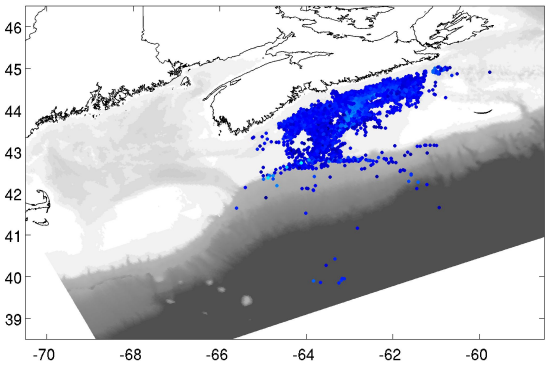

(e) Destinations - Summer

Figure D.1: Sources and destinations of particles in Emerald Basin for both winter and summer for combined years 2010-2012. Particles were released over the full domain of the regional model on January 1st and July 1st of each year and allowed to travel for 90 days in daily changing flow fields. Left hand panels show the particle location (on day 1) for particles that were in the basin below 100 meters on day 90. Right hand panels show the final locations (on day 90) of particles that were released below 100 m in Emerald Basin. Colour indicates the depths at which the particles were released. Dark blue means surface particles; light blue means near bottom release.

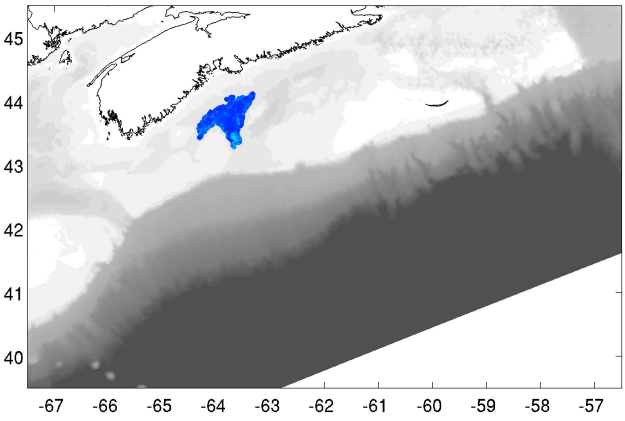

(a) Lahave Basin

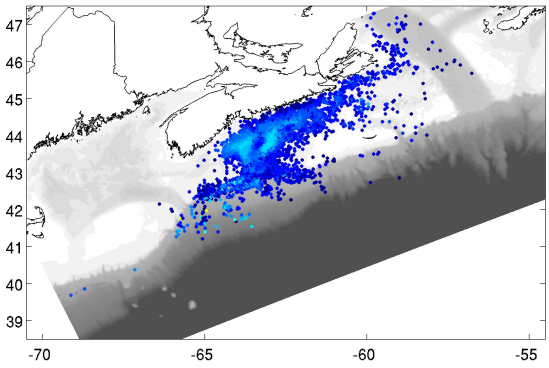

(b) Sources - Winter

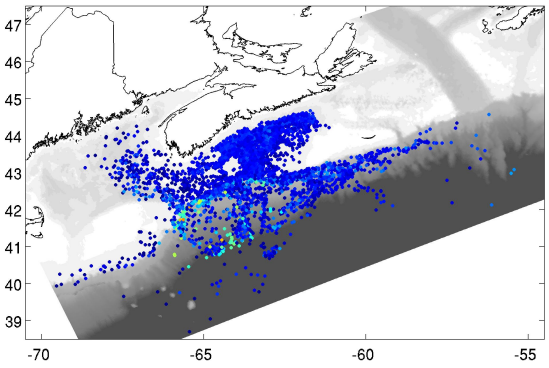

(c) Destinations - Winter

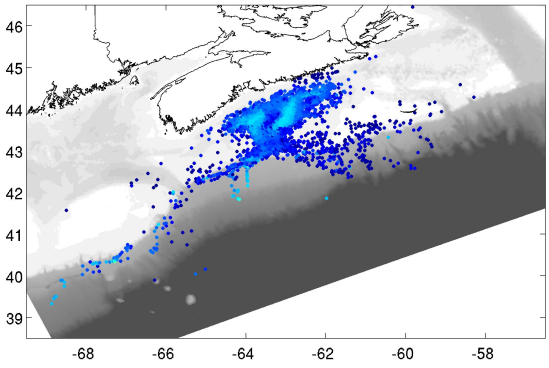

(d) Sources - Summer

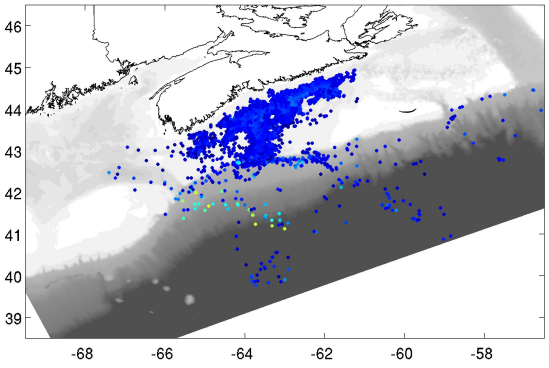

(e) Destinations - Summer

Figure D.2: Sources and destinations of particles in Lahave Basin for both winter and summer for the combined years 2010-2012. Otherwise as in Figure D.1.

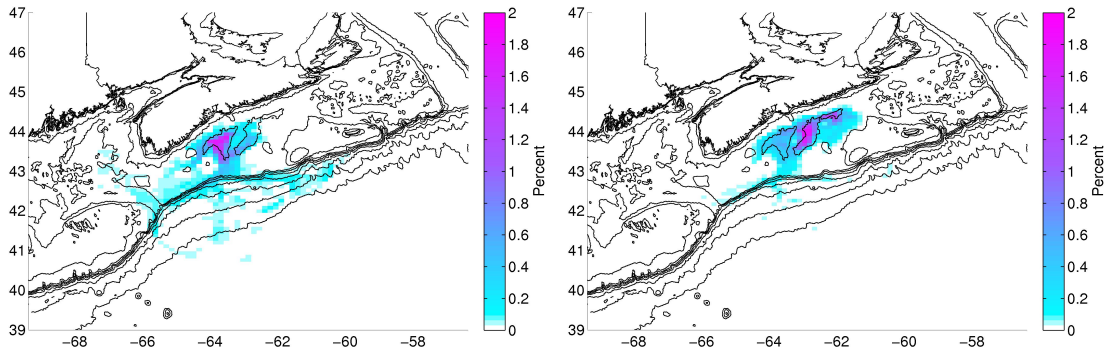

(a) Lahave Basin - Winter

(b) Emerald Basin - Winter

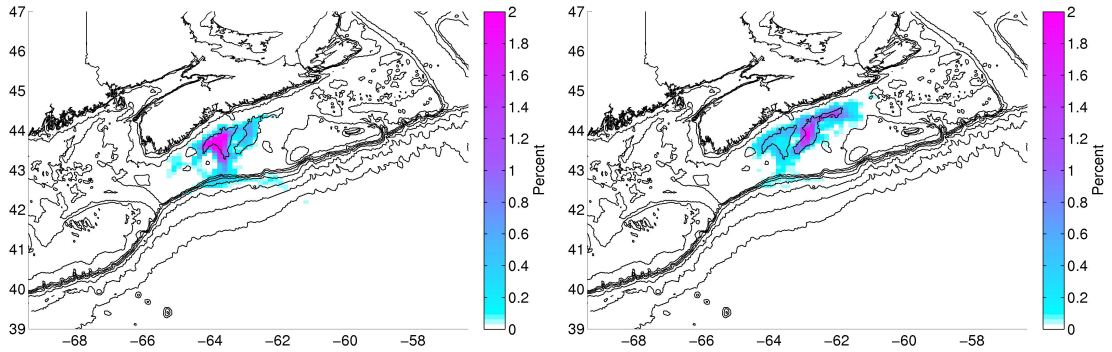

(c) Lahave Basin - Summer

(d) Emerald Basin - Summer

Figure D.3: Destinations of particles which originate in Lahave (left panels) and Emerald Basin (right panels) respectively in both Winter and Summer for the years 2010-2012. All panels show the final locations (on day 90) of particles that started below 100 m within the respective basin (on day 1). The advecting flow fields were daily snapshots as discussed in Chapter 5. The dispersion was set to zero. Particles were released at all depth levels over the entire domain and selectively screened. Particles within the basin polygon above 100 meters were discounted from these results. In each plot particles were released within the basin on each day of January and July respectively, and allowed to drift for the remainder of the 90 period.

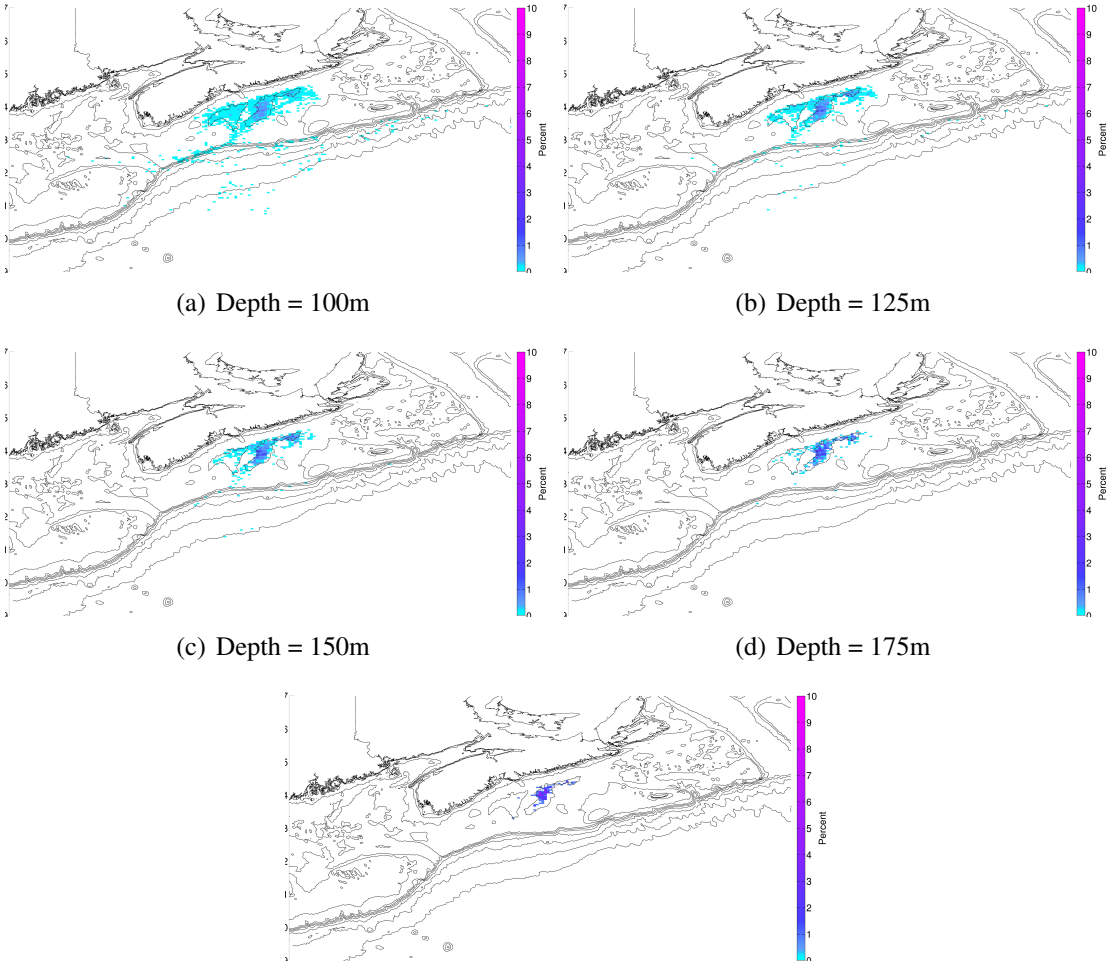

(a) Depth = 100m

(b) Depth = 125m

(c) Depth = 150m

(d) Depth = 175m

(e) Depth = 200m

Figure D.4: Retention of particles in Emerald Basin for January 2010-2012 by minimum release depth. Particles were released over the full domain on January 1st and allowed to drift for 90 days. Colour indicates the locations of particles remaining in the basin as a percentage of those initiated in the basin (on day 1), below (a) 100 m (b) 125 m (c) 150 m (d) 170 m (e) 200 m respectively. Blues and turquoise indicate low percentages, purples and magenta indicate high percentages. Note the colourbar ranges from 0 to 10%. Flow fields were daily snapshots as discussed in Chapter 5.

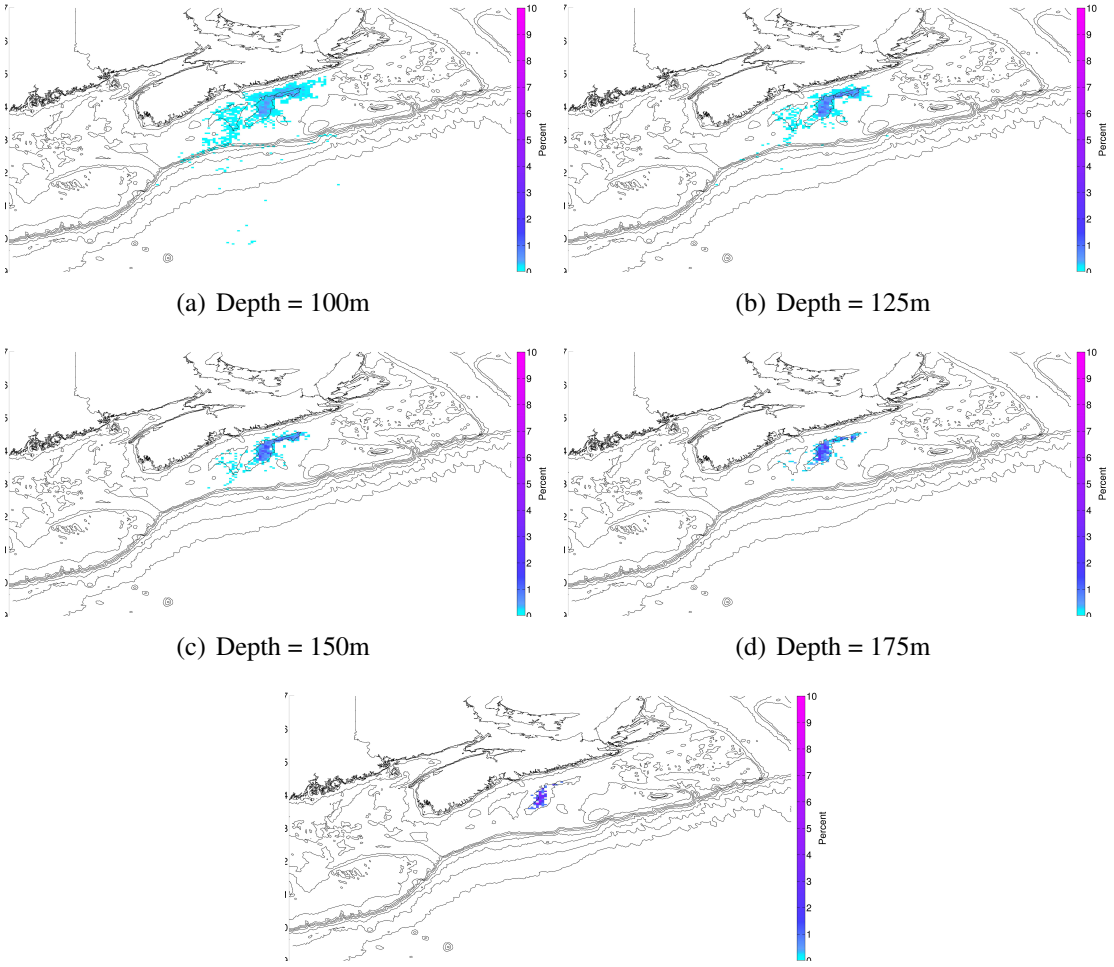

(a) Depth = 100m

(b) Depth = 125m

(c) Depth = 150m

(d) Depth = 175m

(e) Depth = 200m

Figure D.5: Retention of particles in Emerald Basin for July 2010-2012 by depth. Otherwise as in Figure D.4.

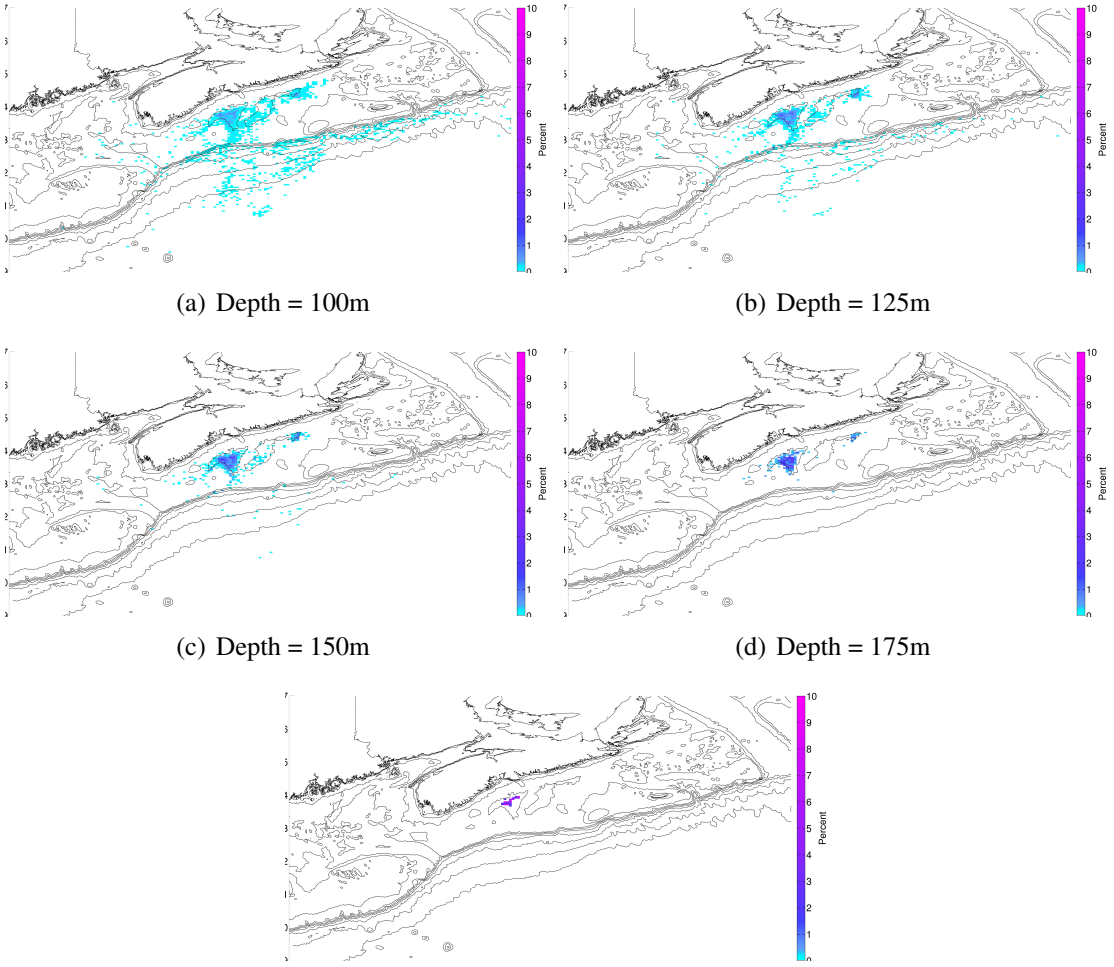

(a) Depth = 100m

(b) Depth = 125m

(c) Depth = 150m

(d) Depth = 175m

(e) Depth = 200m

Figure D.6: Retention of particles in Lahave Basin for January 2010-2012 by depth. Otherwise as in Figure D.4.

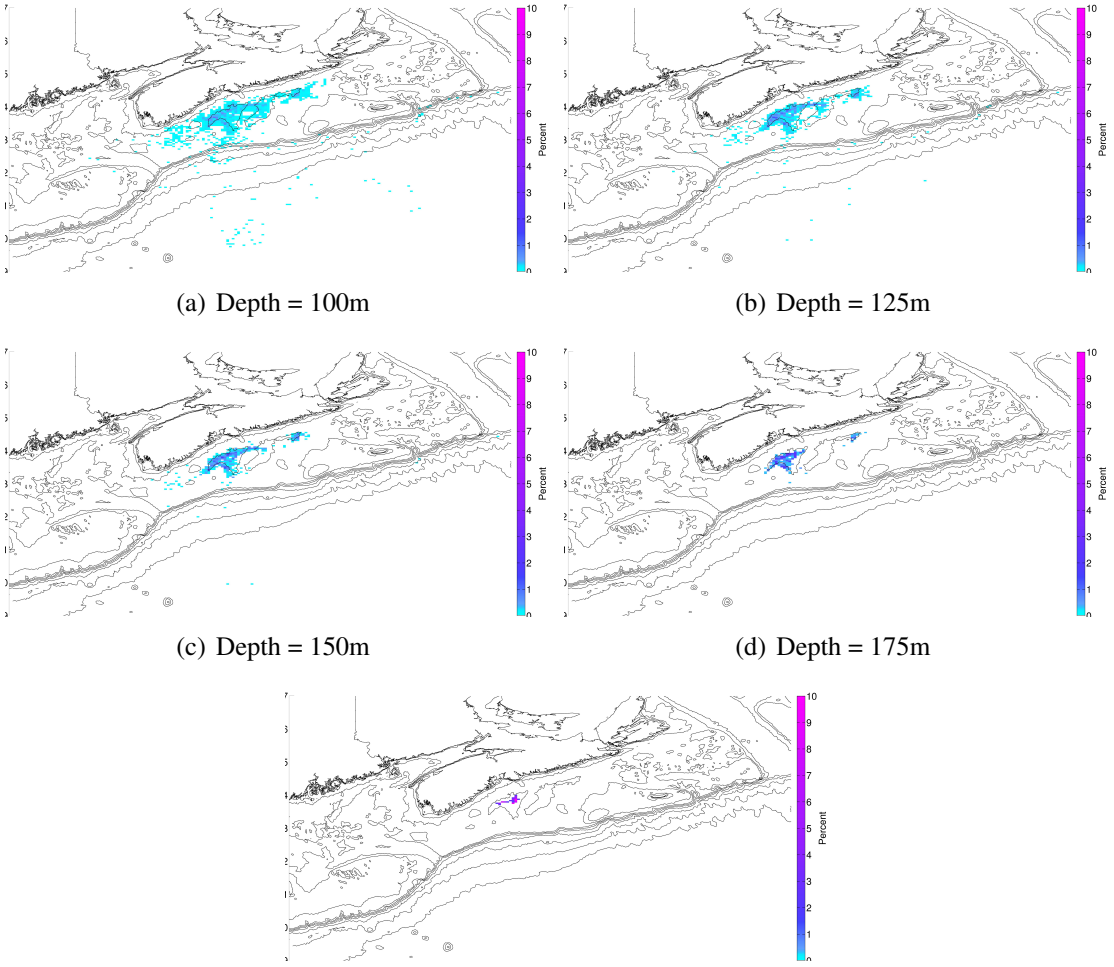

(a) Depth = 100m

(b) Depth = 125m

(c) Depth = 150m

(d) Depth = 175m

(e) Depth = 200m

Figure D.7: Retention of particles in Lahave Basin for July 2010-2012 by depth. Otherwise as in Figure D.4.

APPENDIX E

RETENTION INDICES FOR DIFFERENT BASINS, SEASONS AND DEPTHS

As discussed in Chapter 6, retention indices were calculated for both Emerald and Lahave basin in winter and summer at different minimum release depths.

Emerald Basin - Winter

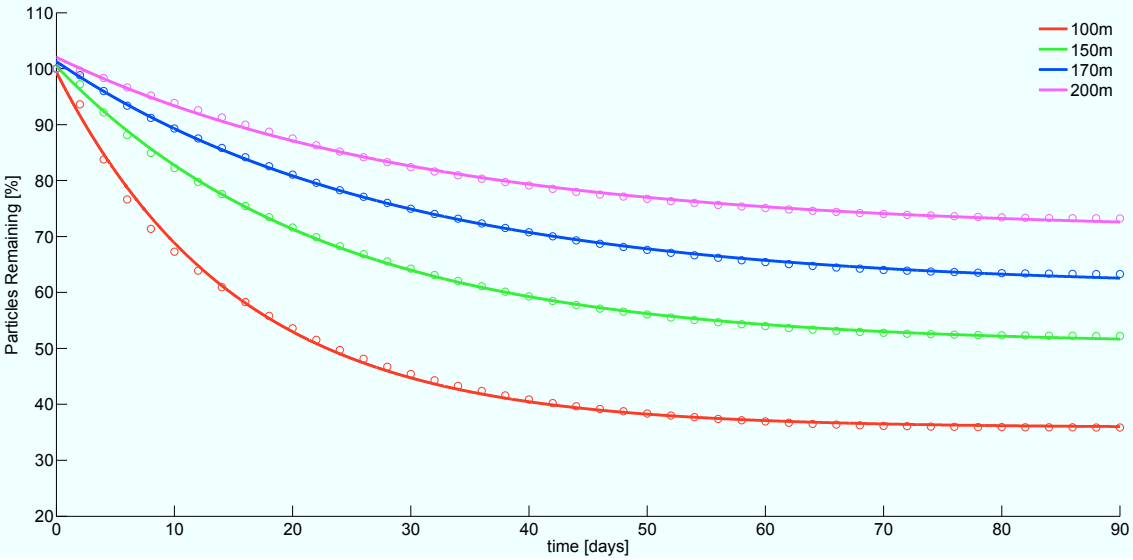

Figure E.1: Retention times for Emerald Basin in winter by minimum release depth.

Depth [m]	Fitted equation	R^2	e-Folding Time
100	$35.85 + 63.57e^{-0.066t}$	0.9971	15.15 days
150	$50.72 + 49.74e^{-0.044t}$	0.9992	22.73 days
170	$60.86 + 40.42e^{-0.035t}$	0.9993	28.57 days
200	$70.96 + 31.08e^{-0.033t}$	0.9976	30.30 days

Table E.1: Retention indices for Emerald Basin by depth in the winter. Particles were released within Emerald Basin below the minimum depth at daily intervals for the month of January. The form of the fitted model is given in equation (6.1). The coefficient of determination, R^2, is also given.

Emerald Basin - Summer

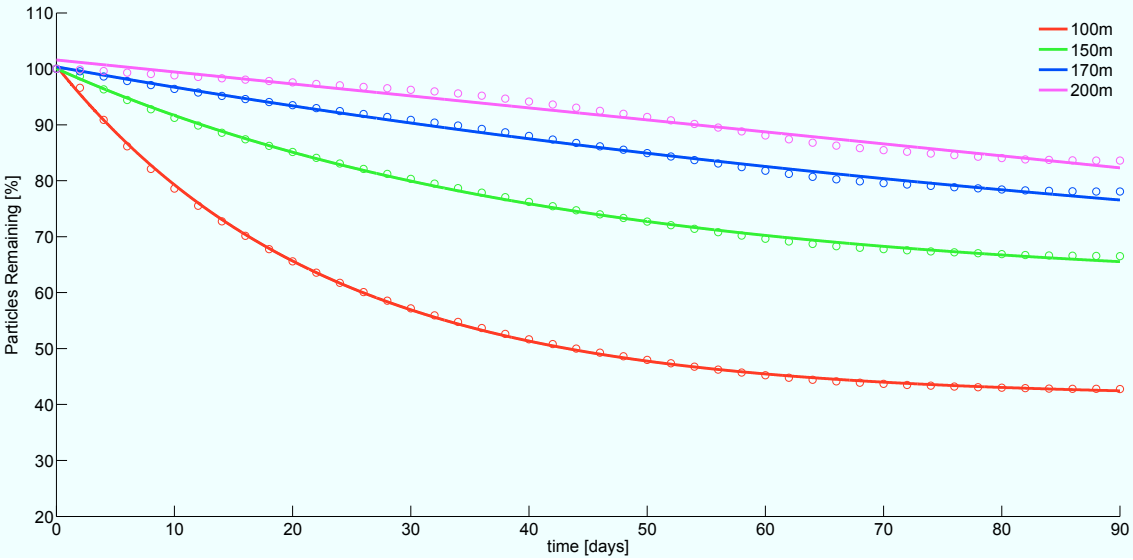

Figure E.2: Retention times for Emerald Basin in summer by minimum release depth.

Depth [m]	Fitted equation	R^2	e-Folding Time
100	$41.37 + 59.14e^{-0.045t}$	0.9994	22.22 days
150	$61.15 + 38.90e^{-0.024t}$	0.9982	41.67 days
170	$56.24 + 44.13e^{-0.009t}$	0.9936	111.11 days
200	$101.59 - 0.21t$	0.9730	

Table E.2: Retention indices for Emerald Basin by depth in the summer. Note the fitted equation for minimum release depth for 200 m is linear. The reason is the decline was so slow that an exponential could not be fit. Otherwise as in Table 6.2

Lahave Basin - Winter

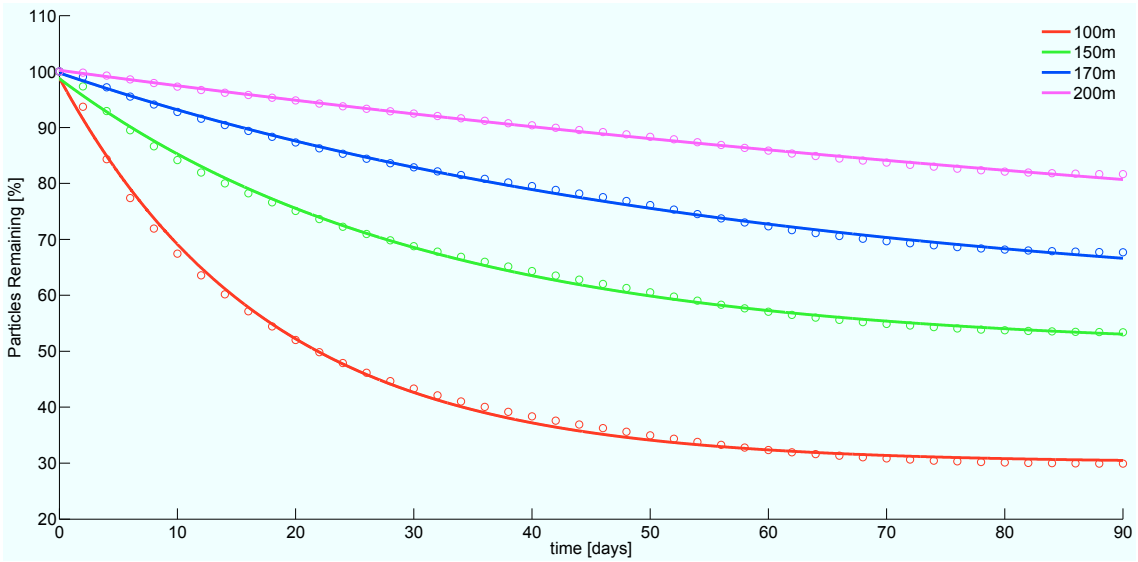

Figure E.3: Retention times for Lahave Basin by depth in winter.

Depth [m]	Fitted equation	R^2	e-Folding Time
100	$30.07 + 68.80e^{-0.057t}$	0.9966	17.54 days
150	$50.54 + 48.20e^{-0.033t}$	0.9972	30.30 days
170	$57.40 + 42.36e^{-0.017t}$	0.9975	58.82 days
200	$55.76 + 44.463^{-0.006t}$	0.9975	166.67 days

Table E.3: Retention indices for Lahave Basin by minimum release depth in winter. Otherwise as in Table 6.2.

Lahave Basin - Summer

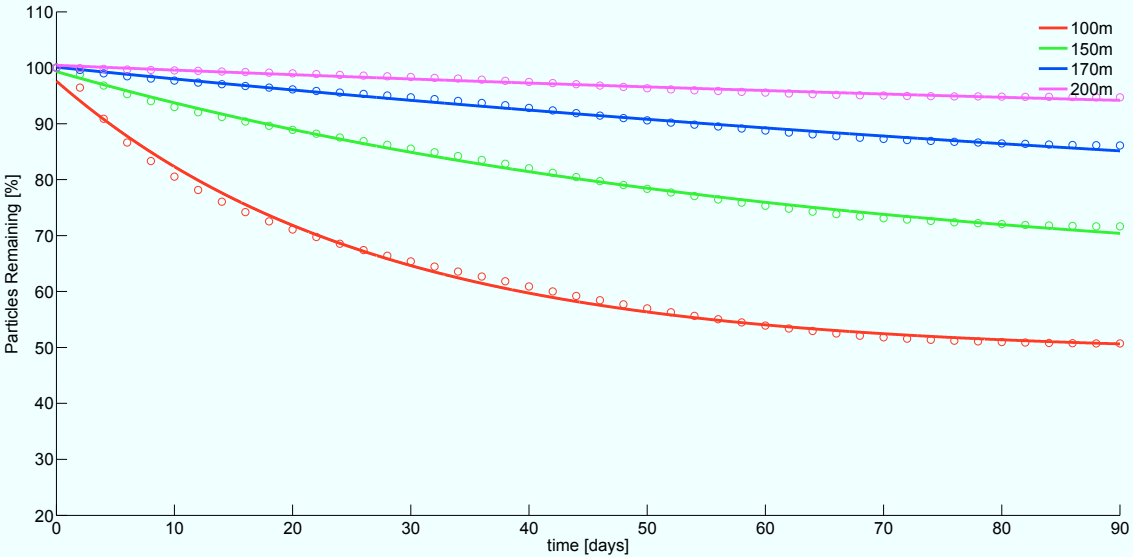

Figure E.4: Retention times for Lahave Basin by depth in summer.

Depth [m]	Fitted equation	R^2	e-Folding Time
100	$49.03 + 48.61e^{-0.038t}$	0.9938	26.32 days
150	$61.36 + 37.96e^{-0.016t}$	0.9952	62.50 days
170	$64.83 + 35.27e^{-0.006t}$	0.9917	166.67 days
200	$84.45 + 15.98^{-0.006t}$	0.9772	166.67 days

Table E.4: Retention indices for Lahave Basin by minimum release depth in summer. Otherwise as in Table 6.2.

APPENDIX F

IDENTIFYING INTERBASIN PATHWAYS

Included here are supplemental Figures for Chapter 6. The following 4 images show particles released over the full domain on the first day of the given season (January or July 1st). The particle trajectories were calculated using Ariane and daily changing snapshot flow fields. Particles were selected based on if they originated (on day 1) in a given basin or terminated (on day 90) in a given basin. Plotting select trajectories allows the connections between basins to become apparent.

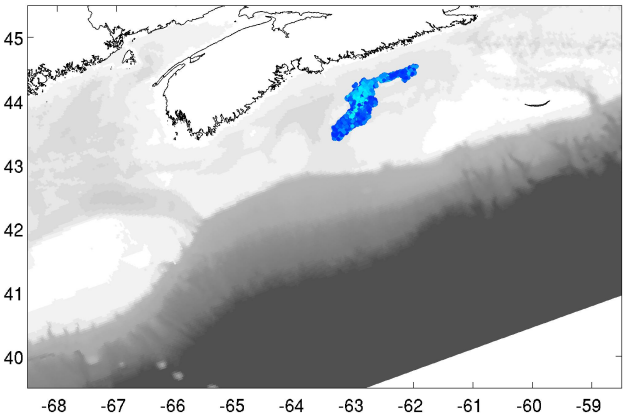

(a) Emerald Basin - Winter

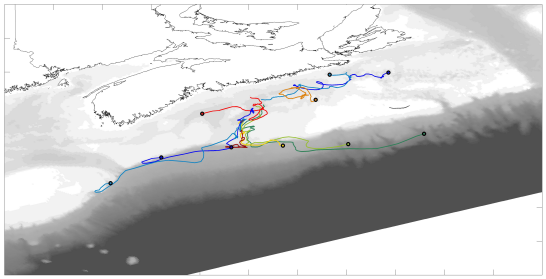

(b) Sources - 2010

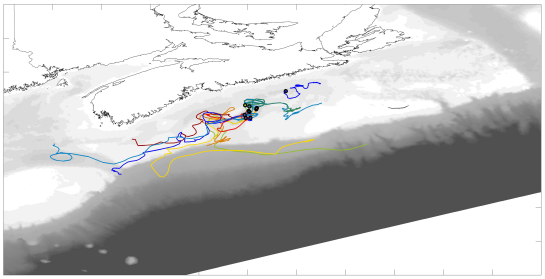

(c) Destinations - 2010

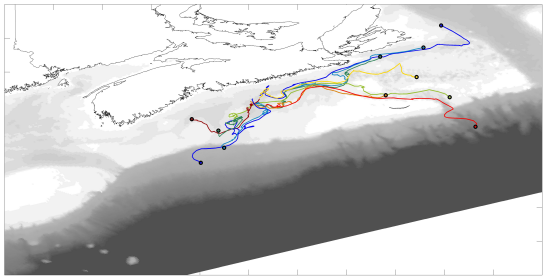

(d) Sources - 2011

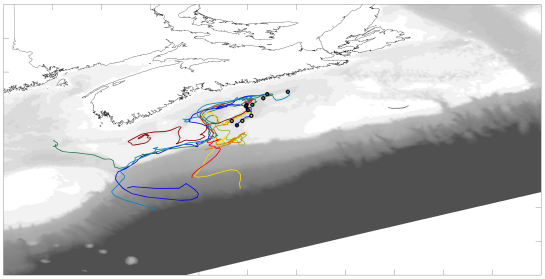

(e) Destinations - 2011

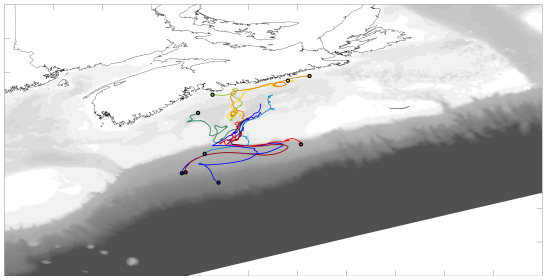

(f) Sources - 2012

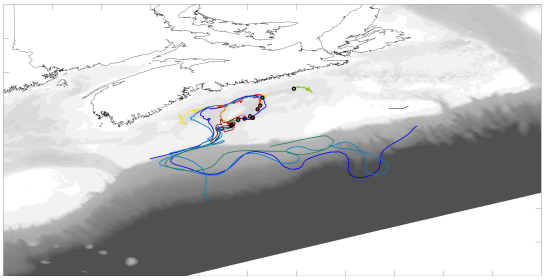

(g) Destinations - 2012

Figure F.1: Trajectories of particles entering and leaving Emerald Basin in winter for the years 2010-2012. Individual particle release position is indicated by the black star. The trajectories were calculated using Ariane and daily flow fields. Particles were released on January 1st, 2010 and allowed to drift for 90 days.

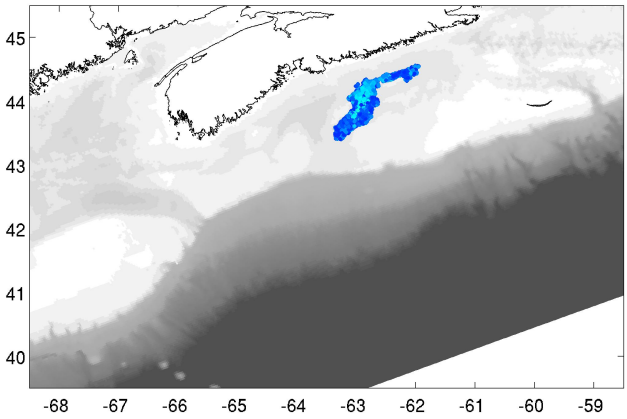

(a) Emerald Basin - Summer

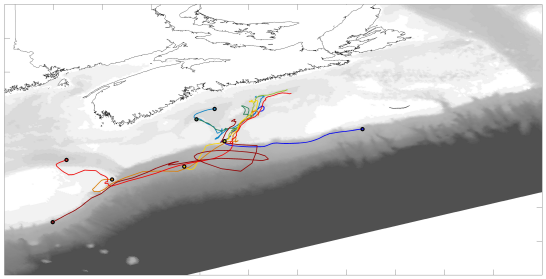

(b) Sources - 2010

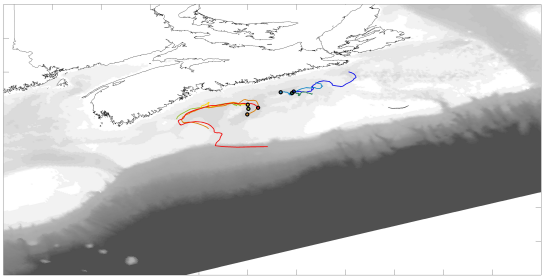

(c) Destinations - 2010

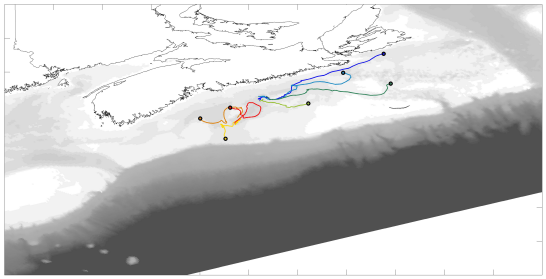

(d) Sources - 2011

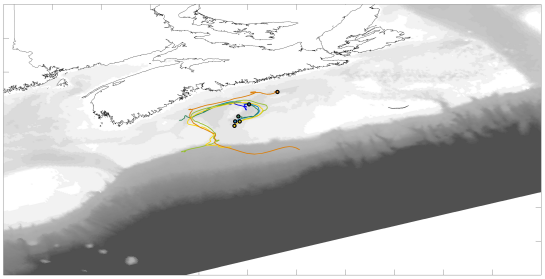

(e) Destinations - 2011

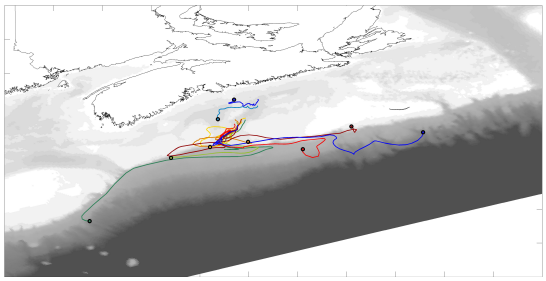

(f) Sources - 2012

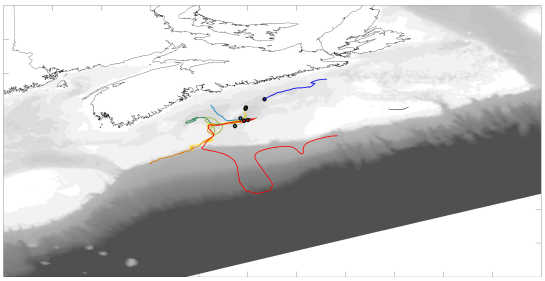

(g) Destinations - 2012

Figure F.2: Trajectories of particles in Emerald Basin in summer for the years 2010-2012. Otherwise as in Figure F.1.

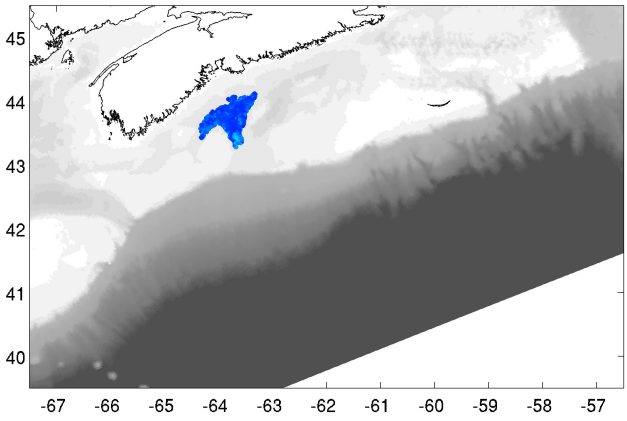

(a) Lahave Basin - Winter

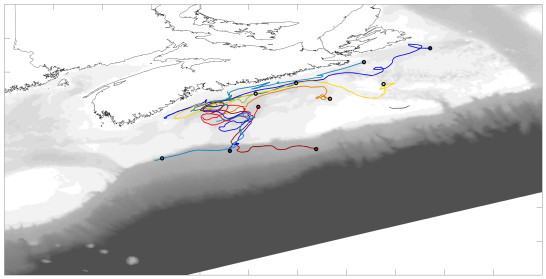

(b) Sources - 2010

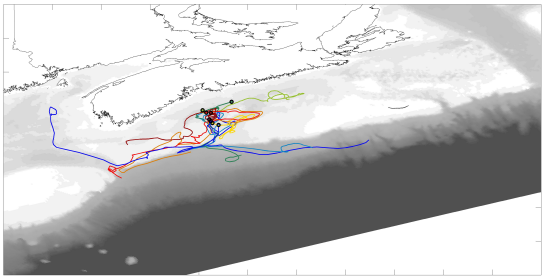

(c) Destinations - 2010

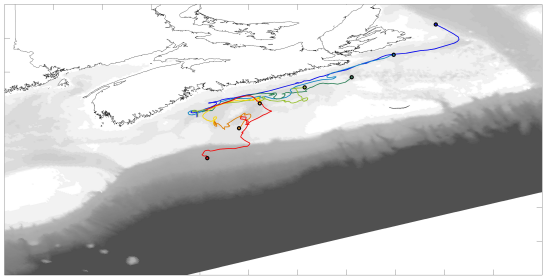

(d) Sources - 2011

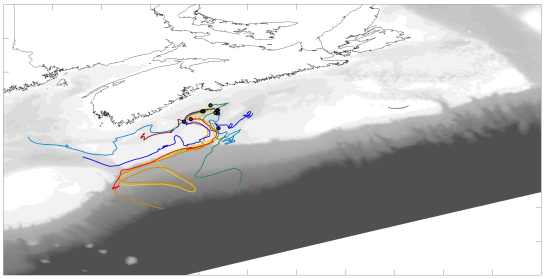

(e) Destinations - 2011

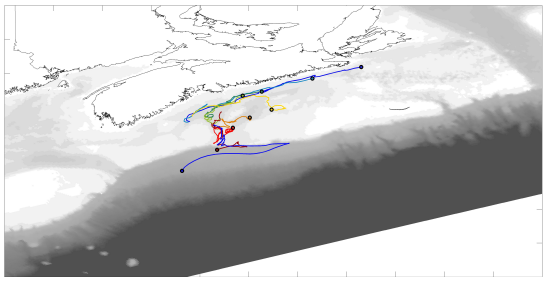

(f) Sources - 2012

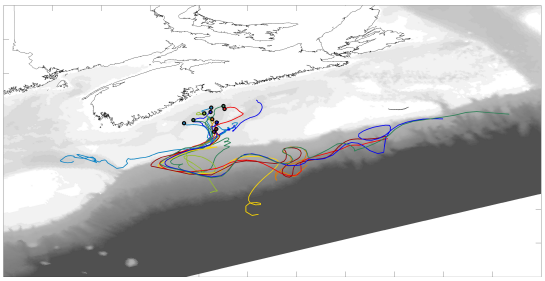

(g) Destinations - 2012

Figure F.3: Trajectories of particles in Lahave Basin in winter for the years 2010-2012. Otherwise as in Figure F.1.

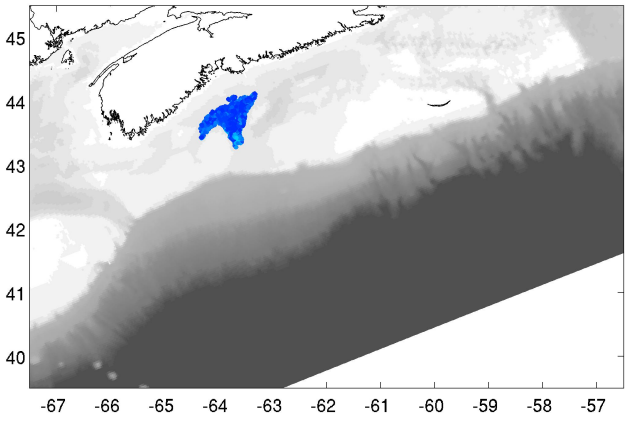

(a) Lahave Basin - Summer

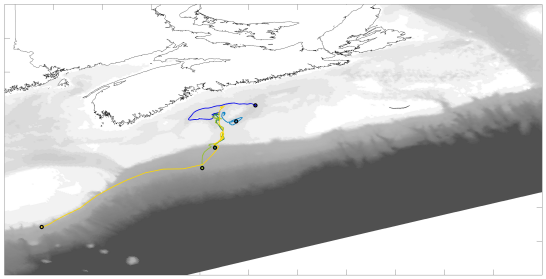

(b) Sources - 2010

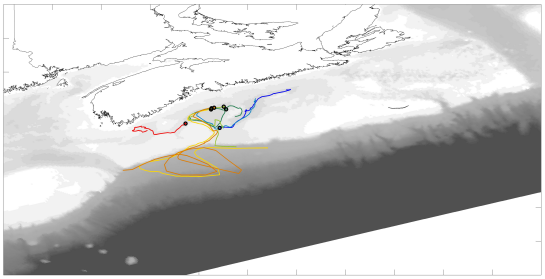

(c) Destinations - 2010

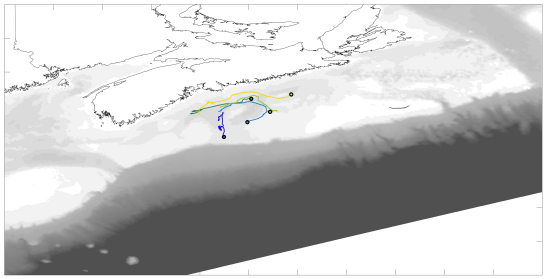

(d) Sources - 2011

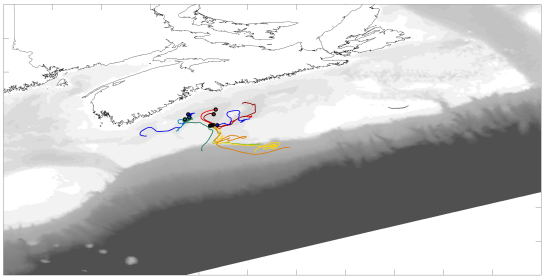

(e) Destinations - 2011

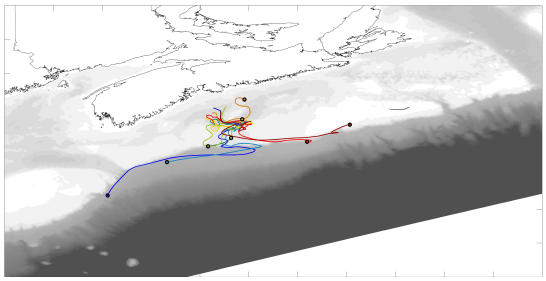

(f) Sources - 2012

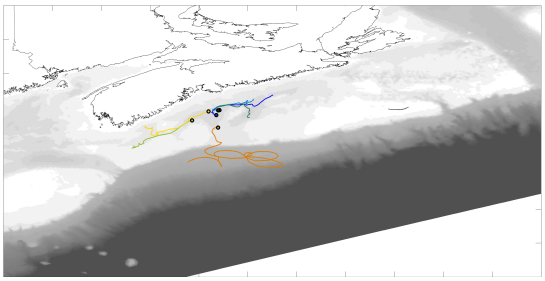

(g) Destinations - 2012

Figure F.4: Trajectories of particles in Lahave Basin in summer for the years 2010-2012. Otherwise as in Figure F.1.

BIBLIOGRAPHY

Allen, A., and J. Plourde, Review of leeway: Field experiments and implementation, *Us coast guard report*, US Coast Guard Research and Development Center, 1999.

Arakawa, A., and V. Lamb, Computational design of the basic dynamical processes of the ucla general circulation model, *Methods of Computational Physics*, *17*, 173–265, 1977.

Aref, H., Stirring by chaotic advection, *Journal of Fluid Mechanics*, *143*, 1–21, 1983.

Batchelor, G., *An Introduction to Fluid Dynamics*, Cambridge University Press, 1967.

Blanke, B., and S. Raynaud, Kinematics of the pacific equatorial undercurrent: An eulerian and lagrangian approach from gcm results, *Journal of Physical Oceanography*, *27*, 1038–1053, 1997.

Breivik, O., and A. Allen, An operational search and rescue model for the norwegian sea and north sea, *Journal of Marine Systems*, *69*, 99–113, 2008.

Breivik, O., T. Bekkvik, C. Wettre, and A. Ommundsen, Baktrak: Backtracking drifting objects using an iterative algorithm with a forward trajectory model, *Ocean Dynamics*, *62*, 239–252, 2012.

Ekman, V., On the influence of the earth's rotation on ocean-currents, *Arkiv for Matematik, Astonomi och fysik*, *2(11)*, 1–51, 1905.

Emerson, S., and J. Hedges, *Chemical Oceanography and the Marine Carbon Cycle*, Cambridge University Press, 2008.

Fisher, H., J. Imberger, N. Brooks, E. List, and R. Koh, *Mixing in Inland and Coastal Waters*, Academic Press Inc, San Diego, 1979.

Fratantoni, P., and R. Pickart, The western north atlantic shelfbreak current system in summer, *Journal of Physical Oceanography*, *37*, 2509–2533, 2007.

Gardiner, C., *Stochastic Methods: A Handbook for the Natural and Social Sciences*, Springer, 2009.

Gill, A., *Atmosphere-Ocean Dynamics*, Academic Press, 1982.

Gillespie, D., The multivariate langevin and fokker-planck equations, *American Journal of Physics*, *64*, 1246–1257, 1996.

Hackett, B., O. Breivik, and C. Wettre, Ocean weather forecasting: An integrated view of oceanography, chap. Forecasting Drift of objects and substances in the oceans, pp. 507–524, Springer, 2006.

Haidvogel, D., and A. Beckmann, *Numerical Ocean Circulation Modeling*, Imperial College Press, 1999.

Hannah, C., J. Shore, J. Loder, and C. Naimie, Seasonal circulation on the western and central scotian shelf, *Journal of Physical Oceanography*, *31*, 591–615, 2001.

Hebert, D., R. Pettipas, D. Brickman, and M. Dever, Meteorological, sea ice and physical oceanographic conditions on the scotian shelf and in the gulf of maine during 2012, *Canadian science advisory secretariat: Research document 2013/058*, 2013.

Hunter, J., P. Craig, and H. Phillips, On the use of random walk models with spatially variable diffusivity, *Journal of Computational Physics*, *106*, 366–376, 1992.

Isobe, A., S. Kako, P. Chang, and T. Matsuno, Two-way particle-tracking model for specifying sources of drifting objects: Application to the east china sea shelf, *Journal of Atmospheric and Oceanic Technology*, *26*, 1672–1682, 2009.

Jordan, R., D. Kinderlehrer, and F. Otto, The variational formulation of the fokker-planck equation, *SIAM Journal on Mathematical Analysis*, *29:1*, 1–17, 1998.

Katavouta, A., K. Thompson, Y. Lu, and J. Loder, Seasonal changes in the tides and mean circulation of the scotian shelf and the gulf of maine, *Journal of Physical Oceanography*, 2015.

Kundu, P., and I. Cohen, *Fluid Mechanics: Fourth Edition*, Elsevier, 2008.

Lemons, D., and A. Gythiel, Paul langevin's 1908 paper "on the theory of brownian motion" ["sur la théorie du mouvement brownien," c.r. acad. sci. (paris) 146, 530-533 (1808)], *American Journal of Physics*, *65(11)*, 1079–1081, 1997.

Lumley, J., Eulerian and langranian descriptions in fluid mechanics, *National Committee for Fluid Mechanics Films*, 1969.

Lynch, D., C. Naimie, J. Ip, C. Lewis, F. Werner, R. Luettich, and . R. Gorman, Real-time data assimilative modeling on georges bank, *Oceanography*, *17(1)*, 65–77, 2001.

Lynch, D., D. Greenberg, D. M. A. Bilgili, J. Manning, and A. Aretxabaleta, *Particles in the Coastal Ocean; Theory and Applications*, Cambridge University Press, 2015.

MacLean, M., H. Breeze, J. Walmsley, and J. Corkum, State of the scotian shelf report, *Aczisc context document*, 2011.

North, E., R. Hood, S.-Y. Chao, and L. Sanford, Using a random displacement model to simulate turbulent particle motion in a baroclinic frontal zone: A new implementation scheme and model performance tests, *Journal of Marine Systems*, *60*, 365–380, 2006.

Press, W., B. Flannery, S. Teukolsky, and W. Vetterling, *Numerical Recipes: The Art of Scientific Computing (3rd ed.)*, Cambridge University Press, 1999.

Stokes, G., *Mathematical and Physical Papers*, Cambridge at the University Press, 1880.

Thompson, C., State of the gulf of maine report: The gulf of maine in context, *Gulf of maine council on the marine environment and fisheries and oceans canada report*, 2010.

Thompson, K., M. Dowd, Y. Shen, and D. Greenberg, Probabilistic characterization of tidal mixing in a coastal embayment: a markov chain approach, *Continental Shelf Research*, *22*, 1603–1614, 2002.

Uchupi, E., Atlantic continental shelf and slope of the united states - physiography, *Geological survey professional paper 529-c*, 1968.

Visser, A., Using random walk models to simulate the vertical distribution of particles in a turbulent water column, *Marine Ecology Progress Series*, *158*, 275–281, 1997.